UNIVERSITY OF
BIRMINGHAM

Filtering amplifiers based on coupled resonator circuits

by

Tianhao He

A thesis submitted to the University of Birmingham for the degree of Doctor of Philosophy

School of Electronic, Electrical and Systems Engineering
The University of Birmingham
March 2015

Abstract

Terahertz (THz) wireless communication systems over 300 GHz can offer broad bandwidth, but they have limitations, such as high precision fabrication requirements, high fabrication cost and lossy system components. This thesis introduces a THz communication system concept based on low-cost and high precision micromachining techniques, also a new design approach to achieve a low loss system for THz communication components and systems. A polymer (SU-8) micromachined THz rectangular waveguide is demonstrated in this thesis, which shows that micromachined SU-8 waveguide is a good solution for THz systems with a performance equivalent to the best metal waveguides.

In order to minimise the components and systems losses, this thesis proposes a design approach for filtering amplifiers which removes the lossy planar matching and interconnection circuits replacing them with waveguide structures to complete the transistor amplifiers design. The technique also adds filters resulting in a combined filtering amplifier. By using this design approach, filters are designed together with transistor amplifiers without additional interconnections circuits. To enable this, an analytical design method for filtering amplifiers based on, the conventional passive coupling matrix for filters is expanded for the amplifiers filters. Novel coupled resonator circuits, including a general transistor model for the first time is investigated and a new $[T]$ matrix is introduced to facilitate this additional transistor element. Complete mathematical formulas are provided in this thesis for the coupled resonator circuits for transistor amplifiers.

Two physical design examples at X band are provided in this thesis to demonstrate the usage of the novel coupling matrix with a simple mathematical synthesis. One microstrip amplifier is demonstrated using hairpin resonators for 8.4 GHz centre frequency and 500 MHz bandwidth. A third order Chebyshev bandpass filter is integrated with the amplifier. In this microstrip circuit, the interconnection of the circuits between the filter and the amplifier is removed. In addition, a waveguide filtering amplifier is demonstrated using waveguide resonators. The transistor amplifier is integrated with a quasi-waveguide resonator via a waveguide-to-microstrip transition. This waveguide amplifier reflects the design considerations and methods for future THz amplifier developments. Good correlations between mathematical synthesis results and physical measurements are achieved for the waveguide filtering amplifier, with 3 clearly observed poles in passband, verifying the order of the filters.

ACKNOWLEDGEMENTS

Thanks the grace of God for giving me the passion, wisdom, confidence and faith in Him.

I would like to thank my supervisor Prof. Michael J. Lancaster for his constructive ideas, patient supervising and continuous support during my PhD study in the University of Birmingham. Without his assistance and encouragement, the work presented in this thesis may never have been accomplished.

My appreciation also goes to my colleagues Dr. Jeffrey Powell for his suggestions on active circuit design and assistance for measurements; Dr. Yingtao Tian for teaching me the micromachining techniques of SU-8 device; Dr. Xiaobang Shang and Dr Yuliang Dong for the fruitful discussions on filters, and Prof. Richard G. Humphreys for inspiration of matrix calculations during my studies at the University.

My gratitude also goes to all research group members for their friendships and support. I would like to thank the technicians Ms Donna Johnson, Mr Alan Yates and Mr Robert Davies for making and teaching me how to make my printed circuits boards.

I also appreciate the financial support from my family and the Engineering School Scholarship and Dudley Docker Research Scholarship from the School.

Last but certainly not least I want to express my greatest gratitude to my family and friends, and Birmingham Chinese Evangelical Church for their fellowship and prayers.

Knowledge puffs up, but love edifies.

1 Corinthians 8:1 (NKJV)

CONTENTS

1 Introduction **1**
1.1 Research Motivation 1
1.2 Thesis Organisation 3

2 Terahertz Communication Devices and Systems **5**
2.1 Introduction 5
2.2 Terahertz Applications 6
2.3 Terahertz Microwave Electronics 8
2.4 Terahertz Waveguides and Transmission Lines 10
2.5 Terahertz Micromachining Technologies 12
2.5.1 Micromachining Technologies 12
2.5.2 SU-8 Photoresist 13
2.5.3 SU-8 Applications 13
2.6 Terahertz Communication Propagations 14
2.7 Terahertz Wireless Communication Systems 16
2.7.1 Terahertz Communication System Block Diagram 16
2.7.2 Micromachined Communication System Concept 17
2.8 Terahertz Amplifier Concept 20
2.9 Summary 22

3 A WR-3 Band Rectangular Waveguide **23**
3.1 Introduction 23
3.2 Review of Submillimetre Rectangular Waveguides 23
3.3 WR-3 Band Waveguide Design Considerations 25
3.4 WR-3 Band Waveguide Bend Design 26
3.5 WR-3 Band Rectangular Waveguide Design 28
3.6 WR-3 Band Waveguide Layouts 29
3.7 WR-3 Band Waveguide Measurements 30
3.8 Discussions 35
3.9 Summary 40

4 Coupled Resonator Circuits for Transistor Amplifiers **41**
4.1 Introduction . . . 41
4.2 Coupling Matrix Review . . . 42
4.3 Coupling Matrix Synthesis . . . 42
4.4 The $n \times n$ Coupling Matrix for Coupled Resonator Filters . . . 45
4.5 The Small Signal Transistor Model . . . 48
4.6 The $(n + 1) \times (n + 1)$ Coupling Matrix for a Transistor integrated into the last Resonator . . . 49
4.7 The $n \times n$ Coupling Matrix for a Transistor between Resonators . . . 56
4.8 Two port network for S-parameters generation for the transistor coupled resonator circuit . . . 61
4.9 Summary . . . 63

5 Microstrip Bandpass Filtering Amplifier **64**
5.1 Introduction . . . 64
5.2 Review of Bandpass Filtering Amplifier . . . 65
5.3 A Simplified FET Small-Signal Model . . . 66
5.4 Microstrip Filtering Amplifier Design Overview . . . 68
5.5 Microstrip Filtering Amplifier Coupling Matrix Description . . . 70
5.6 Microstrip Filtering Amplifier Resonator Design using Coupling Matrix . . . 75
5.6.1 External quality factor extraction for Resonator 1 . . . 76
5.6.2 External quality factor extraction for Resonator 3 . . . 78
5.6.3 Coupling coefficient extractions for Resonator 2 . . . 80
5.7 Microstrip Filtering Amplifier Full Implementation . . . 82
5.8 Microstrip Amplifier Measurements and Discussions . . . 87
5.9 Summary . . . 90

6 Waveguide Bandpass Filtering Amplifier **91**
6.1 Introduction . . . 91
6.2 Integrated Waveguide Amplifiers . . . 92
6.3 Waveguide Filtering Amplifier Coupling Matrix Synthesis . . . 94
6.4 Waveguide Amplifier Coupling Matrix Design Process . . . 98
6.4.1 Extraction the external quality factor for Resonator 1 . . . 100
6.4.2 Extraction of the coupling coefficient for Resonator 2 . . . 101
6.4.3 Extraction of the external quality factor for Resonator 3 . . . 102
6.5 Waveguide Amplifier Simulated Design with a Transistor . . . 105
6.6 Microstrip Circuit for Waveguide Filtering Amplifier . . . 109
6.7 Waveguide Amplifier Fabrication . . . 113
6.7.1 Waveguide metal blocks . . . 113
6.7.2 Microstrip circuit for waveguide amplifier . . . 114
6.7.3 Waveguide amplifier assembly . . . 115
6.8 Waveguide Amplifier Measurements and Discussions . . . 116
6.9 Summary . . . 118

7 Conclusions and Future Work **119**
7.1 Conclusions 119
7.2 Future Work 123

A One-port measurement for external quality factor **125**

B WR-3 Rectangular Waveguide Fabrication Procedures **128**

References **130**

Chapter 1

Introduction

1.1 Research Motivation

Without direct wired connections, wireless communication systems transfer information between two points with sound, infrared, optical, radio frequency or microwave energy. This thesis focuses on the wireless communication systems using RF or microwave waves to propagate signals. Wireless communications have applications for broadcast radio and television, cellular telephone and networking systems, direct broadcast satellite television service, wireless local area networks, paging systems, Global Positioning System (GPS) service, and radio frequency identification systems [1]. This thesis focuses on the communication components and systems. For communication system circuits, current research has demonstrated a bandpass filter at the centre frequency of 700 GHz [2] at the University of Birmingham with the long term objectives of producing communication systems at terahertz frequency.

Wireless communication systems commonly require receivers with high selectivity using filters, for example, where channelisation is implemented or high power radiators are present adjacent to the receiver's band of interest. Additionally, low noise amplifiers (LNA) are the fundamental components for microwave communication system at the receiver ends. Achieving optimum performance for LNA designs requires two key criteria (i) optimum impedances are presented

to the active device, e.g., a transistor in order to minimise noise figure and simultaneously conserve the highest transistor gain; (ii) losses in transmission lines are minimised in matching and biasing circuits at the input of the transistor, where ohmic losses directly degrade noise performance for the overall microwave system. Examples of LNA designs can be found in the literature and on commercial datasheets using different technologies from almost DC and up to many hundreds of GHz [3–5]. Below 50 GHz, interfaces to the LNA circuits are 50 Ω using either microstrip or coplanar waveguide with on-wafer probable launching structures. Above 100 GHz, and even up to terahertz, waveguide module interfaces are required for measurements, therefore transitions between the planar amplifier circuit and the 3D waveguide are necessary. Recent circuits over 100 GHz have been demonstrated with transitions to waveguide included directly on the MMIC [6–10].

In each case of circuit designs, a matching strategy must be adopted to present the transistor with an impedance optimised for the target performance. Impedance matching techniques have been the subject of publications for many decades, examples are such as matching stubs, quarter-wavelength transformer, multisection quarter-wavelength transformers, line and stub transformers, are comprehensively summarised in the seminal texts [1, 11].

The central objective of this thesis is to describe a new design method for filtering amplifiers that can be incorporated as part of a coupled resonator structure, which can be described using a novel coupling matrix formulation with a transistor included. Using the formulation, it is demonstrated here that simplistic parameters of resonators, namely; external quality factors and coupling coefficients, extracted using simple electromagnetic modelling techniques, can be used to synthesise filtering amplifiers.

1.2 Thesis Organisation

This thesis has 7 chapters and the story begins by introducing terahertz communication components and systems. A micromachined terahertz communication system at 300 GHz is discussed. A demonstration of a WR-3 band (220-325 GHz) rectangular waveguide is presented with the fabrications and measurements. A combined resonator based matching and filtering approach for filtering amplifiers is proposed. A series of novel coupling matrices have been presented as the novel design approaches with two physical examples.

This thesis is organised as following chapters:

- Chapter 1 is the research motivation and the thesis organization.
- Chapter 2 gives an introduction about electromagnetic waves at the terahertz (THz) frequency range. Planar transmission lines and waveguides are introduced in the scope of terahertz frequencies. Reviews of THz wireless communication systems and the electronics are given. THz micromachining technologies are introduced with a focus on the SU-8 micromaching technology. A terahertz wireless communication system for 300 GHz is proposed with its block diagram and its possible physical realisation using micromachined circuits. A concept for micromachined THz amplifiers is also provided.
- Chapter 3 presents a complete example for a THz micromachined device using SU-8 photoresist; a WR-3 band rectangular waveguide with novel bends in order to match the waveguide measurement flanges. A review of waveguide circuits at submillimetre and THz is presented. The design using the computer aided simulation software for the waveguide and the waveguide bend is given. Measurements are carried out with a vector network analyser and the measurement results indicate the waveguide insertion loss is better than 0.031 dB/mm which can match the best reported pure metal micromachined waveguides at the same operating frequency.

- Chapter 4 deals with coupling matrices. Coupling matrices derived from coupled resonator circuits are reviewed for microwave passive circuit designs such as filters, antennas and multiplexers. Synthesis based on lowpass Chebyshev prototype filter and optimisations is presented. Novel coupling matrices for coupled resonator circuits which include a small signal transistor model are given. A novel $[T]$ matrix is introduced to describe transistor characteristics. Physical implementations using the novel coupling matrices are given in Chapter 5 and Chapter 6.

- Chapter 5 demonstrates an X-band third order microstrip bandpass filtering amplifier based on hairpin resonators. The coupling matrix description for the microstrip filtering amplifier is provided with the simple Chebyshev lowpass filter synthesis. Procedures on extractions of physical dimensions for external quality factors and coupling coefficients are given. The measurement results are presented based on the fabricated microstrip circuit. The 3 poles in the return loss passband have been clearly observed.

- Chapter 6 demonstrates an X-band, centre frequency 9.1 GHz, and 400 MHz bandwidth, rectangular waveguide based amplifier with third order Chebyshev filtering characteristics. The coupling matrix description for the waveguide amplifier is provided. Extractions for physical dimension by external quality factors and coupling coefficients are presented during the design procedures. The planar microstrip circuit, where a transistor is mounted, is designed with associated stability and bias circuits. The waveguide structure and planar circuits are fabricated and assembled. Measurements are conducted with a vector network analyser and measurement results agree well with 3 poles clearly observed in the passband. The design reflects the considerations for the 300 GHz amplifier introduced in Chapter 2.

- Chapter 7 concludes the whole thesis. Some suggestions are given for future work.

Chapter 2

Terahertz Communication Devices and Systems

2.1 Introduction

Since the introduction of the first wireless communications in 1901, electromagnetic waves have been used for telecommunication over long distances. Nowadays, mobile device users are consuming increasing data traffic to approach those Internet-based resources and multimedia services available in the conventionally accessed wired-networks. It is predicted that voice and data traffic on mobile networks will grow more than 30-fold during 2010-2020 in China, India and Europe [12]. It is also reported that the annual growth rate of mobile data traffic in Japan is around 71% and mobile traffic in 2017 will be 220 times more than that in 2007 [13]. In the US, 2015 will see a rising rate of 117% of the mobile traffic reaching 327 PB (1 Peta Bits = 10^{15} bits) monthly, which is 40 times more than that in 2010 [13]. Large data capacity communication systems, over 10 Gb/s or even faster, are required to match the requirements. Data capacity can be improved by increasing the spectral efficiency by advanced modulation schemes and signal processing technologies. However, the fundamental limitation of narrow bandwidth makes it very difficult to reach a data capacity over 10 Gb/s [13]. Several possible wireless

communications systems have been reported such as ultra wideband system (UWB) [14] to increase the bandwidth, 60 GHz microwave systems [15–17], free-space optical communication systems [18, 19] and terahertz wireless communication systems [20–24].

The terahertz (THz) frequency region refers to the electromagnetic spectrum that lies between the microwave and the optical from 300 GHz to 10 THz with the equivalent wavelength of 1 millimetre to 30 micrometres [25]. By increasing the operating frequency of microwave systems into the terahertz frequency range, systems can benefit with wider transmission bandwidth for communications. Terahertz wireless communication systems have drawn attention for academic research and industry application [13, 21, 26–29] for over ten years, with devices and systems attracting many publications in [10, 30–33].

In this chapter, terahertz technology is introduced with the electromagnetic waves used for security, medical and communications applications. A review of terahertz wireless communication systems is discussed, as well as terahertz microwave electronics such as mixers and amplifiers.

2.2 Terahertz Applications

Generally, the applications of THz systems can be treated in three categories: security, medical and wireless communication. This thesis particularly has a interest in the THz wireless communication application.

1. Security Applications

   Terahertz radiation systems can generate electromagnetic waves which can penetrate dielectric materials such as paper, plastic, cloth, wood and other the common packaging materials, yet are blocked by metals. Chemical and biological bodies can be detected by terahertz radiation with the unique spectrum. Airport and railway stations can be equipped with the terahertz systems to offer additional non-destructive testing methods to detect possible hazardous items from personal belongings [34]. Additionally, THz can stimulate molecular and electronic motions in many materials, revealing hidden weapons

or materials [23, 25, 35].

2. Medical Applications

   Radiation such as X-rays can cause harm to the health and risk due to its high energy and long exposure to create ionisation of biological tissue [36]. THz radiation from active imaging systems can hardly cause any health hazard as it is not ionising, and the radiation can be well controlled to very low radiation power [36]. The wavelength of THz radiation is short enough to display medical images of resolutions better than 200 micrometres, at 3 THz, and it is achievable with 40 micrometres at higher frequencies [37]. Most adult cancers such as skin, lung, liver, breast, colon, bladder and prostate can be detected by THz radiations [38]. THz spectroscopy systems have been used to characterise DNA and proteins as well [39]. Additionally, THz radiation can check tooth decay [23, 35].

3. Wireless Communication Applications

   Some reviews on the THz communication systems are available in [13, 21, 26–29]. System considerations are given in [22] about how to plan a short range communication system. THz wireless communications may be used in a similar way to most common systems for much larger data capacity. THz communications have potential applications such as wireless displays, transfer for high definition content, backhaul traffic in a mesh or point to point communication, lecture theatres or auditorium deployments. Future THz communication systems with potentially over 10 Gb/s can be used to transfer uncompressed high-definition television (HDTV) contents with 1920×1080 resolutions requiring 3 Gb/s, and even for Super Hi-Vision of 7680×4320 resolutions requiring 24 Gb/s data rate [13, 40, 41]. A triple-stack nano-cellular architecture has been proposed where cellular, WiFi and THz communications are installed in parallel with a balance of wide coverage with a slower rate from cellular and WiFi systems and high data rate communication via THz systems [42]. THz communications can be applied to link computer

clusters [43]. THz communication systems with high order encryption can be a candidate for a secure wireless system in battle fields. With highly directive antenna and high atmosphere losses, THz communication system can be made reasonably secure from jamming attacks. [23].

There have been some reported communication systems. In [44], a 220 GHz wireless communication system can transmit data at 20 Gbit/s to the distance of 100 metres. In [20], the authors show a terahertz wireless link at 300 GHz over a 50 cm long distance with data rate beyond 12.5 Gb/s using a Schottky barrier diode detector integrated with a planar antenna. Another instance in [45] of the transceiver communication system reached a data rate of 12.5 Gbps with bandwidth of 30 GHz at a carrier frequency of 307.2 GHz over a 2 metre range with a binary phase shift keying (BPSK) communication link.

2.3 Terahertz Microwave Electronics

Microwave electronics for THz communication systems have been reviewed in [30–33]. For the components aspects of the transceiver, several [6, 7] have been developed with the SiGe technologies working around 170 GHz. Waveguide mixers have attracted a lot of publications [46–54], and some examples are reviewed here. Planar GaAs mixer diodes have been used for frequencies of at least 600 GHz and they are expected to reach higher THz frequencies [8, 9]. A micromachined waveguide mixer with integrated horn antenna and a hybrid-integrated planar Schottky diode operating at 600 GHz on a quartz substrate have been manufactured by both micro mechanical milling and silicon etching technology [55]. With the standard semiconductor fabrication processes, a 585 GHz fundamentally pumped Schottky mixer [56] has been demonstrated with micromachining technologies. It has an etched silicon horn, a diced waveguide and a lithographically formed microstrip channel for the diode circuits. A combined sub-millimeter wave mixer/doubler consists of a 380 GHz sub-harmonic mixer and a 190 GHz frequency doubler on a single quartz of microstrip circuit has been developed [10], which were realised by

separate flip-chip mounted planar Schottky diode components. A fixed tuned 600 GHz heterodyne mixer in split-block waveguide technology has been developed based on a single planar GaAs Schottky diode on a quartz substrate [53]. A 520-590 GHz crossbar balanced fundamental Schottky mixer has been reported, whose circuit was fabricated on a GaAs membrane mounted in a split waveguide block [54].

There are a number of new mixers using the superconductor-insulator-superconductor (SIS) technologies [57–60]. For instance, a 400-500 GHz balanced SIS mixer with a waveguide quadrature hybrid coupler has been designed and measured at 4 K with good performance [57]. The balanced mixer topology was important to heterodyne receivers at sub-millimetre and terahertz frequency range with little LO power required [57, 59]. Hot electron bolometer (HEB) [61–64] is another popular technology for THz waveguide mixers. A balanced waveguide (HEB) receiver has been developed for telescope application at the frequency band of 1.25-1.39 THz with a quadrature balanced scheme and two HEB mixers on NbN film deposited on crystalline quartz substrate. A 250 GHz sub-harmonic mixer design has been achieved by electromagnetic band gap (EBG) technology, which has improved the radiation features of a dipole antenna for coupling the mixer. The EBG technology is based on the use of periodic structures to control electromagnetic propagation [65]. Most millimetre and submillimetre wavelength receivers in radio astronomy use double-sideband mixers to downconvert the RF signal to the intermediate frequency [66]. Single-chip or Monolithic Microwave Integrated Circuit (MMIC) balanced and sideband-separating mixers for 200-270 GHz have been developed [67]. With the SU-8 polymer, an integrated optical mixer was designed and fabricated [68]. For THz electronics such as mixers, sophisticated and high cost micromachining technologies have been used. MMIC circuits are used to achieve the planar circuit designs to accommodate the diodes and waveguide structures serve as packaging and measurement interfaces. Similar design considerations are applied to THz amplifiers as well.

THz amplifiers have been widely studied [4, 5, 32, 69]. A InP MMIC amplifier for 300-345 GHz

is described in [4]. It has 5 dB gain for the single-stage at 340 GHz and 13-15 dB gain from 300-345 GHz for the three stages S-MMIC amplifier. In [5], an H-band sub-millimetre wave monolithic integrated circuit (S-MMIC) amplifier has been developed around 300 GHz by using metamorphic high electron mobility transistor (mHEMT) technology with grounded coplanar waveguide (GCPW) circuit topology. The whole gain (four-stages) is over 12 dB in the range of 264-300 GHz with each stage having a 5 dB gain. Another HEMT amplifier module [70] with integrated waveguide transitions at over 300 GHz has been developed, this was monolithically fabricated with a MMIC for high performance with low loss. Also, a MMIC-to-waveguide transition is designed, integrated on the MMIC. The module can supply over 10 dB gain [70].

2.4 Terahertz Waveguides and Transmission Lines

Figure 2.1 shows the loss per wavelength against frequency for microstrips, coplanar waveguides and rectangular waveguides. The dimensions of the transmission lines and waveguides are scaled according to the increasing frequencies. It shows that the loss of transmission lines will increase with the frequency [33]. Several transmission lines and waveguides have been investigated such as microstrips, coplanar waveguides (CPW) and rectangular waveguides for frequencies from microwave up to terahertz ranges. Planar transmission lines are evaluated using different substrates for different frequency ranges. In the THz frequency range, micromachined rectangular waveguides have superior low loss property over planar transmission lines such as microstrips and CPWs, which makes them optimal solution for THz systems.

Planar transmission lines (e.g., microstrip, coplanar waveguide) can experience losses associated with finite conductivity of metals, dielectric material loss tangent, and radiation. The conductor loss is proportional to the square root of the frequency. The dielectric loss is proportional to the frequency, and at higher frequencies, the metallic conductor loss is less important than the substrate associated loss for planar transmission lines [71]. Traditional planar circuits also suffer from significant radiation losses and dielectric losses as well as the losses from the

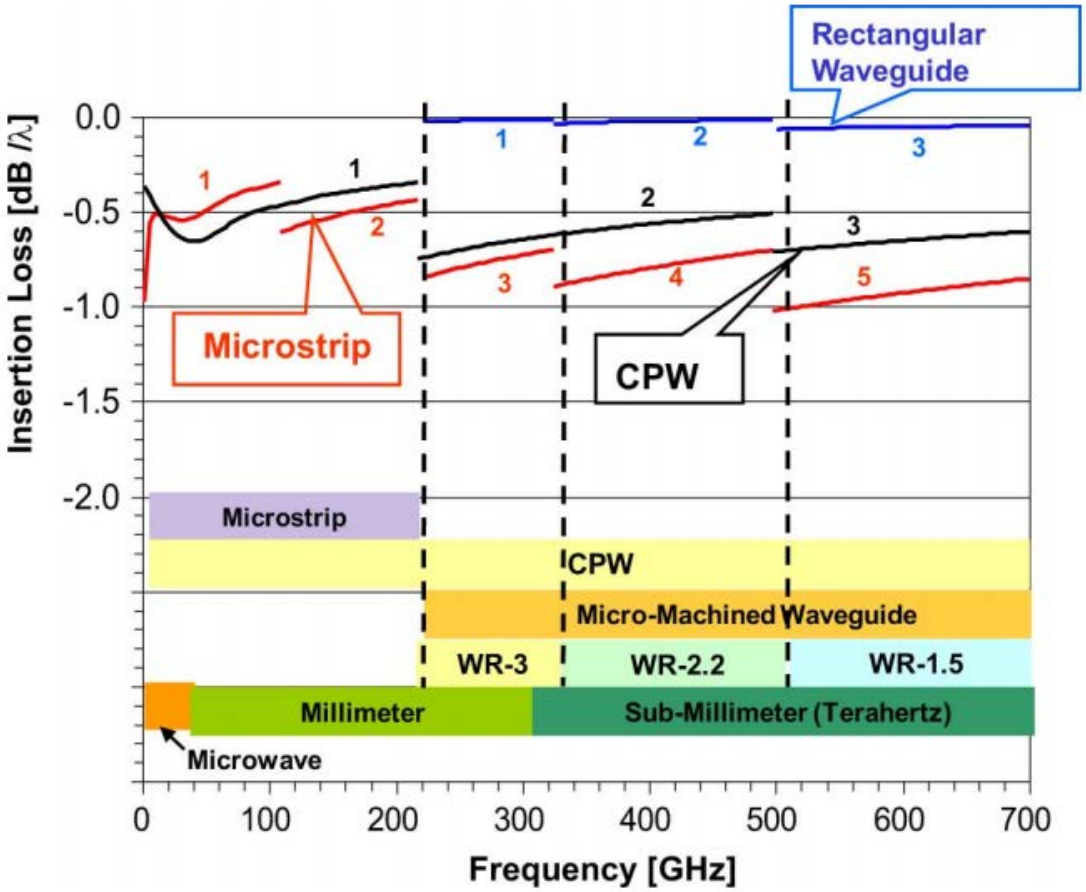

Figure 2.1: Loss per wavelength for transmission lines and waveguides versus frequency, taken from [33].

dispersion [72]. As planar transmission lines such as microstrip are not shielded, they also face the problems such as spurious cross-coupling or detrimental parasitic modes such as the dielectric-related surface waves.

A shielded and dielectric-free transmission line or waveguide with well-shielded 3 dimensional structure can be a good solution to the problems for a system at high frequencies, for instance, THz systems. The shielded structures have lower conductor losses due to a spread in the surface current distribution. By removing the dielectric, the dielectric losses and dielectric-related parasitic modes are eliminated. For example, air filled coaxial transmission lines or waveg-

uides offer no dielectric loss and the enclosed 3 dimensional structure can limit the radiation losses in higher operating frequencies [73, 74]. Surface roughness is an another factor that can cause losses to waveguides and transmission lines. The rough surface can increase the conductor loss, particularly in higher frequency ranges. Although planar transmission lines such as microstrips and CPWs have become widely used for submillimetre application due to the fabrication simplicity and integration convenience, rectangular waveguides are still of importance in THz systems, for the losses of waveguides are significantly less than those of planar transmission lines.

2.5 Terahertz Micromachining Technologies

2.5.1 Micromachining Technologies

Conventionally, passive microwave components at frequencies of tens of GHz such as waveguide circuits are fabricated by computer numerical controlled (CNC) metal milling technology. When the operating frequency of the circuits or systems increases, the physical sizes of the circuits are scaled down according to the frequencies. CNC micromachining technology has been used to fabricate submillimetre wave devices operating up to 1.5 THz with accuracy of 2-3 μm tolerance [75, 76] with capacities of 15 μm wide channels on a solid metal block. Although the CNC machining approach can produce components with very high dimensional precision, it is limited by its increasing cost according to the shrinking feature sizes, achievable aspect ratio due to the mechanical limitations of the milling cutter strength and the rounded corners due to the cutter diameter [77–79]. To fabricate these high frequency components (e.g. over 100 GHz), the CNC metal milling method will cost a lot more time than low frequency components (e.g. 10 GHz). Sometimes it is not even possible to achieve complicated structures. It is known [73, 80] that photolithography based micromachining technologies are feasible fabrication methods with features of high dimensional accuracy, high achievable aspect ratio structures and capability of low-cost mass scale manufacturing [81]. Some of the micromachining technologies for

thick layer (50 to 2000 μm) or 3-dimensional fabrication are listed as metal coated plasma-etched silicon [82, 83], silicon deep reactive ion etching (DRIE) [79, 79, 84–87], Lithographie, Galvanoformung, Abformung (LIGA) [88–91] and SU-8 photoresist micromachining [92–95]. Particularly, thick SU-8 photoresist micromachining technology has an achievable aspect ratio of ~1:50, which is generally superior to other micromachining technologies. e.g., silicon DRIE [73, 95–97]. One advantage of this SU-8 lithography micromachining approach is its simple process with normally one etching step for great dimensional accuracy, and relatively low demand for expensive fabrication facilities [98]. More miniaturised or complex devices demanding more design effort may not necessarily increase the SU-8 fabrication complexity. The SU-8 micromachining technology has been used to fabricate THz communication devices and systems, and brief fabrication procedures are available in [74, 80, 99, 100]. SU-8 is used in this thesis.

2.5.2 SU-8 Photoresist

SU-8 was developed and patented by IBM as a negative, epoxy based, near-UV photoresist which can be processed by standard photolithography techniques. SU-8 is transparent with a low UV absorption property which can be penetrated with a uniform exposure into large depth. Ideally, vertical sidewall profiles are achievable if the UV exposure can transmit through the photoresist without any losses. SU-8 is photo sensitive to 350 to 400 nm [100] which means that it can be processed under conventional photolithography facilities. Although, LIGA can provide better resolutions to sub-micrometre dimensions using X-rays for photolithography with special expensive masks, SU-8 photoresist micromachining is a better cost-effective and precision technology. SU-8 is also thermally stable which makes it a good mould for electroplating [101].

2.5.3 SU-8 Applications

There are many applications using SU-8 [94, 102–104], and some of the examples are provided here. Applications using SU-8 photoresist micromachining have been reported in mi-

crofluidics [102, 105] with the multi-layered fabrication techniques where two SU-8 layers are produced in one processing step. An electrospray tip for mass spectrometry has been reported fully fabricated with three layers of SU-8 photoresist producing stable electrospray for hours with pressure driven flow [106]. Also, SU-8 micromachining technology can fabricate microwave devices and systems as thick layered structures. The metal (silver/gold) plated SU-8 devices can give decent electromagnetic performances compared to CNC metal machined devices [80]. The SU-8 photoresist has been utilised to fabricate microwave antennas such as horn antennas [107–109], dielectric resonator antenna [110], monopoles by self-assembly [111] and slotted waveguide antenna [112]. Additionally, it has been used to fabricate microwave passive circuits such as filters up to 700 GHz [2, 80] and rectangular coaxial cable [73]. SU-8 based micromachined planar transmission lines have been shown with no dielectric, which allows lower loss and the removal of any substrate associated modes [73].

2.6 Terahertz Communication Propagations

For outdoor propagation, the atmosphere and weather are the primary factors which matter for the attenuation, phase shift and angle of arrival variations on the electromagnetic waves. With the increasing operating frequencies of the systems, the influence from atmospheric properties and absorptions on THz communication is more significant. The microwave systems such as communication, radar and radiometry systems can be seriously affected by propagation effects such as reflection, refraction, attenuation or diffraction. Atmospheric attenuation is caused mainly by the absorption of microwave energy by water vapour or oxygen molecules. When the electromagnetic waves at a frequency resonates with one of the molecules of water or oxygen, the absorption is maximum with distinct peaks [1].

Figure 2.2 shows the relationship between atmospheric attenuation levels and the frequencies. The atmospheric attenuation effect can be ignored at frequencies below 10 GHz. Two resonance peaks appear at 22.2 and 183.3 GHz due to the water vapour. Frequencies at 60 GHz and 120

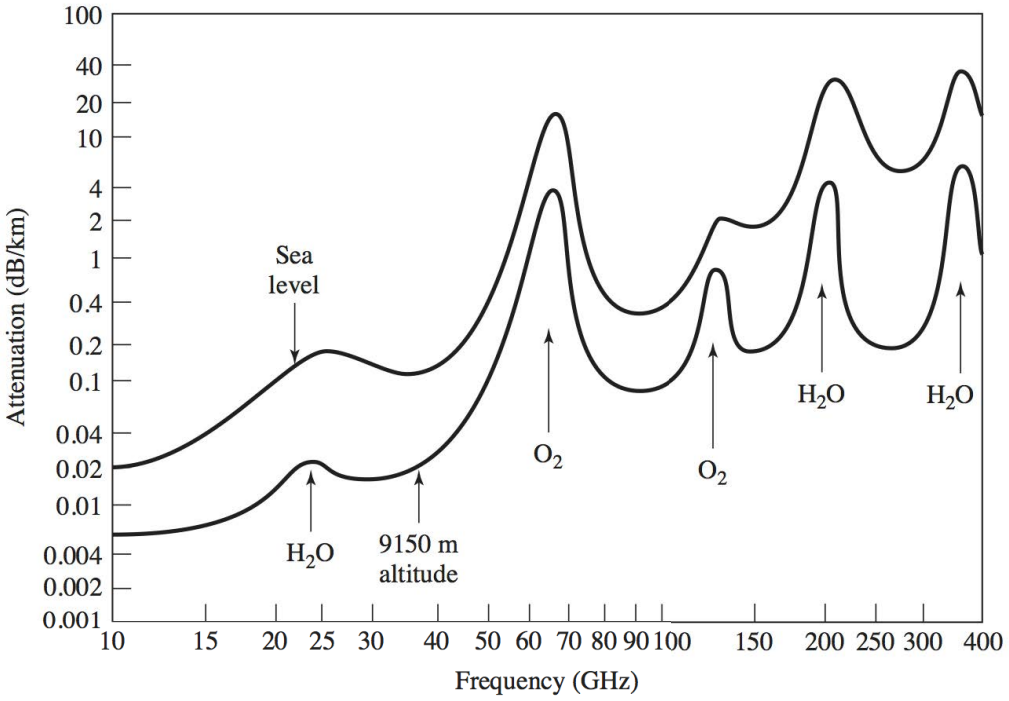

Figure 2.2: Average atmospheric attenuation versus frequency, taken from [1].

GHz see the maximum absorption caused by molecular oxygen. Radar and communication systems can operate with minimum loss at frequencies of 35, 94, 135 GHz which are called the 'windows' in the millimetre wave band, and around 300 GHz in the terahertz range.

The attenuation from rain for the frequencies beyond 300 GHz depends only on the rain rate and the loss is up to 100 dB/km [22]. The attenuation from fog and clouds depends on the frequency and droplets concentration, and can reach up to tens of dB/km. Scintillation occurs outdoor which manifest itself in rapid amplitude fluctuations of the propagation, causing attenuation of a few dB/km. With the considerations of free space path loss in varying weather conditions, the THz communication systems are likely to be applicable for short range outdoor or indoor communications [22].

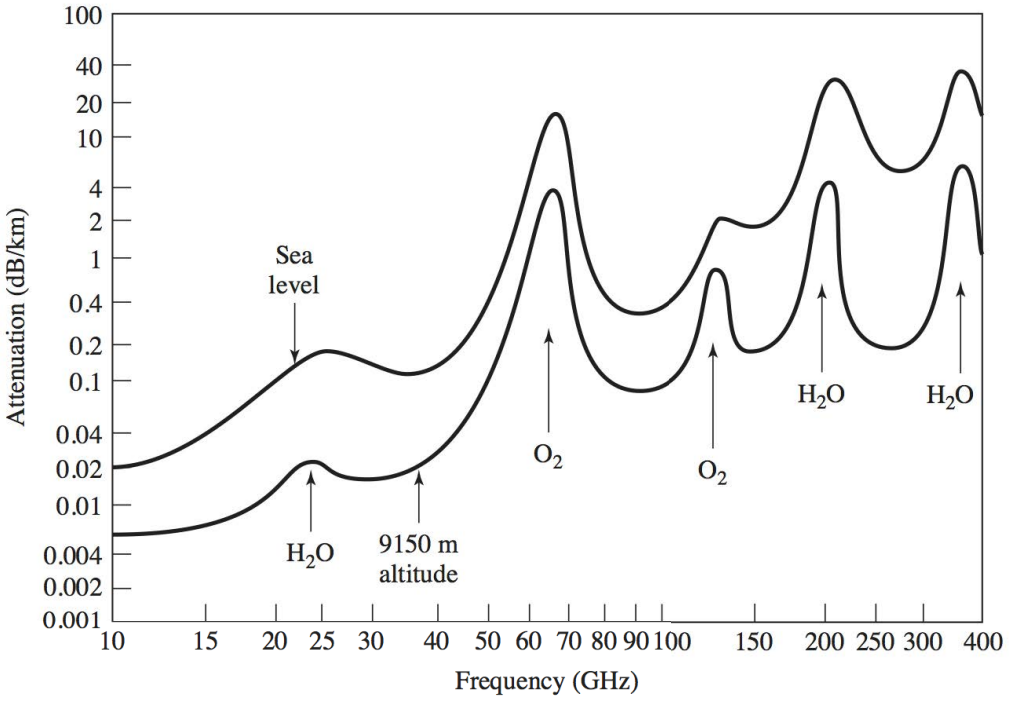

Figure 2.2: Average atmospheric attenuation versus frequency, taken from [1].

GHz see the maximum absorption caused by molecular oxygen. Radar and communication systems can operate with minimum loss at frequencies of 35, 94, 135 GHz which are called the 'windows' in the millimetre wave band, and around 300 GHz in the terahertz range.

The attenuation from rain for the frequencies beyond 300 GHz depends only on the rain rate and the loss is up to 100 dB/km [22]. The attenuation from fog and clouds depends on the frequency and droplets concentration, and can reach up to tens of dB/km. Scintillation occurs outdoor which manifest itself in rapid amplitude fluctuations of the propagation, causing attenuation of a few dB/km. With the considerations of free space path loss in varying weather conditions, the THz communication systems are likely to be applicable for short range outdoor or indoor communications [22].

2.7 Terahertz Wireless Communication Systems

2.7.1 Terahertz Communication System Block Diagram

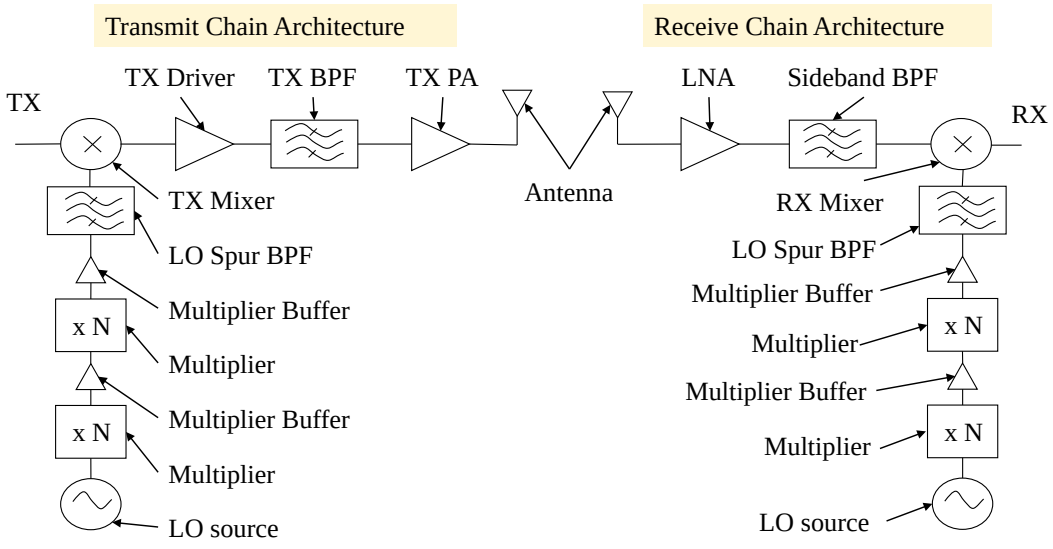

Figure 2.3: THz communication system block diagram, reproduced from [113].

Figure 2.3 gives the block diagram of a terahertz communication system. The research vision is to build a terahertz communication system with a transmitter and a receiver at 300 GHz with over a 10 metre link made with micromachined components, e.g., SU-8 micromachining technologies [113]. The receiver and transmitter chains of communication systems share common components such as antennas, filters, mixers, amplifiers for different architectures [1]. At the transmit chain, signals are converted by a mixer, and then it is amplified by a driver amplifier. A bandpass filter is included into the main route of the transmitter architecture to provide selectivity and remove unwanted sideband harmonics from the mixer. Step multipliers are included for the local oscillator with multiplier buffers. The signal is transmitted with a high gain antenna towards the receiver chain. On the receiver end, the signal is received by an antenna then amplified by a low noise amplifier. The amplified signal passes through a sideband bandpass filter

to have better selectivity for the system and remove interference. The signal is then converted by a mixer for further signal processing.

2.7.2 Micromachined Communication System Concept

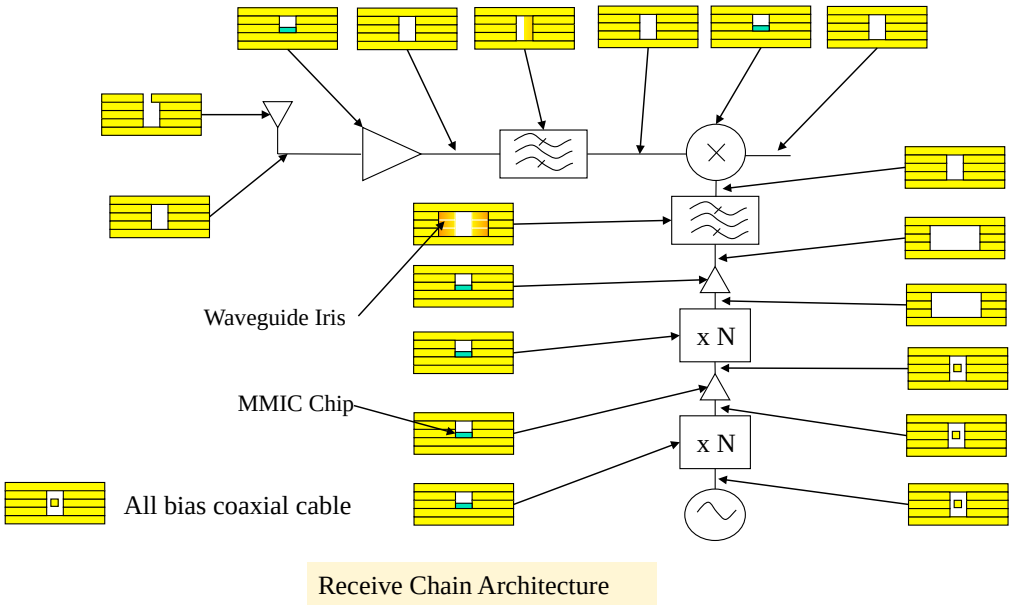

Figure 2.4: Proposed THz Communication System Receive Architecture based on SU-8 micromachining, reproduced from [113].

Figure 2.4 illustrates the micromachined and layered physical realisation concept for the receiver end for the system block diagram given in Figure 2.3 previously. The transmitter end will have similar construction. The whole THz communication system is proposed to be built with multilayer structures based on SU-8 photoresist, which can be fabricated with the SU-8 micromachined technologies [80]. The whole system including filters, amplifiers, mixers, multipliers and antennas can be integrated with the 5 layer micromachined process. The communication system is based on rectangular waveguide with the standard WR-3 band (220-325 GHz) with aperture size 0.864 mm by 0.432 mm. Each SU-8 layer shares common thickness of 0.288 mm, and 3 cascaded layers form the long side of the WR-3 waveguide for 0.864 mm.

The 5 layered structure can provide a coaxial cable [73] for the local oscillation (LO) sources as well as providing waveguide pedestals for mounting the active components or chips into the rectangular waveguides.

At the Emerging Device Technology (EDT) Group at the University of Birmingham, several passive components have been designed, fabricated and measured using the SU-8 micromachining technologies [73, 80, 112, 114, 115], and those components can be used for the THz communication systems.

Up to now, straight rectangular waveguides have been demonstrated with comparable loss performance versus CNC gold plated waveguide [80, 114]. System components such as a rectangular waveguide (Chapter 3), waveguide iris filters [115], micromachined layered coaxial cables [73] have also been demonstrated successfully for the THz communication system. Those components and circuits lay the foundations for the terahertz communication system based on SU-8 photoresist micromachining technologies and some examples are:

* A micromachined WR-3 (220-325 GHz) waveguide iris filter using SU-8 photoresist operating at a centre frequency of 293.2 GHz with insertion loss of 3.3 dB and measured return loss better than 16 dB [115].

* A micromachined rectangular waveguide operating at 300 GHz with measured return loss of -20 dB and a normalised insertion loss of 0.031 dB/mm [80, 99].

* A micromachined 300 GHz SU-8 slotted waveguide antenna is presented with the measured 5 dB gain [112].

* SU-8 based micromachined coaxial cables have been demonstrated which can be used as bias coaxial cable for mixers with full compatibility to SU-8 layered structures [73].

The remaining work required to produce the THz communication system focuses on high gain THz antennas, and implementing waveguide integrated circuits with active MMIC components

such as diodes and transistors for mixers and amplifiers. The THz antenna research has led to a publication in [116] and is still in progress in another research project [113].

A THz component concept based on SU-8 micromachining technology (e.g., amplifier) is described in the following section.

2.8 Terahertz Amplifier Concept

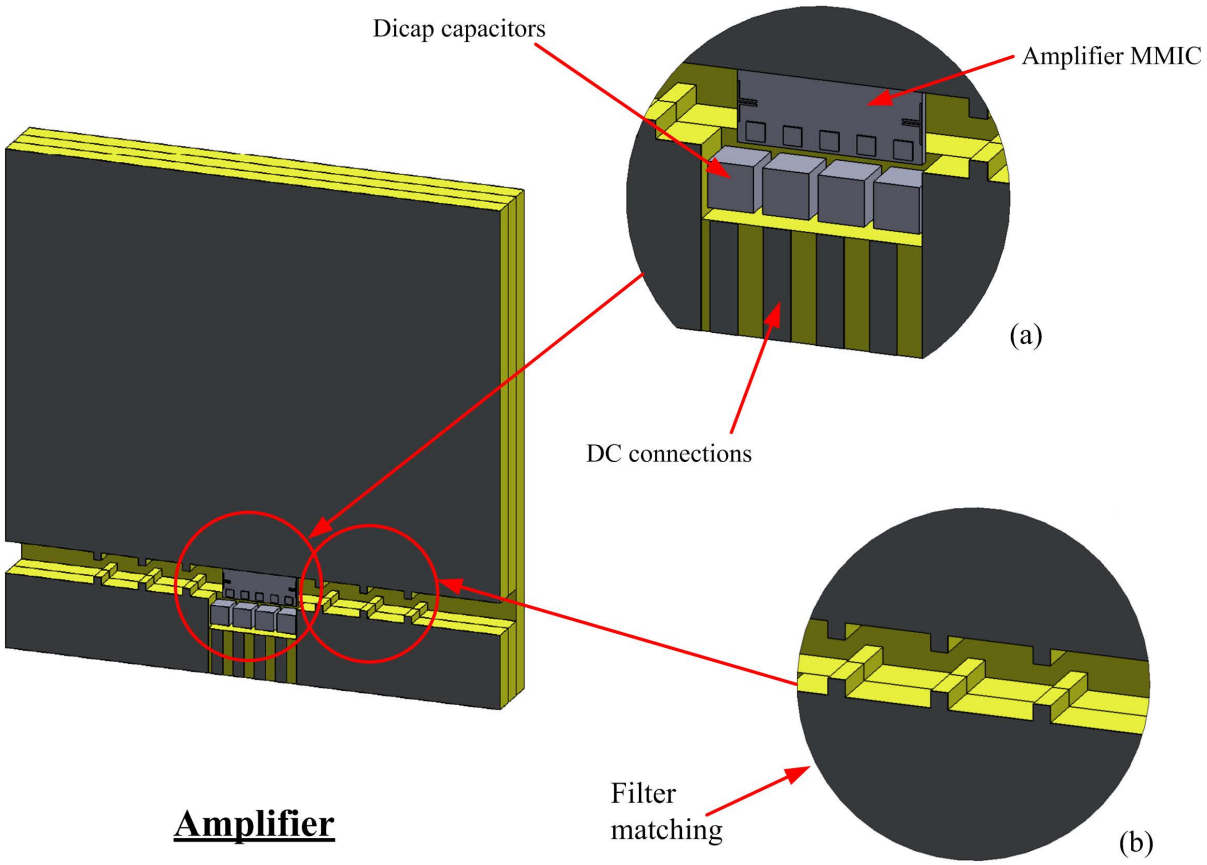

Figure 2.5: THz waveguide circuit concept: amplifier.

Figure 2.5 shows the THz amplifier circuit concept. They give the diagrammatic concept of the possible THz amplifier, however, they are not rigorous design considerations. The view shows the middle layer cascaded together with the other two adjacent layers. The EM waves enter from the input port and are filtered by the waveguide iris structure as illustrated in Figure 2.5 (b). As shown in Figure 2.5 (b), there is the filter matching network based on waveguide iris filter resonators. The signal is then coupled onto the planar amplifier chip as shown in Figure 2.5 (a) via the transitions. In Figure 2.5 (a), there are tracks to supply the DC current to drive the amplifier chip. On the amplifier chip shown in Figure 2.5 (a), two dipole antenna-like transitions are designed to couple the electromagnetic waves from the input and output ports. The amplifier

MMIC chip is bonded on the waveguide pedestal. Dicap capacitors can be mounted into the waveguide structure to decouple the DC signals. The amplified signals are then coupled from the planar circuit into the rectangular waveguide. The matching circuits for the amplifier input and output are not on the planar MMIC circuit but integrated into the waveguide iris and the microstrip-to-waveguide transitions.

2.9 Summary

In this chapter, terahertz technology is introduced with a literature review for terahertz systems presented in addition to THz electronics such as mixers and amplifiers. This chapter gives an insight into transmission lines and waveguide properties at terahertz frequencies. THz micromachining technology is reviewed and SU-8 micromachining technology is selected to implement physical devices. A simple THz communication system operating at 300 GHz is presented with its block diagram as well as the concept of the SU-8 micromachined structure. The concept of a THz waveguide amplifier is discussed.

A SU-8 THz rectangular waveguide in 5 layers is presented in Chapter 3 which experimentally verifies the performance of micromachined devices using SU-8 micromachining technologies. A novel active coupling matrix is introduced in Chapter 4 to describe the novel design approach by matrix synthesis which is briefly mentioned in this chapter. A demonstration of the amplifier design approach is presented in Chapter 6 for an X-band rectangular waveguide amplifier, in which conventional on-chip matching for a transistor is removed and completed in waveguide structure.

Chapter 3

A WR-3 Band Rectangular Waveguide

3.1 Introduction

Rectangular waveguides are widely used for high frequencies for their low loss properties. Chapter 2 has introduced a THz waveguide communication system concept operating at 300 GHz based on a SU-8 photoresist 5 layered structure. This chapter will discuss WR-3 band micromachined SU-8 waveguides as the fundamental device for the THz communication system. In this chapter, a review on submillimetre wave rectangular waveguides is given. SU-8 waveguides are demonstrated operating at WR-3 band from 220 GHz to 325 GHz. The details of the waveguide designs and measurements are provided including novel bends to match the waveguide measurement flanges.

3.2 Review of Submillimetre Rectangular Waveguides

A few publications are available on submillimetre wave rectangular waveguide components [80, 92, 93, 104, 112, 115, 117–122], and the performance of the waveguides have been reported. The best achieved insertion loss for WR-3 band waveguides is 0.02 dB/mm [80, 122] with gold plated metal waveguides machined by CNC. Some examples of waveguide components are listed below:

* A micromachined WR-3 waveguide filter with embedded H-plane back to back bends using SU-8 photoresist operating at a central frequency of 293.2 GHz with insertion loss of 3.3 dB and measured return loss better than 16 dB has been demonstrated by the University of Birmingham [115].

* Another micromachined waveguide with embedded bends for direct flange connections operating at 300 GHz with measured return loss of -20 dB and a normalised insertion loss of 0.134 dB/mm has been demonstrated [117]. In the design 4 layers of SU-8 pieces are used. The measured results show a return loss better than -16 dB and the lowest insertion loss of 2.5 dB for the frequency range from 260-312 GHz by the University of Birmingham.

* A micromachined 300 GHz SU-8 slotted waveguide antenna was developed with the measured gain of 5 dB at 295 GHz [112]. The device gives 0.25 dB loss for the 15 mm long feeding waveguide addressed in the paper by the University of Birmingham.

* In [104] a method to combine the photolithography and mechanical lapping fabrication technique to obtain a micromachining process to get better results than conventional fabrication for waveguide components at millimetre and submillimetre range is presented. A flange is CNC machined and SU-8 columns have been introduced with photonic band gap structures which offer better alignment between micromachined SU-8 circuits and the flanges with a simulated return loss below 15 dB by the University of Virginia.

* The paper [92] demonstrates a straight waveguide and a cylindrical cavity resonator based on SU-8 fabrication process. The measured return loss is better than 15 dB and the insertion loss is 1 dB for its length of 11.4 mm by the University of Virginia.

* A plastic rectangular waveguide operating at 95 GHz with an integrated plastic flange is demonstrated in [118]. It is made with micro hot embossing and electroplating fabrication

techniques. It has good S_{11} response of -20.7 dB and insertion loss S_{21} is measured -1.35 dB at 95 GHz by UC Berkeley.

* A micromachined waveguide twist of 0.8 inch length is presented with the return loss near 20 dB and the insertion loss about 0.5 dB from 600 to 750 GHz. The device is made by LIGA micromachining techniques [119] by the University of Virginia.

3.3 WR-3 Band Waveguide Design Considerations

This chapter discusses the design, fabrication and testing of a 5-layer SU-8 waveguide with embedded bends to enable connection to measurement equipment. With the requirement of the

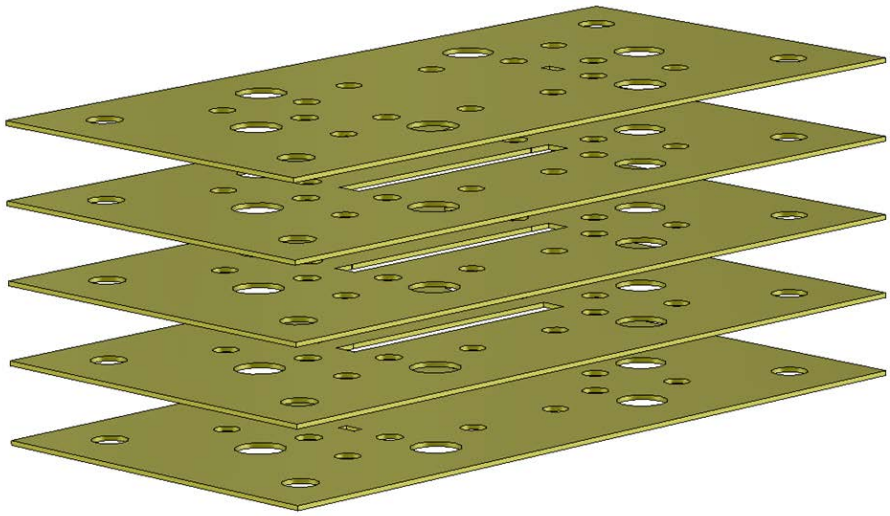

Figure 3.1: A SU-8 5 layer structure.

THz communication system concept in Chapter 2, the micromachined 5 layered structure by SU-8 photoresist is to be considered here as shown in Figure 3.1. A device using the SU-8 micromachining technology should be mechanically easy to fabricate, also mechanically robust with reliable structures. Electromagnetically, it should has low insertion loss and high transmission performance for the specified operating frequency bandwidth.

For this rectangular waveguide design, the specification for the reflection coefficient S_{11} is lower than -20 dB for the whole WR-3 band. The waveguide devices can be fabricated into 5 SU-8 individual pieces, and the fabricated pieces are sandwiched together with the specially designed rigid brass plates to accommodate screws and alignment pins for measurements [115]. With the double-layer fabrication techniques presented in [123], only 3 SU-8 processed pieces need to be fabricated instead of 5 individual pieces with the top and bottom 2 layers jointly fabricated.
A waveguide bend is required to match the waveguide measurement configuration at both input and output ports. Conventional metal rectangular waveguide bends follow large curves with optimal electromagnetics performance [1]. However, curved structure is not feasible for the lithography micromachining process based on SU-8 photoresist [99]. The novel rectangular waveguide bend is required which is designed on SU-8 with 5 layered structures. The waveguide device design starts from one side bend and the bend is then modelled and configured for the back-to-back structure with the required the length of 15.95 mm waveguide for the whole waveguide device to match previous waveguide device in the research group [115].

3.4 WR-3 Band Waveguide Bend Design

The rectangular waveguide bend is modelled and simulated with the 3D EM simulation software CST [124]. Several structures have been proposed for the optimal transmission and lowest reflections via simulation and optimisation. One design with modification of previous 4 layer design in [115] is used to accommodate the 5 layer design, and it is displayed with its simulation results in Figure 3.2 and Figure 3.3.
For the single bend in Figure 3.2, there are four layers with two waveguide ports. Figure 3.3 shows the simulation results. The whole WR-3 band can see better than -26 dB in S_{11} and -0.004 dB in S_{21}. This design shows better performance over [115] using more layers therefore gentler bend with small steps, with the varying width for a matching network. The design in Figure 3.2 is used because of its decent simulation performance and ease of fabrication.

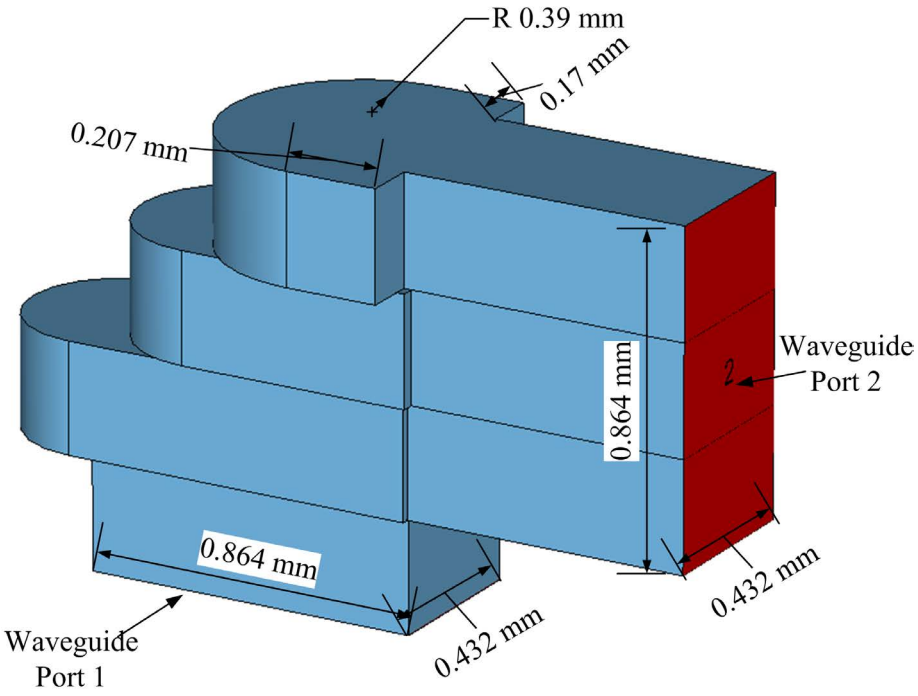

Figure 3.2: Modelled waveguide bend with curved shapes

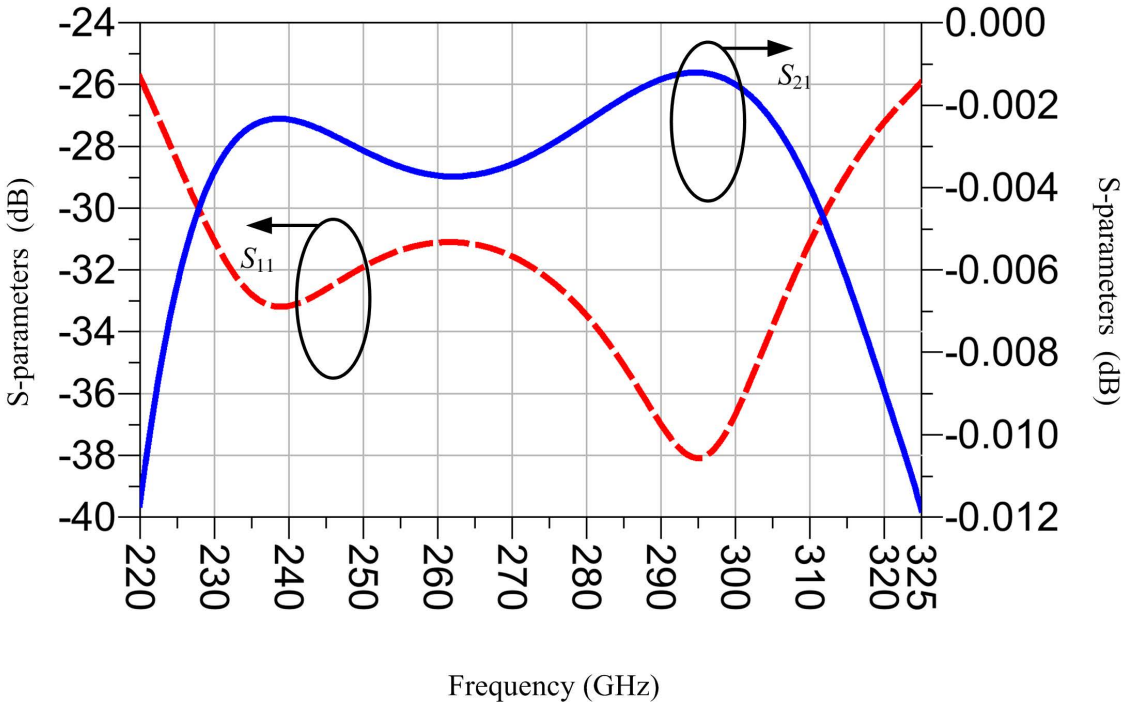

Figure 3.3: The simulation results for the waveguide bend with curved shapes.

3.5 WR-3 Band Rectangular Waveguide Design

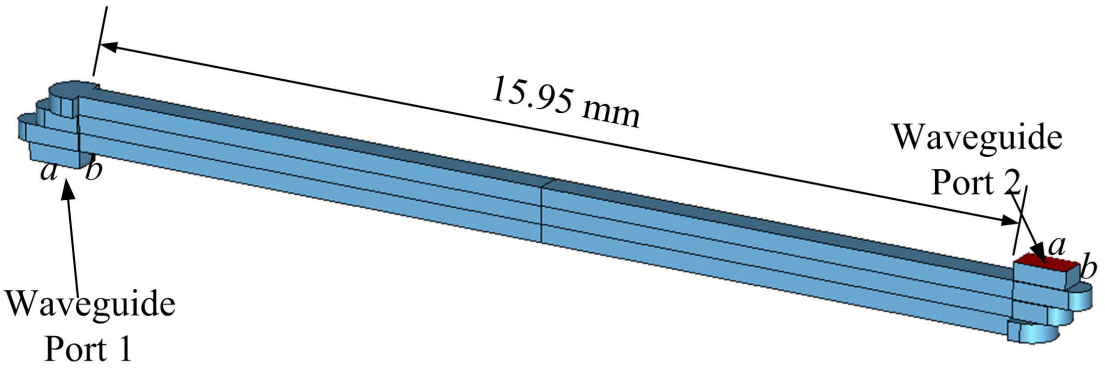

Figure 3.4: Modelled rectangular waveguide with bend structures.

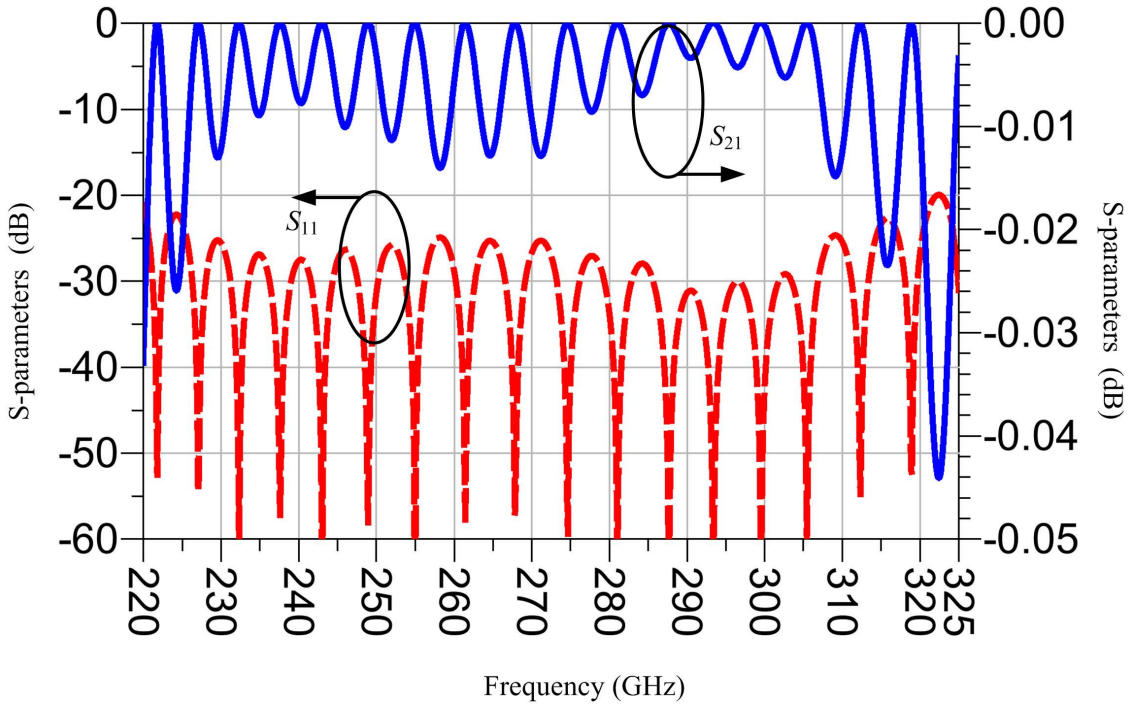

Figure 3.5: The simulation results for the modelled waveguide back-to-back bend.

To achieve the complete waveguide design, another identical waveguide bend is modelled at other end with a straight rectangular waveguide. Figure 3.4 shows the overall structure. Figure 3.5 shows the CST simulation results of the whole waveguide including two bends. The simulated waveguide has better than -20 dB S_{11} over the whole WR-3 band. The ripples in S_{11} are possibly generated by the reflected waves from the mismatched terminals. The waveguide length reflects the integer times of the half wavelength of the electromagnetic waves.

3.6 WR-3 Band Waveguide Layouts

Based on the rectangular waveguide model as shown in Figure 3.4, the layouts of the 5 SU-8 layers and their corresponding masks for micromachining photolithography are generated.

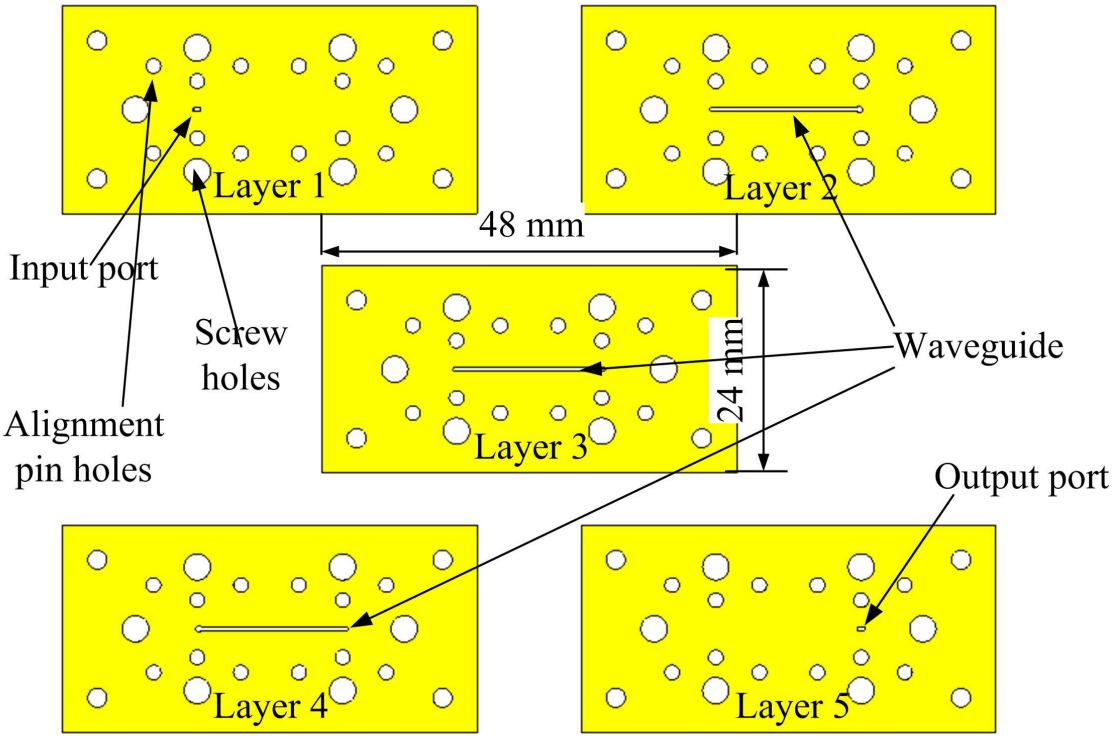

Figure 3.6: The pictures of SU-8 layers for the WR-3 waveguide.

There are five layers for the SU-8 waveguide and they are displayed in Figure 3.6. As the whole structure is symmetrical, Layer 1 and Layer 5 are identical as are Layer 2 and Layer 4.

3.7 WR-3 Band Waveguide Measurements

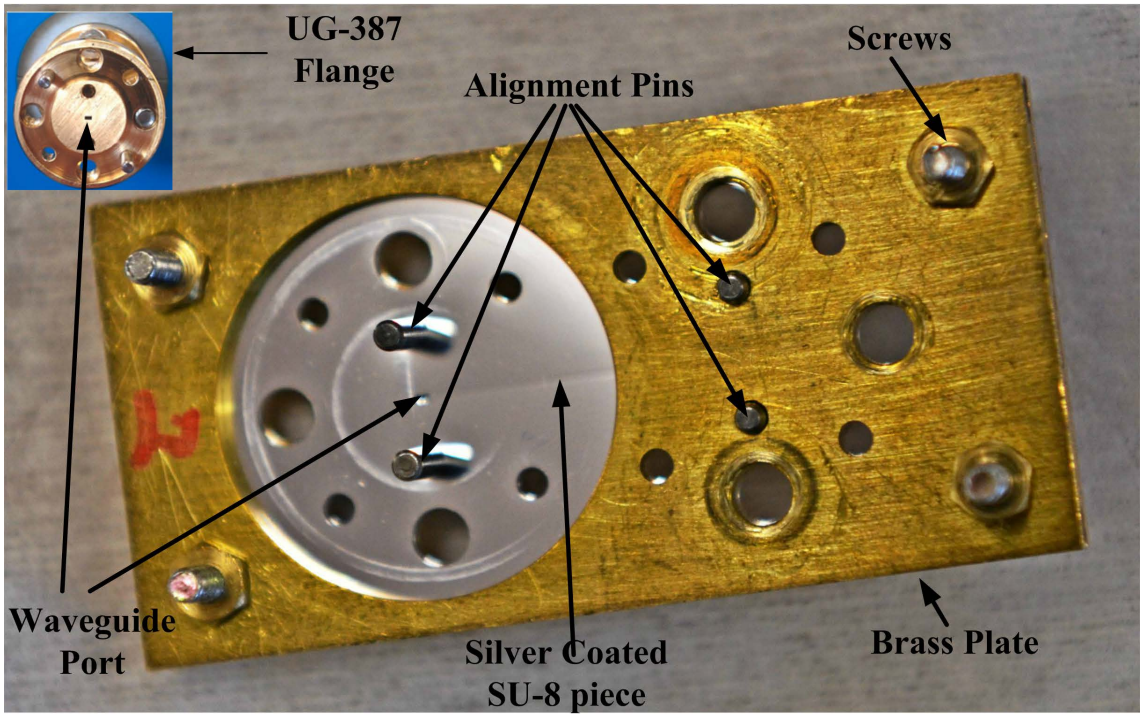

Figure 3.7: The photograph shows the first fabricated and assembled device WR-3 waveguide.

The SU-8 pieces for two separate waveguide devices are fabricated in the in-house 10,000 class clean room using the SU-8 micromachining technology [99], and then they are plated with silver on the external surfaces. Precision alignment pins provide accurate assembly alignment for measurements (see Figure 3.6), and bolts sandwich the layered waveguide structures between brass plates to minimise the gaps between layers. Fabrication details are given in Appendix B. Two waveguide devices have been fabricated and assembled. One of the circuits is shown in Figure 3.7. Air gaps between each fabricated SU-8 pieces become smaller when SU-8 pieces are assembled together with clamping brass plates, reducing the possible losses [103]. The main part of the device, including the SU-8 pieces and clamping brass plates, but not including the outstanding screws, occupies a volume of 48 mm $\times$ 24 mm $\times$ 8 mm. The measurement waveguide flange, UG-387, is displayed in Figure 3.7, which matches the waveguide device

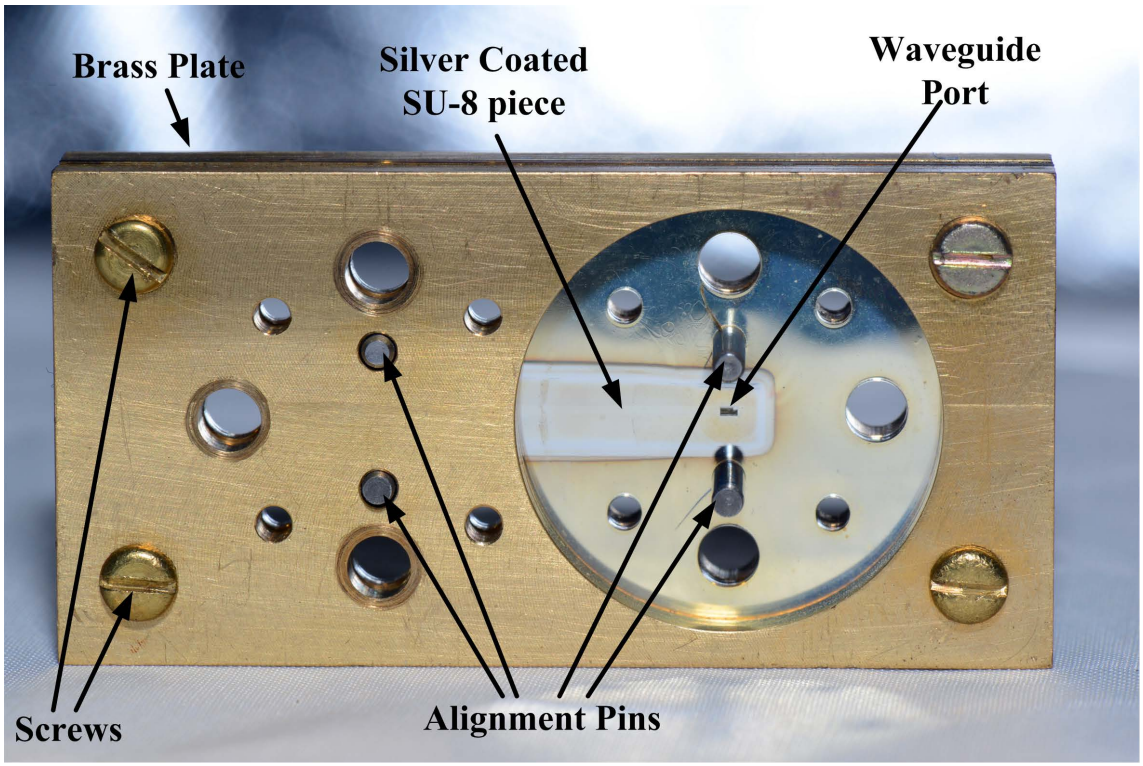

Figure 3.8: The photograph shows the second fabricated and assembled device WR-3 waveguide.

with precision alignment pins. Figure 3.8 shows another fabricated and assembled waveguide device, using the same micromachining and metal plating technologies.

The measurement configuration is shown in Figure 3.9. The measurement is carried out with the Agilent E8361A Vector Network Analyser with a WR-3 OML band extender T/R module at test Port 1 and a receiving only T-module at Port 2. Enhanced response calibrations are done before the measurements.

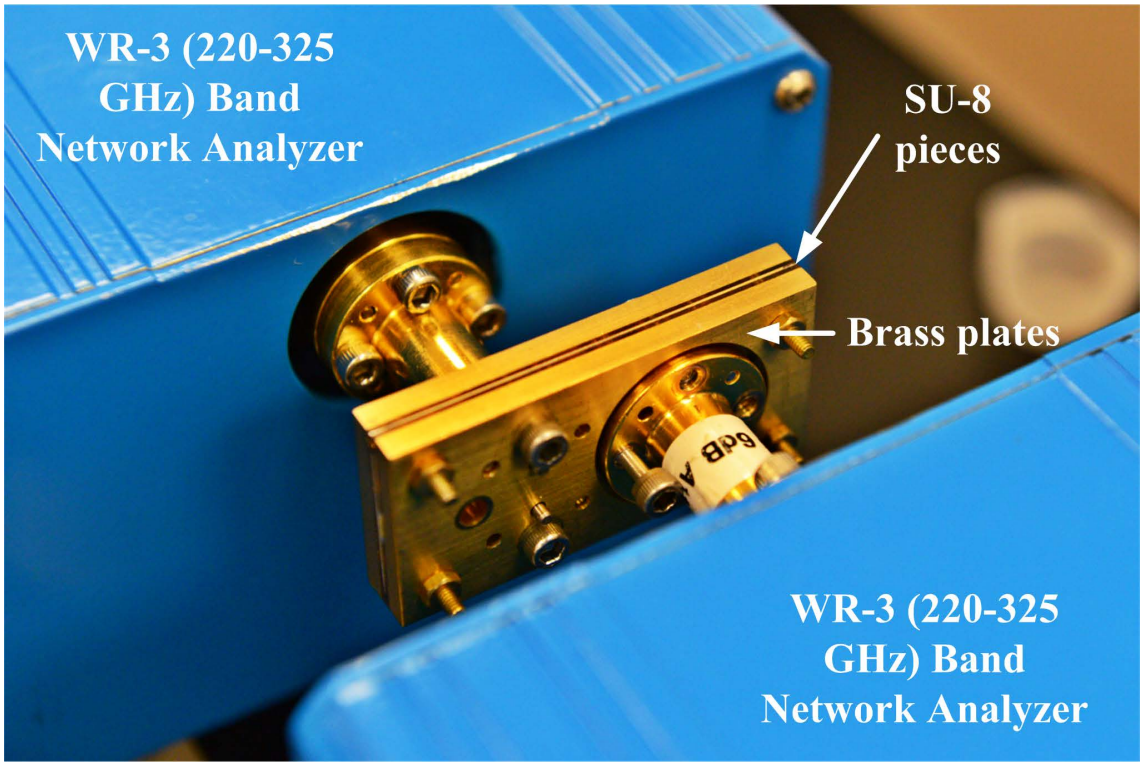

Figure 3.9: Measurement configuration: the WR-3 band waveguide under test with the Vector Network Analyser.

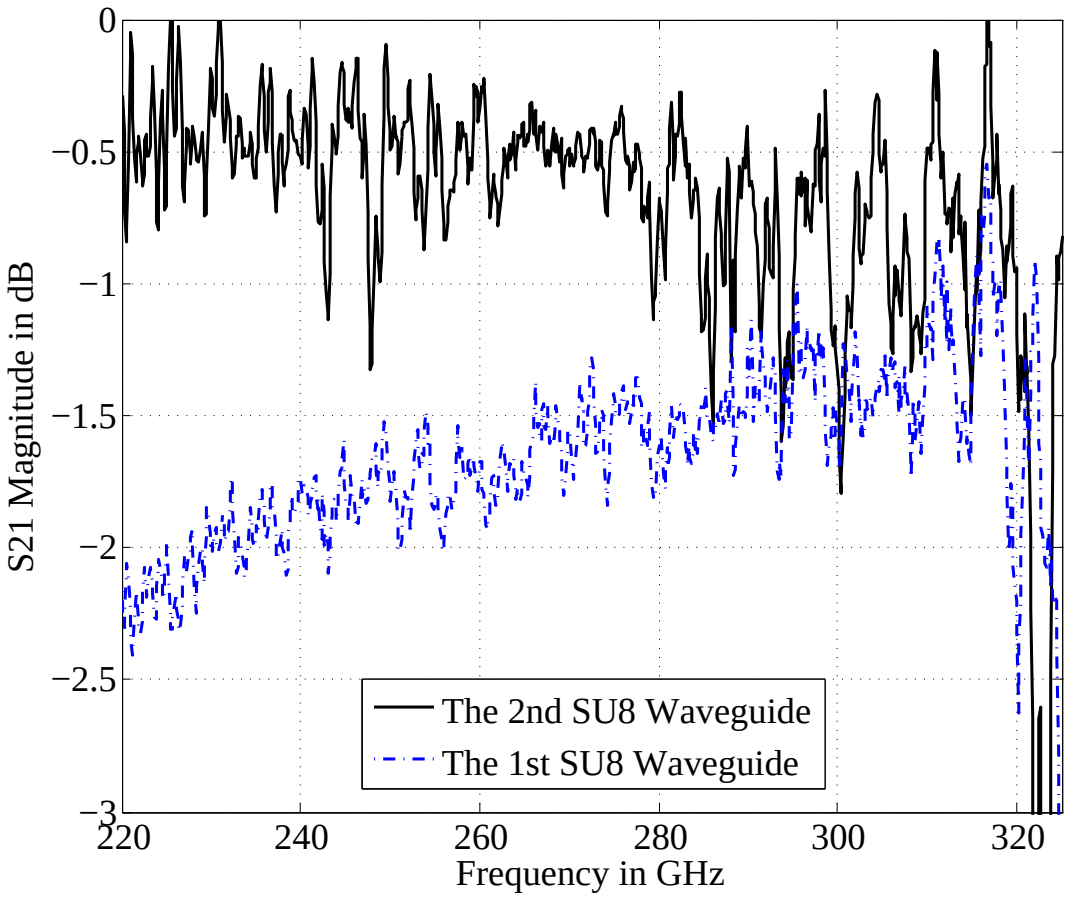

Figure 3.10: Measurement S_{21} results for two fabricated waveguides

Figure 3.10 and Figure 3.11 show the measurement results for the two rectangular waveguide devices. As illustrated in Figure 3.10, one waveguide has the measured insertion loss between 2 dB and 1 dB over the tested frequency bandwidth from 220 GHz to 325 GHz and the other one has the insertion loss between 0.5 dB and 1 dB over the main WR-3 band frequencies.

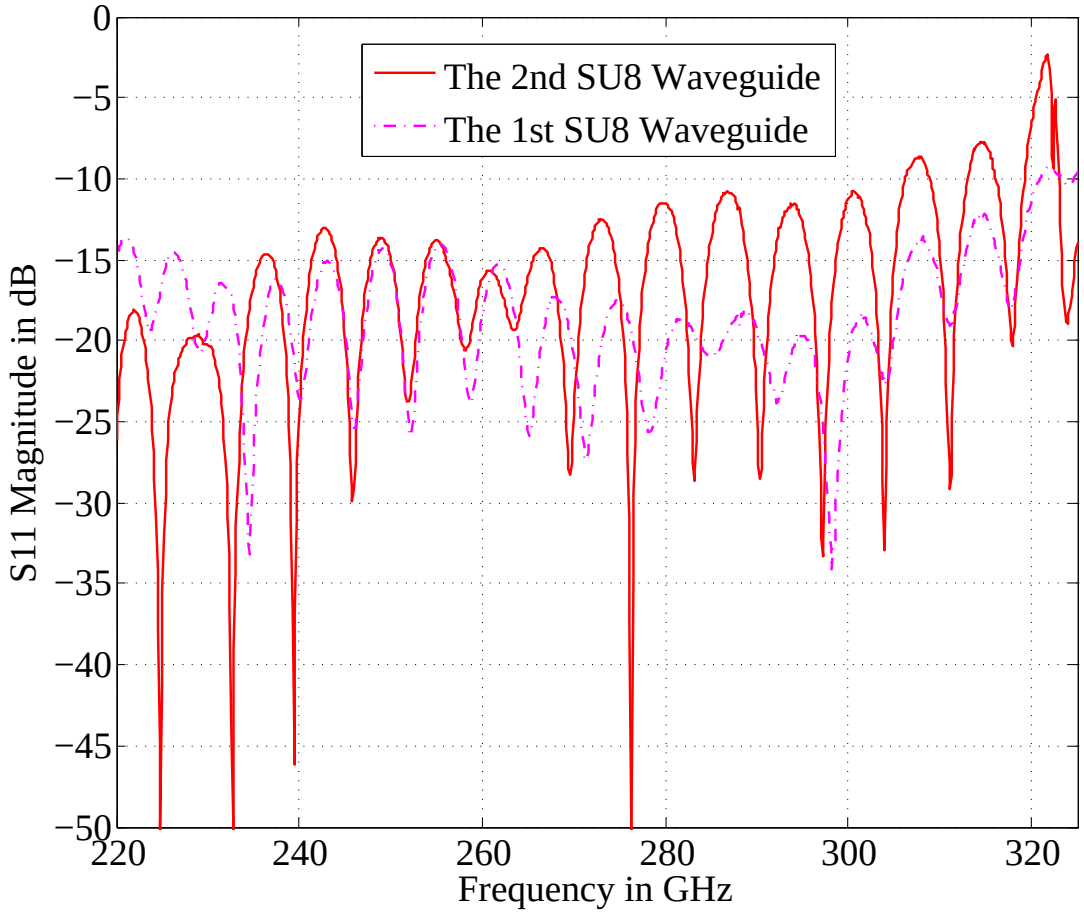

Figure 3.11: Measurement S_{11} results for two fabricated waveguides

In terms of the return loss, in Figure 3.11, one waveguide has between 10 dB to 15 dB return loss over the frequency band and is best at 300 GHz (20 dB return loss) while the other waveguide device is tested with between 5 dB and 15 dB return loss over the whole bandwidth and has the best S_{11} response of -20 dB at 230 GHz. With better control of the fabrication precision on layer thickness, silver coating and fine structure fabrication, the second device has performed better than the first one.

3.8 Discussions

This chapter has demonstrated rectangular waveguide devices for the WR-3 band using SU-8 photoresist micromachining technology. The discussions on measurement results are given in this section. In terms of the SU-8 based waveguide performance, the best measured insertion loss of the device is better than 0.5 dB over the WR-3 band with the best insertion loss is 0.2 dB at low frequency end. The return loss is better than 18 dB at 300 GHz and 15 dB from 220 GHz to 310 GHz. The average insertion loss is 0.03 dB/mm, which is better than the KMPR based NV-LIGA waveguide circuits of 0.096 dB/mm insertion loss [120]. The excellent average insertion loss performance indicates that SU-8 devices can be a good alternative to conventional CNC milling waveguide circuit with insertion loss of 0.021 dB/mm [80] without requiring high fabrication costs, and consistent with previous devices with 4 layers using SU-8 micromaching technology [115].

Possible factors for the device performance are discussed below:

Surface Roughness

When discussing the surface roughness, it is another crucial factor regarding the insertion loss of the waveguide. Due to the scattering of electrons, the silver surface with a rough finish will increase the conductor loss and therefore deteriorate the insertion loss. It has been reported [99] that the nanometre-scale surface roughness of the silver coating onto the SU-8 layer comparing to the several micrometer fabrication tolerance will affect SU-8 waveguide devices performance with 0.017 dB/mm.

Metallisation on Skin depth

Insufficient metallisation on waveguide conducting surfaces can lead to negative impact on the performances due to the skin-depth issue [1]. The formula for skin-depth δ_s is defined as [1],

$$\delta_s = \sqrt{\frac{2}{\omega \mu_r \sigma}} \tag{3.8.1}$$

where ω is the radian frequency, μ_r is the absolute permeability of the conducting material and σ is for the conductivity. The skin depth at 220 GHz for the silver coating on the waveguide pieces is 0.14 μm, and at 325 GHz, it is 0.1 μm according to Equation 3.8.1. The plated silver thickness of the SU-8 pieces is about 2 μm with the control of thickness [99]. This is much larger than the skin-depth. Practically, only a very thin plating of a good conductor, silver or gold, is needed for low-loss waveguide circuits. The skin depth should not be an issue for the disagreement between simulation and measurement results unless there are problems with the deposition of the silver.

Fabrication accuracies

SU-8 Layer of the 1st Device	1	2	3	4	5
Design Model Thickness	288 μm	288 μm	288 μm	288 μm	288 μm
Measured Fabricated Thickness	282 μm	296 μm	286 μm	296 μm	282 μm

Table 3.1: Table of the thickness of modelled SU-8 layers with measured thickness for the fabricated SU-8 device.

The average thickness regardless of the uneven surfaces for each fabricated SU-8 piece is measured by an interferometer and is given with the comparison to the design thickness in Table 3.1. With the comparisons, it can be seen that all the SU-8 pieces are within the 10 μm thickness differences. The impact of the thickness on the device EM performance will be considered later. Figure 3.12 and Figure 3.13 shows scanning electron microscope (SEM) photographs of the internal structures for the fabricated, but unplated, SU-8 pieces.

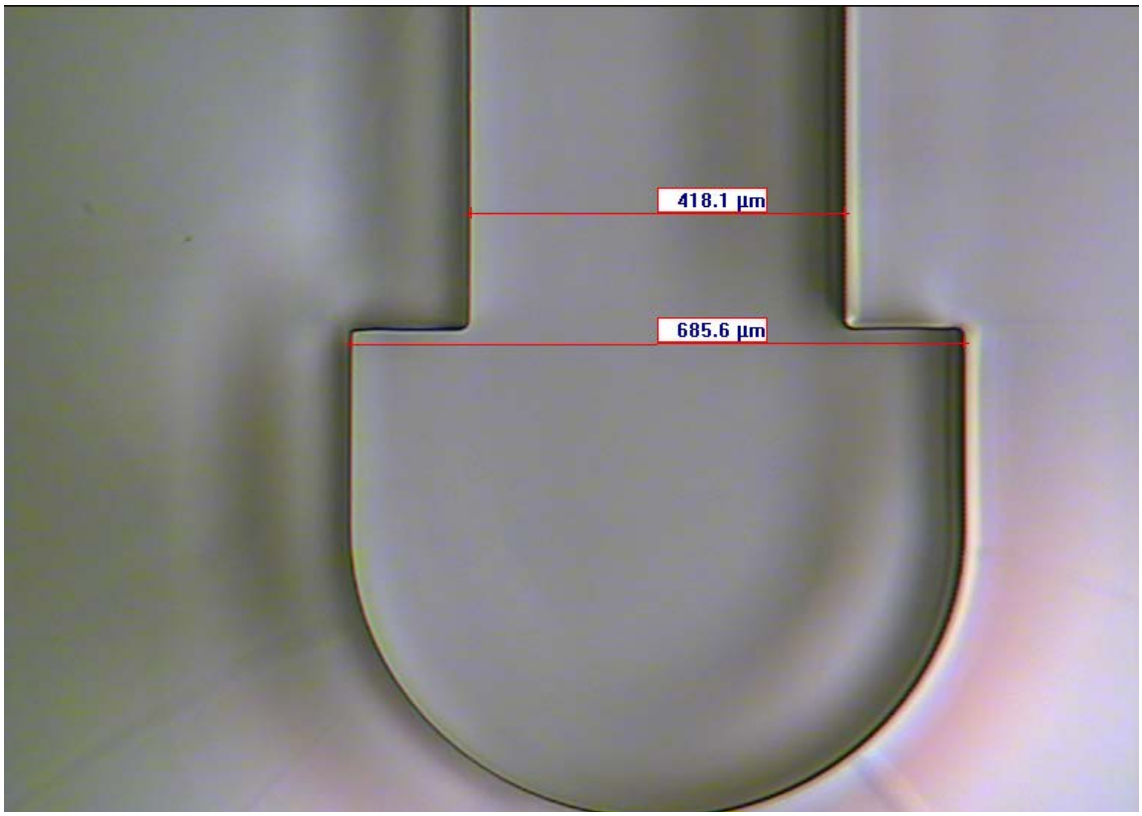

Figure 3.12: Microscope photo of the first SU-8 device for layer 2. The design parameter for the waveguide structure are of widths 699 µm and 432 µm, while the measured dimensions of the structures are of 685.6 µm and 418.1 µm respectively.

The measured geometry of the second fabricated SU-8 waveguide is shown revealing the actual dimensions of the waveguide. The EM model of the waveguide circuits is configured using the measured fabrication dimensions and additional 2 µm silver plating thickness is added on each surface.

A new 3D EM model has been used to simulate the circuit with the dimensions of the fabricated device, and the simulation results for the fabricated SU-8 waveguide device are compared in Figure 3.14. The results indicate the misalignment and fabrication tolerances of SU-8 pieces can determine the measured reflection coefficient S_{11}.

Also it is reported [80] the gaps between each SU-8 pieces can cause energy leakage and negatively affect the insertion loss S_{21}.

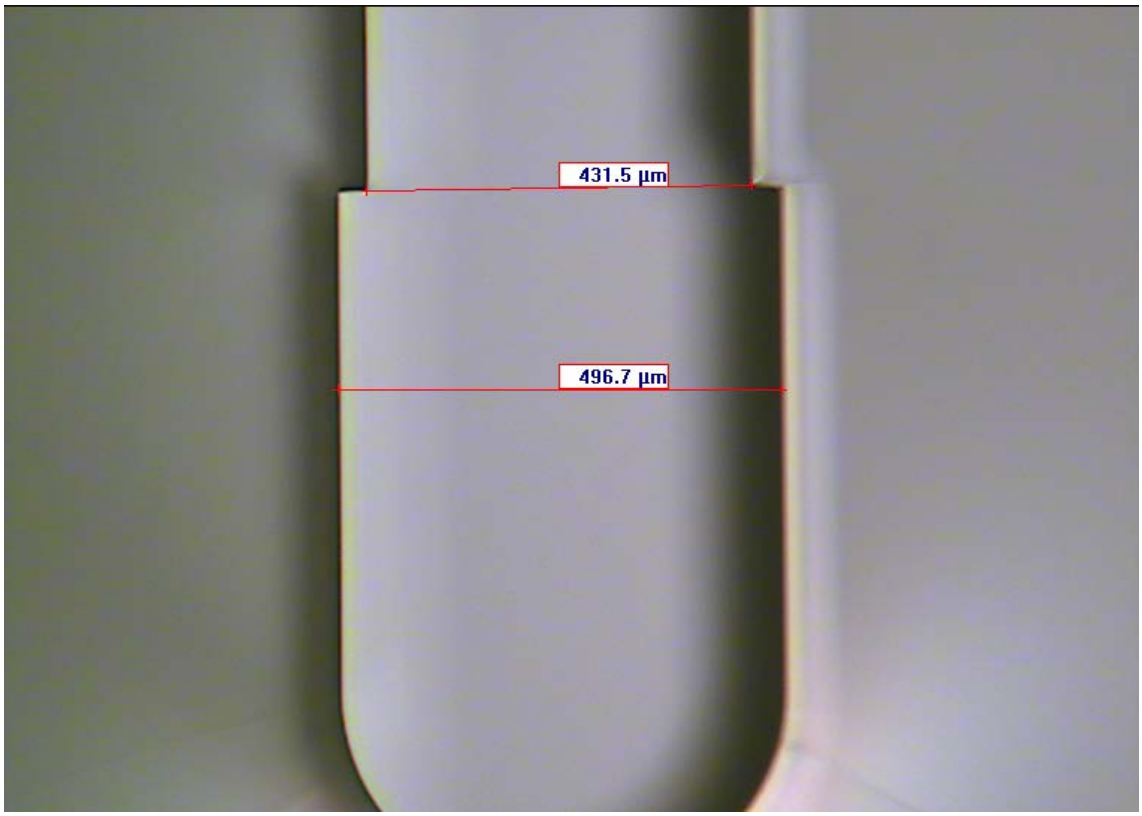

Figure 3.13: Microscope photo of the second SU-8 waveguide device for layer 3. The design parameter for the waveguide structure are of widths 499.1 µm and 432 µm, while the measured dimensions of the structures are of 496.7 µm and 431.5 µm respectively.

In summary, it is believed that the fabrication accuracy is the core factor which affects the measurement results over the factors such as surface roughness and skin depth.

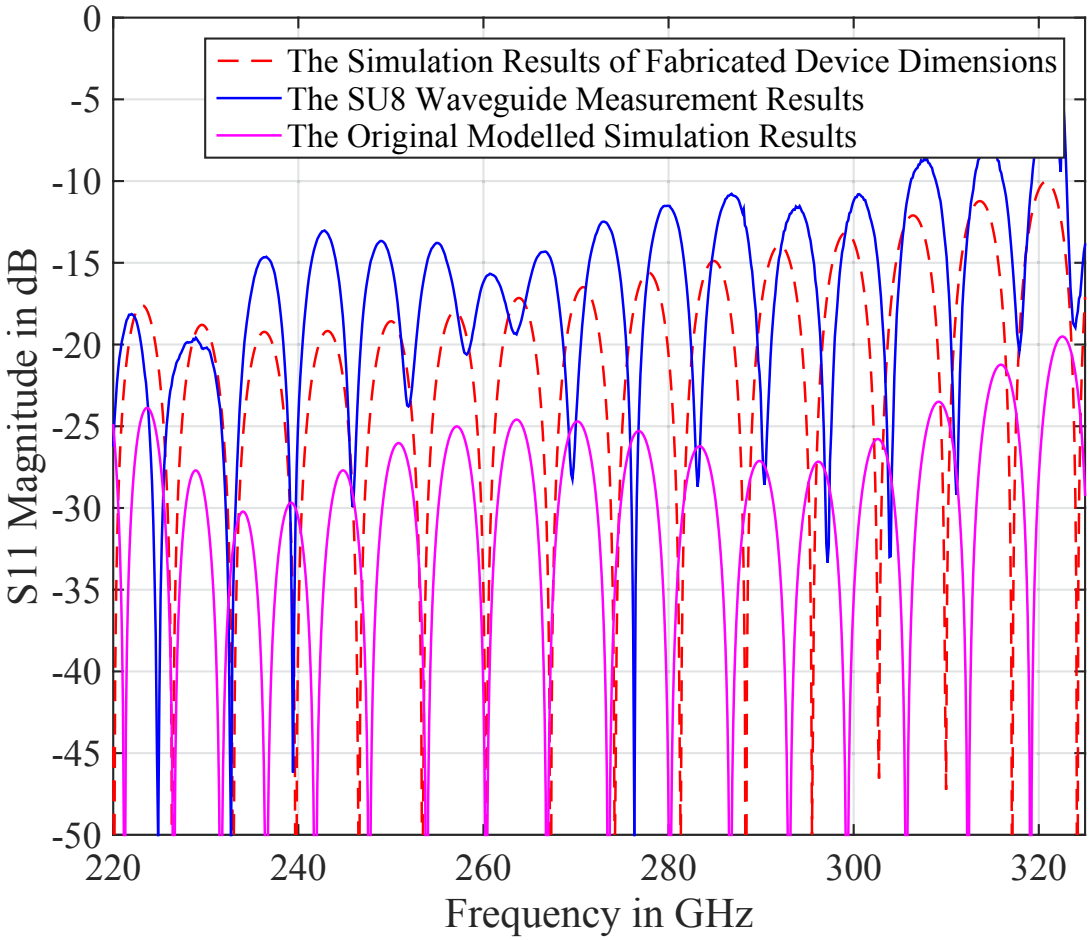

Figure 3.14: Comparisons between simulation results of fabrication dimensions vs. measurement results vs. original EM simulation results.

3.9 Summary

In this chapter, rectangular waveguides made of SU-8 for the WR-3 band (220 GHz - 325 GHz) have been demonstrated and fabricated. This chapter has presented the details of 3D EM design based on SU-8 micromachining techniques for the waveguide design. Waveguide devices have been measured with the novel bends which connect the waveguide to the measurement flanges. Dimensional evaluations comparing the actual device dimensions to the modelling are given. The SU-8 waveguides demonstrate the average insertion loss is comparable to conventional CNC micormachining waveguides at 0.03 dB/mm.

This chapter has led to two publications in [114, 116].

Chapter 4

Coupled Resonator Circuits for Transistor Amplifiers

4.1 Introduction

A general coupling matrix based on coupled resonator circuits has been used to design microwave passive devices for many years [125]. Initially, in this chapter, a general review of coupling matrix synthesis is provided. Some explanations and introductory analysis on conventional coupling matrix synthesis methods for coupled resonator filters are introduced [125]. Later, a simplified transistor small-signal circuit model is presented and it is integrated into the conventional passive coupled resonator circuit model where the transistor is placed after the last resonator and connected to the output terminal. This active coupling matrix with a transistor included is demonstrated. The conventional general matrix $[A]$ is extended with an additional matrix named $[T]$ to describe the transistor characteristics. Another active coupled resonator circuit model is presented where one transistor is placed between two resonators and the transistor behaves as a resonating coupling element for the coupled resonator circuit. Again an additional matrix $[T]$ is introduced to describe transistor characteristics for the extended general matrix $[A]$. Also, the formulas to generate the S-parameters for the two sets of novel transis-

tor coupling matrix are derived for each coupled resonator circuits model with one transistor inserted.

4.2 Coupling Matrix Review

The designs of microwave filters have been reviewed in the literature [126, 127]. The coupling matrix synthesis method is one of the most popular methodologies for the synthesis and design of microwave filters. The coupling matrix concept has been introduced in the 1970's [128–130] for symmetric waveguide filters based on bandpass prototypes, which consist of equivalent lossless lumped-element resonators inter-coupled via lossless transformers [131]. To represent a microwave circuit better, the transformers can be replaced by immittance inverters, so that the electrical characteristics of many coupling devices are approximated [125, 132]. It has been extensively extended and promoted [131]. Several review papers on the coupling matrix synthesis for coupled resonator filters are available in [132–135], and some well accepted books are available on the topic of filter synthesis using coupling matrix [125, 131]. Although the basic filter coupling matrix synthesis assumes frequency independent coupling, lossless resonators, coupling matrix synthesis methods have also been developed for lossy microwave circuits [136–138]. Microwave filters are two-port components for microwave systems and coupling matrix synthesis is applied to design filters. The coupling matrix has also been extended to mupltiport circuits, for instance, power dividers [139], diplexers [139, 140] and multiplexer [123, 141]. Also, the coupling matrix synthesis methods have been used for applications on antennas [142–144] and 90 degree hybrid couplers [145].

4.3 Coupling Matrix Synthesis

The synthesis for microwave filter design with approximation techniques of narrow-band filters is introduced in [146] and extended in [147]. These approximate synthesis techniques can give good results for narrow band filters. The synthesis of the coupling matrix for filters is based on

low-pass prototype filters with frequency and element transformation implemented to achieve the target frequency domain and filter type. The element values of lowpass prototype filter can be found via analytical means or tables in [147, 148], and then they can be transformed into quality factors and coupling coefficients to realise physical filter designs.

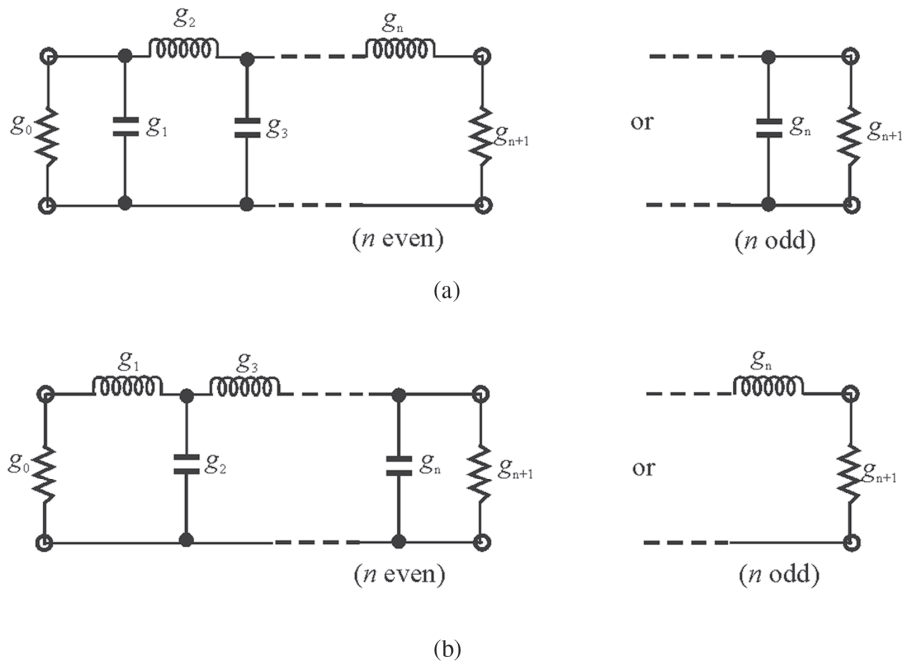

Figure 4.1: Lowpass prototype filters for all-pole filters with (a) a ladder network structure and (b) its dual. Taken from [125]

A brief introduction of an n pole Chebyshev lowpass prototype for an all-pole filter response is given below with the topology in Figure 4.1. A lowpass prototype filter is a filter with its source resistance or conductance equal to one, denoted by $g_0 = 1$, cutoff angular frequency to be unity, denoted by $\Omega_c = 1$ (rad/s). [125, 147] show forms of an n-pole lowpass prototype for an all-pole

filter response and filter synthesis calculation formulas based on g values.

$$
\begin{aligned}
g_0 &= 1 \\
g_1 &= \frac{2}{\gamma}\sin\left(\frac{\pi}{2n}\right) \\
g_i &= \frac{1}{g_{i-1}}\frac{4\sin\left(\frac{(2i-1)\pi}{2n}\right)\cdot\sin\left(\frac{(2i-3)\pi}{2n}\right)}{\gamma^2+\sin^2\left(\frac{(i-1)\pi}{n}\right)} \ (i=2 \text{ to } n) \\
g_{n+1} &= \begin{cases} 1 & \text{for } n \text{ odd} \\ \coth^2\left(\frac{\beta}{4}\right) & \text{for } n \text{ even} \end{cases}
\end{aligned}
\tag{4.3.1}
$$

where

$$
\begin{aligned}
\beta &= \ln\left[\coth\left(\frac{L_{Ar}}{17.37}\right)\right] \\
\gamma &= \sinh\left(\frac{\beta}{2n}\right)
\end{aligned}
$$

The input external quality factor Q_{e1}, and output external quality factor Q_{en} of a filter is

$$
\begin{aligned}
Q_{e1} &= \frac{g_0 g_1}{FBW} \\
Q_{en} &= \frac{g_n g_{n+1}}{FBW}
\end{aligned}
\tag{4.3.2}
$$

where FBW is the fractional bandwidth.

The coupling matrix coefficients $M_{i,i+1}$ ($i = 1$ to $n-1$) between the i and $i+1$ resonators are

$$
M_{i,i+1} = \frac{FBW}{\sqrt{g_i g_{i+1}}} \tag{4.3.3}
$$

For more complex topology and higher selectivity specifications transmission zeroes can be included. Optimization methods are usually used and some optimization approaches and techniques are available in [125, 131, 149–151].

On the topic of using coupling matrix for active microwave circuit synthesis and design, it has

been reported that transistors can be considered with filter designs. Reference [152] demonstrates a bandpass filter using the active capacitance circuit of a transistor, where the active capacitor is made of a transistor exhibiting negative resistance as well as capacitance to compensate the loss of an resonator, and the design is based on conventional microwave passive bandpass filter design using immittance inverter theory. However, the transistor cannot be synthesised into the coupling matrix and it is designed separately to the bandpass filter.

To the author's knowledge, at the moment, there is no coupling matrix and synthesis method reported to describe the active circuits such as amplifiers, mixers and other frequency synthesis devices. In the following section, a novel coupling matrix to describe active circuits with a transistor is presented after a brief introduction of the general coupling matrix.

4.4 The $n \times n$ Coupling Matrix for Coupled Resonator Filters

In this section, a conventional and widely cited [125] filter coupling matrix synthesis method of a coupled resonator circuit model is presented. For a two port coupled resonator filter with

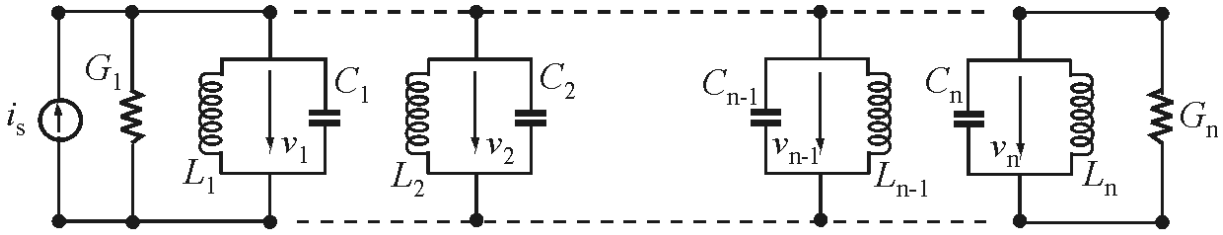

Figure 4.2: Equivalent circuit of n-coupled resonators for node-equation formulation, taken from [125].

electric couplings, the equivalent circuit is shown in Figure 4.2 with node equation formulation. In the circuit model, filters can be described by an equivalent circuit of coupled resonators of n^{th} order with inductance L, capacitance C and resistance R or conductance G to represent the circuit model. In the model, v_i is the node voltage, G denotes the conductance and i_s is the source current. Based on Kirchhoff's current law, the node equations for circuit in Figure 4.2

are

$$\begin{aligned}\left(G_1 + j\omega C_1 + \tfrac{1}{j\omega L_1}\right) v_1 - j\omega C_{12} v_2 \cdots - j\omega C_{1n} v_n &= i_s \\ -j\omega C_{21} v_1 + \left(j\omega C_2 + \tfrac{1}{j\omega L_2}\right) v_2 \cdots - j\omega C_{2n} v_n &= 0 \\ \vdots & \\ -j\omega C_{n1} v_1 + -j\omega C_{n2} v_2 \cdots + \left(j\omega C_n + \tfrac{1}{j\omega L_n} + G_n\right) v_n &= 0\end{aligned} \tag{4.4.1}$$

Here the $C_{ij} = C_{ji}$ means the mutual capacitance across resonators i and j denoted as the dotted lines in the figure, and all node voltages are determined with the ground reference node to introduce a negative sign for the mutual coupling capacitance. $\omega_0 = 1/\sqrt{LC}$ is the filter midband frequency, $FBW = \Delta\omega/\omega_0$ is defined as the fractional bandwidth. In the matrix form, the equations are

$$[Y] \cdot [v] = [i] \tag{4.4.2}$$

where $[Y]$ is an $n \times n$ admittance matrix. On the condition of a synchronously tuned filter, the normalized admittance matrix $[\overline{Y}]$ is given by

$$[Y] = \omega_0 C \cdot FBW \cdot \left[\overline{Y}\right] \tag{4.4.3}$$

The equations $\left[\overline{Y}\right]$ are

$$\left[\overline{Y}\right] = \begin{bmatrix} \frac{G_1}{\omega_0 C \cdot FBW} + p & -j\frac{\omega}{\omega_0}\frac{C_{12}}{C} \cdot \frac{1}{FBW} & \cdots & -j\frac{\omega}{\omega_0}\frac{C_{1n}}{C} \cdot \frac{1}{FBW} \\ -j\frac{\omega}{\omega_0}\frac{C_{21}}{C} \cdot \frac{1}{FBW} & p & \cdots & -j\frac{\omega}{\omega_0}\frac{C_{2n}}{C} \cdot \frac{1}{FBW} \\ \vdots & \vdots & \vdots & \vdots \\ -j\frac{\omega}{\omega_0}\frac{C_{n1}}{C} \cdot \frac{1}{FBW} & -j\frac{\omega}{\omega_0}\frac{C_{n2}}{C} \cdot \frac{1}{FBW} & \cdots & \frac{G_n}{\omega_0 C \cdot FBW} + p \end{bmatrix} \tag{4.4.4}$$

where p is for the complex lowpass frequency variable as

$$p = j(\frac{\omega}{\omega_0} - \frac{\omega_0}{\omega})\frac{1}{FBW} \tag{4.4.5}$$

Practically, circuits based on coupled resonators are determined by the external quality factors

and inter-resonator coupling coefficients.

The external factor Q_{ei} is

$$Q_{ei} = \frac{\omega_0 C}{G_i} \quad \text{for } i = 1, n \tag{4.4.6}$$

and the coupling coefficient M_{ij} is

$$M_{ij} = \frac{C_{ij}}{\sqrt{C_i C_j}} \quad \text{for } i \neq j \tag{4.4.7}$$

The scaled external quality factor q_{ei} is given by

$$q_{ei} = Q_{ei} \cdot FBW \tag{4.4.8}$$

and the normalized coupling coefficient m_{ij} is

$$m_{ij} = \frac{M_{ij}}{FBW} \tag{4.4.9}$$

With the Equations from (4.4.6) to (4.4.9) and the assumption for the narrow-band approximation $\omega/\omega_0 \approx 1$, $[\overline{Y}]$ can be simplified as

$$\left[\overline{Y}\right] = \begin{bmatrix} \frac{1}{q_{e1}} + p & -jm_{12} & \cdots & -jm_{1n} \\ -jm_{21} & p & \cdots & -jm_{2n} \\ \vdots & \vdots & \vdots & \vdots \\ -jm_{n1} & -jm_{n2} & \cdots & \frac{1}{q_{en}} + p \end{bmatrix} \tag{4.4.10}$$

If the coupled resonator circuit is asynchronously tuned which means that the resonators do not share a common resonating frequency, the equations are

$$M_{ij} = \frac{C_{ij}}{\sqrt{C_i C_j}} \quad \text{for } i \neq j \tag{4.4.11}$$

In this case, it gives

$$\left[\overline{Y}\right] = \begin{bmatrix} \frac{1}{q_{e1}} + p - jm_{11} & -jm_{12} & \cdots & -jm_{1n} \\ -jm_{21} & p - jm_{22} & \cdots & -jm_{2n} \\ \vdots & \vdots & \vdots & \vdots \\ -jm_{n1} & -jm_{n2} & \cdots & \frac{1}{q_{en}} + p - jm_{nn} \end{bmatrix} \tag{4.4.12}$$

A general coupling matrix is used to describe circuits which are based on coupled resonators. The coupling matrix design approach can be applied to any electrical or magnetic circuit. A general coupling matrix can be determined from Equation (4.4.12) and is described as,

$$[A] = [q] + p[U] - j[m] \tag{4.4.13}$$

where $[U]$ is the $n \times n$ unit or identity matrix, $[q]$ is an $n \times n$ matrix with all entries zero, except that $q_{11} = 1/q_{e1}$ and $q_{nn} = 1/q_{en}$, which are the external quality factors of the coupled resonators. The matrix $[m]$ is called the general coupling matrix and it is reciprocal, namely that $m_{ij} = m_{ji}$ with possible nonzero diagonal entries m_{ii} for an asynchronously tuned filter.

4.5 The Small Signal Transistor Model

The circuit model of a transistor presented in [1, 153] is a very complex model for a transistor, which means that the coupling matrix synthesis of coupled resonator circuits with a transistor can be very complex. However, a well accepted simple transistor model is shown in Figure 4.3 based on basic transistor amplifier theory [1], here there are no package parasitics included for the small series resistances and inductances at gate, drain, source terminals due to ohmic contacts and bonding leads. A small signal transistor equivalent circuit is possibly represented by some simple circuit elements [154]. In Figure 4.3, the drain conductance g_d and the transconductance g_m are used to predict the transistor performance under a certain bias condition and operating point. C_{gd} represents the capacitance between transistor gate and drain. This simplest

ideal transistor model is used to describe the transistor in the coming sections to represent a transistor in the coupled resonator circuit. The voltage controlled current source $g_m V_{gs}$ gives the

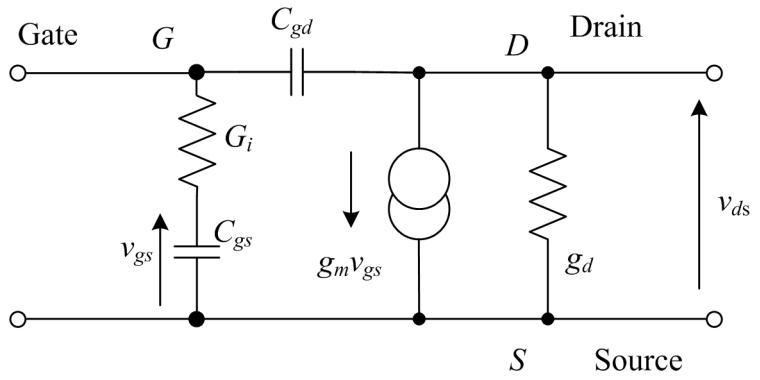

Figure 4.3: Simplest Small signal equivalent circuit for a microwave FET in the common-source configuration, redrawn from [154]

forward transmission path of $S_{21} > 1$ in magnitude with common source connections and g_m is the transconductance. The reverse propagation path for a transistor, S_{12}, is solely dependent to the capacitance between gate and drain C_{gd}. The G_i is the series gate conductance of a transistor, which can be represented as G_t for the equivalent conductance in the following sections. g_d is the drain to source conductance which is usually small. C_{gs} is the capacitance between gate and source [1]. C_{ds}, the capacitance between drain to source, is not included in this figure for circuit simplicity, as it mainly affects the transistor output. However, it is not significant into a further coupled resonator circuit focusing on transistor input circuits. On the condition of the unilateral assumption, the capacitance C_{gd} can be ignored and $S_{12} = 0$. In the bilateral condition, C_{gd} will affect the coupling, which will affect the frequency response if $S_{12} \neq 0$.

4.6 The $(n + 1) \times (n + 1)$ Coupling Matrix for a Transistor integrated into the last Resonator

In this section, a coupling matrix which includes the transistor at the end of the last resonator is presented. It extends the coupled resonator circuit for passive filter networks in [125] to use a

coupling matrix with a transistor. The conventional passive coupled resonator circuit for filters now is extended to describe the behaviours of a transistor into a coupled resonator circuit, which enables the synthesis approach to design a filter with an amplifier using filter synthesis methods. This novel coupled resonator circuit for filtering amplifiers is drawn in Figure 4.4. In the topology, n is the order of the filter and also indicates the number of resonators. The black nodes indicate the resonators and the white nodes indicate the source or load termination. The triangle symbol $\triangleright$ between the n th resonator and load node represents the inserted small-signal transistor model.

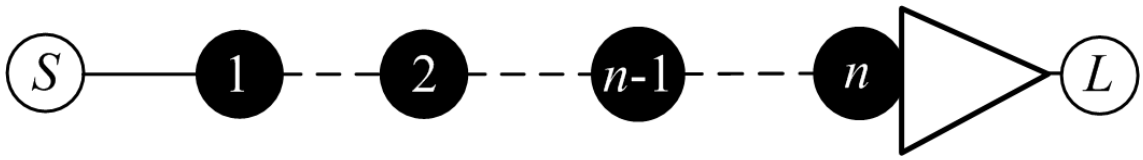

Figure 4.4: Topology of n-coupled resonator circuits with transistor at end terminal.

Figure 4.5 shows the equivalent circuit of n-coupled resonators with a small signal transistor included. The L, C, and R indicate the inductance, capacitance and resistance respectively and a simplified transistor model is included into the network. Each resonator is coupled by electric coupling via mutual capacitance which is denoted as dotted lines [125]. G_S and G_L represent the

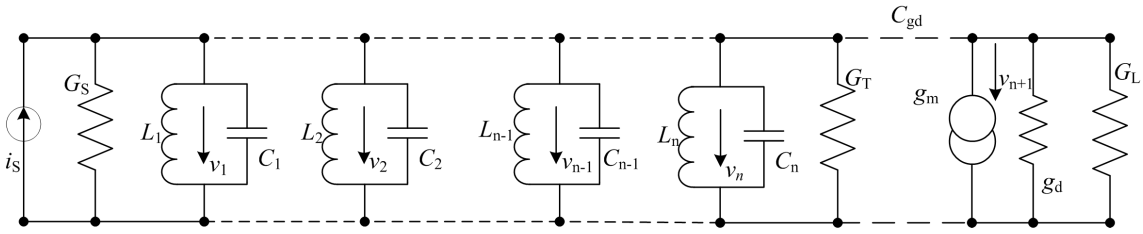

Figure 4.5: Equivalent circuit of n-coupled resonator circuits with simplified transistor model for node-equation formulation.

source and load conductance. The termination conductance G_T is the equivalent conductance for the transistor input circuit, but not the actual physical transistor series gate conductance G_i. G_T is determined by the intrinsic transistor conductance G_i as well as the associated resonator,

which is discussed further in Chapter 5 and Chapter 6. This circuit extends the conventional passive coupled resonator circuit in Figure 4.2 with the simple small-signal transistor model in Figure 4.3. The capacitor between transistor gate to drain C_{gd} is denoted in dashed line between G_T and the transconductance g_m. g_d is the drain conductance or output conductance of the transistor, which can be determined from the drain resistance $r_d = 1/g_d$.

By applying the Kirchhoff's Current Law, the node equations of the circuit are

$$\begin{aligned}
(G_s + j\omega C_1 + \tfrac{1}{j\omega L_1})v_1 - j\omega C_{12}v_2 \cdots - j\omega C_{1n}v_n &= i_s \\
-j\omega C_{21}v_1 + (j\omega C_2 + \tfrac{1}{j\omega L_2})v_2 \cdots - j\omega C_{2n}v_n &= 0 \\
\vdots & \\
-j\omega C_{n1}v_1 - j\omega C_{n2}v_2 \cdots + \left(j\omega C_n + \tfrac{1}{j\omega L_n} + G_T\right)v_n - j\omega C_{gd}v_{n+1} &= 0 \\
g_m v_n - j\omega C_{gd}v_n + g_d v_{n+1} + G_L v_{n+1} &= 0
\end{aligned} \tag{4.6.1}$$

Put the set of equations into matrix from

$$\begin{bmatrix}
G_S + j\omega C_1 + \frac{1}{j\omega L_1} & -j\omega C_{12} & \cdots & -j\omega C_{1n} & 0 \\
-j\omega C_{21} & j\omega C_2 + \frac{1}{j\omega L_2} & \cdots & -j\omega C_{2n} & 0 \\
\vdots & \vdots & \vdots & \vdots & \vdots \\
-j\omega C_{n1} & -j\omega C_{n2} & \cdots & G_T + j\omega C_n + \frac{1}{j\omega L_n} & -j\omega C_{gd} \\
0 & 0 & \cdots & g_m - j\omega C_{gd} & G_L + g_d
\end{bmatrix}
\begin{bmatrix} v_1 \\ v_2 \\ \vdots \\ v_n \\ v_{n+1} \end{bmatrix}
=
\begin{bmatrix} i_s \\ 0 \\ \vdots \\ 0 \\ 0 \end{bmatrix} \tag{4.6.2}$$

Under the synchronously tuned filter conditions, all resonators resonate at the same frequency, the midband frequency of filter $\omega_0 = 1/\sqrt{LC}$, where $L = L_1 = L_2 = \cdots = L_n$ and $C = C_1 = C_2 = \cdots = C_n$ for simplicity.

The admittance matrix can be presented as

$$[Y] = \omega_0 C \cdot FBW \cdot \left[\overline{Y}\right] \tag{4.6.3}$$

where $\omega_0 = 1/\sqrt{LC}$ is the midband frequency and $FBW = \Delta\omega/\omega_0$ is the fractional bandwidth, Then the normalized admittance matrix $[\overline{Y}]$ is given as

$$[\overline{Y}] = \begin{bmatrix} \frac{G_S}{\omega_0 C \cdot FBW} + p & -j\frac{\omega}{\omega_0}\frac{C_{12}}{C} \cdot \frac{1}{FBW} & \cdots & -j\frac{\omega}{\omega_0}\frac{C_{1n}}{C} \cdot \frac{1}{FBW} & 0 \\ -j\frac{\omega}{\omega_0}\frac{C_{21}}{C} \cdot \frac{1}{FBW} & p & \cdots & -j\frac{\omega}{\omega_0}\frac{C_{2n}}{C} \cdot \frac{1}{FBW} & 0 \\ \vdots & \vdots & \vdots & \vdots & \vdots \\ -j\frac{\omega}{\omega_0}\frac{C_{n1}}{C} \cdot \frac{1}{FBW} & -j\frac{\omega}{\omega_0}\frac{C_{n2}}{C} \cdot \frac{1}{FBW} & \cdots & \frac{G_T}{\omega_0 C \cdot FBW} + p & -j\frac{\omega}{\omega_0}\frac{C_{gd}}{C} \cdot \frac{1}{FBW} \\ 0 & 0 & \cdots & \frac{g_m}{\omega_0 C \cdot FBW} - j\frac{\omega}{\omega_0}\frac{C_{gd}}{C} \cdot \frac{1}{FBW} & \frac{G_L}{\omega_0 C \cdot FBW} + \frac{g_d}{\omega_0 C \cdot FBW} \end{bmatrix} \tag{4.6.4}$$

The external quality factor for Q_{eT} is defined as

$$Q_{eT} = \frac{\omega_0 C}{G_T} \tag{4.6.5}$$

which can be applied to Q_{eS} and Q_{eL}. The definition for the coupling coefficient M_{ij} is

$$M_{ij} = \frac{C_{ij}}{C} \tag{4.6.6}$$

where i and j represent the i^{th} row and j^{th} column.

The coupling coefficient M_{gd} for capacitance across gate to drain is defined as

$$M_{gd} = \frac{C_{gd}}{C} \tag{4.6.7}$$

The scaled external quality factor is given as,

$$q_{eT} = Q_{eT} \cdot FBW \tag{4.6.8}$$

The normalized coupling coefficient m_{ij} is

$$m_{ij} = \frac{M_{ij}}{FBW} \tag{4.6.9}$$

The coupling coefficient M_{gd} can be also normalized by the fractional bandwidth FBW as,

$$m_{gd} = \frac{M_{gd}}{FBW} \tag{4.6.10}$$

With the narrow band approximation $\omega/\omega_0 \approx 1$, Equation (4.6.4) can be simplified as

$$[\overline{Y}] = \begin{bmatrix} \frac{1}{q_{eS}} + p & -jm_{12} & \cdots & -jm_{1n} & 0 \\ -jm_{21} & p & \cdots & -jm_{2n} & 0 \\ \vdots & \vdots & \vdots & \vdots & \vdots \\ -jm_{n1} & -jm_{n2} & \cdots & \frac{1}{q_{eT}} + p & -jm_{gd} \\ 0 & 0 & \cdots & T_{gm} - jm_{gd} & \frac{1}{q_{eL}} + T_{gd} \end{bmatrix} \tag{4.6.11}$$

For this coupled resonator circuit, when it is asynchronously tuned, the Equations (4.6.6) and (4.6.11) become

$$M_{ij} = \frac{C_{ij}}{\sqrt{C_i C_j}} \quad \text{for } i \neq j \tag{4.6.12}$$

$$[\overline{Y}] = \begin{bmatrix} \frac{1}{q_{eS}} + p - jm_{11} & -jm_{21} & \cdots & -jm_{1n} & 0 \\ -jm_{21} & p - jm_{22} & \cdots & -jm_{2n} & 0 \\ \vdots & \vdots & \vdots & \vdots & \vdots \\ -jm_{n1} & -jm_{n2} & \cdots & \frac{1}{q_{eT}} + p - jm_{nn} & -jm_{g_d} \\ 0 & 0 & \cdots & T_{gm} - jm_{gd} & \frac{1}{q_{eL}} + T_{gd} \end{bmatrix} \tag{4.6.13}$$

The general circuit matrix $[A]$ is summarised from Equation (4.6.13) as

$$[A] = [q] + p[U] - j[m] + [T] \tag{4.6.14}$$

where $[U]$ is the $(n+1)\times(n+1)$ unit or identity matrix but the element value for $n+1$ row and $n+1$ column $[U]_{n+1,n+1}=0$, and the $[U]$ matrix is displayed as

$$[U]=\begin{bmatrix} 1 & 0 & \cdots & 0 & 0 \\ 0 & 1 & \cdots & 0 & 0 \\ \vdots & \vdots & \vdots & \vdots & \vdots \\ 0 & 0 & \cdots & 1 & 0 \\ 0 & 0 & \cdots & 0 & 0 \end{bmatrix} \tag{4.6.15}$$

$[q]$ is an $(n+1)\times(n+1)$ matrix for scaled external quality factors with all entries zero, but $q_{11}=1/q_{eS}$, $q_{nn}=1/q_{eT}$ and $q_{n+1,n+1}=1/q_{eL}$ are given by

$$[q]=\begin{bmatrix} \frac{1}{q_{eS}} & 0 & \cdots & 0 & 0 \\ 0 & 0 & \cdots & 0 & 0 \\ \vdots & \vdots & \vdots & \vdots & \vdots \\ 0 & 0 & \cdots & \frac{1}{q_{eT}} & 0 \\ 0 & 0 & \cdots & 0 & \frac{1}{q_{eL}} \end{bmatrix} \tag{4.6.16}$$

$[m]$ is the generalized coupling matrix and it has the representation as

$$[m]=\begin{bmatrix} m_{11} & m_{12} & \cdots & m_{1n} & 0 \\ m_{21} & m_{22} & \cdots & m_{2n} & 0 \\ \vdots & \vdots & \vdots & \vdots & \vdots \\ m_{n1} & m_{n2} & \cdots & m_{nn} & 0 \\ 0 & 0 & \cdots & 0 & 0 \end{bmatrix} \tag{4.6.17}$$

In addition, the $[T]$ is the novel transistor matrix which is formed by the basic elements of a

transistor in Section 4.5. In this case, the $[T]$ matrix has the representations as

$$[T] = \begin{bmatrix} 0 & 0 & \cdots & 0 & 0 \\ 0 & 0 & \cdots & 0 & 0 \\ \vdots & \vdots & \vdots & \vdots & \vdots \\ 0 & 0 & \cdots & 0 & -jm_{g_d} \\ 0 & 0 & \cdots & T_{gm} - jm_{gd} & T_{gd} \end{bmatrix} \tag{4.6.18}$$

where the elements in $[T]$ matrix are defined as $T_{gm} = \frac{g_m}{\omega_0 C \cdot FBW}$ and $T_{gd} = \frac{g_d}{\omega_0 C \cdot FBW}$.
However, the matrix elements m_{gd} can be categorised into the coupling matrix $[m]$ as a coupling factor which results in another representation for coupling matrix $[m]$ as

$$[m] = \begin{bmatrix} m_{11} & m_{12} & \cdots & m_{1n} & 0 \\ m_{21} & m_{22} & \cdots & m_{2n} & 0 \\ \vdots & \vdots & \vdots & \vdots & \vdots \\ m_{n1} & m_{n2} & \cdots & m_{nn} & m_{gd} \\ 0 & 0 & \cdots & m_{gd} & 0 \end{bmatrix} \tag{4.6.19}$$

Here, m_{gd} is placed as a coupling coefficient in the coupling matrix $[m]$ which indicates that m_{gd} can be used as an inter-resonator coupling. The transistor matrix $[T]$ will become

$$[T] = \begin{bmatrix} 0 & 0 & \cdots & 0 & 0 \\ 0 & 0 & \cdots & 0 & 0 \\ \vdots & \vdots & \vdots & \vdots & \vdots \\ 0 & 0 & \cdots & 0 & 0 \\ 0 & 0 & \cdots & T_{gm} & T_{gd} \end{bmatrix} \tag{4.6.20}$$

The complex lowpass frequency variable p appears in the identity matrix but not in the $[A]_{n+1,n+1}$ indicating there are only n resonators, which means that the transistor output is a non-resonating

node in this topology.

4.7 The $n \times n$ Coupling Matrix for a Transistor between Resonators

The coupling matrix for the coupled resonator circuit which includes a transistor between rather than at the end of the coupled resonators is given in this section. In this model, a transistor is included into the circuit as a part of resonating node in the circuit. The coupled resonator circuit with a transistor included into the circuit has the topology as shown in Figure 4.6. In this case it is between the i^{th} and j^{th} resonators as a demonstration of circuit synthesis.

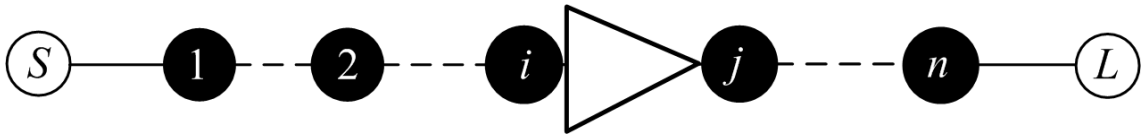

Figure 4.6: Topology of n-coupled resonator circuits with transistor between resonators.

The equivalent circuit of the n-coupled resonator circuit with a transistor is shown in Figure 4.7.

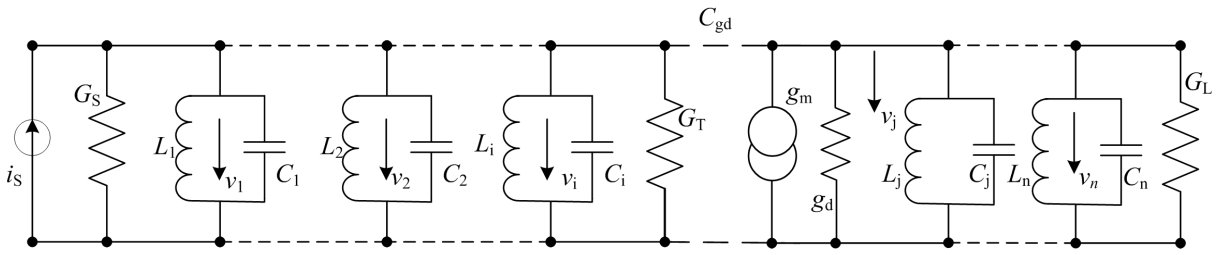

Figure 4.7: Equivalent circuit of n-coupled resonator circuits with simplified transistor model for node-equation formulation.

The L indicates the inductance and C indicates the capacitance. The G_S and G_L are the source and load conductances and i_s is the source current.

By the node analysis of the Kirchhoff's Current Law, the node equations for the circuit are

$$
\begin{aligned}
(G_S + j\omega C_1 + \tfrac{1}{j\omega L_1})v_1 - j\omega C_{12}v_2 \cdots - j\omega C_{1i}v_i - j\omega C_{1j}v_j \cdots - j\omega C_{1n}v_n &= i_s \\
-j\omega C_{21}v_1 + (j\omega C_2 + \tfrac{1}{j\omega L_2})v_2 \cdots - j\omega C_{2i}v_i - j\omega C_{2j}v_j \cdots - j\omega C_{2n}v_n &= 0 \\
&\vdots \\
-j\omega C_{i1}v_1 - j\omega C_{i2}v_2 + \cdots + (j\omega C_i + \tfrac{1}{j\omega L_i} + G_T)v_i - j\omega C_{ij}v_j \cdots - j\omega C_{in}v_n &= 0 \\
-j\omega C_{j1}v_1 - j\omega C_{j2}v_2 + \cdots + (g_m - j\omega C_{ji})v_i + (j\omega C_j + \tfrac{1}{j\omega L_j} + g_d)v_j \cdots - j\omega C_{jn}v_n &= 0 \\
&\vdots \\
-j\omega C_{n1}v_1 - j\omega C_{n2}v_2 \cdots - j\omega C_{ni}v_i - j\omega C_{nj}v_j + (G_L + j\omega C_n + \tfrac{1}{j\omega L_n})v_n &= 0
\end{aligned}
\tag{4.7.1}
$$

The equations can be put into matrix form in $[Y] \cdot [v] = [i]$, and the admittance matrix $[Y]$ is then given as

$$
[Y] = \begin{bmatrix}
G_S + j\omega C_1 + \frac{1}{j\omega L_1} & -j\omega C_{12} & \cdots & -j\omega C_{1i} & -j\omega C_{1j} & \cdots & -j\omega C_{1n} \\
-j\omega C_{21} & j\omega C_2 + \frac{1}{j\omega L_2} & \cdots & -j\omega C_{2i} & -j\omega C_{2j} & \cdots & -j\omega C_{2n} \\
\vdots & \vdots & \vdots & \vdots & \vdots & \vdots & \vdots \\
-j\omega C_{i1} & -j\omega C_{i2} & \cdots & j\omega C_i + \frac{1}{j\omega L_i} + G_T & -j\omega C_{ij} & \cdots & -j\omega C_{in} \\
-j\omega C_{j1} & -j\omega C_{j2} & \cdots & -j\omega C_{ji} + g_m & j\omega C_j + \frac{1}{j\omega L_j} + g_d & \cdots & -j\omega C_{jn} \\
\vdots & \vdots & \vdots & \vdots & \vdots & \vdots & \vdots \\
-j\omega C_{n1} & -j\omega C_{n2} & \cdots & -j\omega C_{ni} & -j\omega C_{nj} & \cdots & G_L + j\omega C_n + \frac{1}{j\omega L_n}
\end{bmatrix}
\tag{4.7.2}
$$

The admittance matrix is expressed by

$$
[Y] = \omega_0 C \cdot FBW \cdot \left[\overline{Y}\right] \tag{4.7.3}
$$

where $\omega_0 = 1/\sqrt{LC}$ is the midband frequency and $FBW = \Delta\omega/\omega_0$ is the fractional bandwidth,

and $[\overline{Y}]$ is the normalized admittance matrix.

Simplifying, the admittance matrix $[\overline{Y}]$ for the synchronously tuned filter gives,

$$[\overline{Y}] = \begin{bmatrix} \frac{G_S}{\omega_0 C \cdot FBW} + p & -j\frac{\omega}{\omega_0}\frac{C_{12}}{C}\cdot\frac{1}{FBW} & \cdots & -j\frac{\omega}{\omega_0}\frac{C_{1i}}{C}\cdot\frac{1}{FBW} & -j\frac{\omega}{\omega_0}\frac{C_{1j}}{C}\cdot\frac{1}{FBW} & \cdots & -j\frac{\omega}{\omega_0}\frac{C_{1n}}{C}\cdot\frac{1}{FBW} \\ -j\frac{\omega}{\omega_0}\frac{C_{21}}{C}\cdot\frac{1}{FBW} & p & \cdots & -j\frac{\omega}{\omega_0}\frac{C_{2i}}{C}\cdot\frac{1}{FBW} & -j\frac{\omega}{\omega_0}\frac{C_{2j}}{C}\cdot\frac{1}{FBW} & \cdots & -j\frac{\omega}{\omega_0}\frac{C_{2n}}{C}\cdot\frac{1}{FBW} \\ \vdots & \vdots & \vdots & \vdots & \vdots & \vdots & \vdots \\ -j\frac{\omega}{\omega_0}\frac{C_{i1}}{C}\cdot\frac{1}{FBW} & -j\frac{\omega}{\omega_0}\frac{C_{i2}}{C}\cdot\frac{1}{FBW} & \cdots & \frac{G_T}{\omega_0 C \cdot FBW} + p & -j\frac{\omega}{\omega_0}\frac{C_{ij}}{C}\cdot\frac{1}{FBW} & \cdots & -j\frac{\omega}{\omega_0}\frac{C_{in}}{C}\cdot\frac{1}{FBW} \\ -j\frac{\omega}{\omega_0}\frac{C_{j1}}{C}\cdot\frac{1}{FBW} & -j\frac{\omega}{\omega_0}\frac{C_{j2}}{C}\cdot\frac{1}{FBW} & \cdots & -j\frac{\omega}{\omega_0}\frac{C_{ji}}{C}\cdot\frac{1}{FBW} + \frac{g_m}{\omega_0 C \cdot FBW} & p + \frac{g_d}{\omega_0 C \cdot FBW} & \cdots & -j\frac{\omega}{\omega_0}\frac{C_{jn}}{C}\cdot\frac{1}{FBW} \\ \vdots & \vdots & \vdots & \vdots & \vdots & \vdots & \vdots \\ -j\frac{\omega}{\omega_0}\frac{C_{n1}}{C}\cdot\frac{1}{FBW} & -j\frac{\omega}{\omega_0}\frac{C_{n2}}{C}\cdot\frac{1}{FBW} & \cdots & -j\frac{\omega}{\omega_0}\frac{C_{ni}}{C}\cdot\frac{1}{FBW} & -j\frac{\omega}{\omega_0}\frac{C_{nj}}{C}\cdot\frac{1}{FBW} & \cdots & \frac{G_L}{\omega_0 C \cdot FBW} + p \end{bmatrix} \tag{4.7.4}$$

With the definition of coupling coefficient in Equation (4.6.6) and external quality factor given in Equation (4.6.5) and also assuming $\omega/\omega_0 \approx 1$ for the narrow-band approximation, a simpler expression of Equation (4.7.4) is obtained:

$$[A] = \begin{bmatrix} \frac{1}{q_{eS}} + p & -jm_{12} & \cdots & -jm_{1i} & -jm_{1j} & \cdots & -jm_{1n} \\ -jm_{21} & p & \cdots & -jm_{2i} & -jm_{2j} & \cdots & -jm_{2n} \\ \vdots & \vdots & \vdots & \vdots & \vdots & \vdots & \vdots \\ -jm_{i1} & -jm_{i2} & \cdots & \frac{1}{q_{eT}} + p & -jm_{ij} & \cdots & -jm_{in} \\ -jm_{j1} & -jm_{j2} & \cdots & -jm_{ji} + T_{gm} & p + T_{gd} & \cdots & -jm_{jn} \\ \vdots & \vdots & \vdots & \vdots & \vdots & \vdots & \vdots \\ -jm_{n1} & -jm_{n2} & \cdots & -jm_{ni} & -jm_{nj} & \cdots & \frac{1}{q_{eL}} + p \end{bmatrix} \tag{4.7.5}$$

where the elements in the matrix are defined as $T_{gm} = \frac{g_m}{\omega_0 C \cdot FBW}$ and $T_{gd} = \frac{g_d}{\omega_0 C \cdot FBW}$.

Similarly, for an asynchronously tuned circuit, with Equation (4.6.12), the coupling matrix

Equation (4.7.5) becomes

$$[A] = \begin{bmatrix} \frac{1}{q_{eS}} + p - jm_{11} & -jm_{12} & \cdots & -jm_{1i} & -jm_{1j} & \cdots & -jm_{1n} \\ -jm_{21} & p - jm_{22} & \cdots & -jm_{2i} & -jm_{2j} & \cdots & -jm_{2n} \\ \vdots & \vdots & \vdots & \vdots & \vdots & \vdots & \vdots \\ -jm_{i1} & -jm_{i2} & \cdots & \frac{1}{q_{eT}} + p - jm_{ii} & -jm_{ij} & \cdots & -jm_{in} \\ -jm_{j1} & -jm_{j2} & \cdots & T_{gm} - jm_{ji} & p + T_{gd} - jm_{jj} & \cdots & -jm_{jn} \\ \vdots & \vdots & \vdots & \vdots & \vdots & \vdots & \vdots \\ -jm_{n1} & -jm_{n2} & \cdots & -jm_{ni} & -jm_{nj} & \cdots & \frac{1}{q_{eL}} + p - jm_{nn} \end{bmatrix} \tag{4.7.6}$$

The coupling matrix $[A]$ can be expressed by the normalized admittance matrix $[\overline{Y}]$ in Equation (4.7.6). The matrix $[A]$ can be expressed as

$$[A] = [q] + p[U] - j[m] + [T] \tag{4.7.7}$$

where the $[q]$ is an $n \times n$ matrix with all entries zero, except that $q_{11} = 1/q_{eS}$, $q_{ii} = 1/q_{eT}$ and $q_{nn} = 1/q_{eL}$.

The $[q]$ matrix is shown as

$$[q] = \begin{bmatrix} \frac{1}{q_{eS}} & 0 & \cdots & 0 & 0 & \cdots & 0 \\ 0 & 0 & \cdots & 0 & 0 & \cdots & 0 \\ \vdots & \vdots & \vdots & \vdots & \vdots & \vdots & \vdots \\ 0 & 0 & \cdots & \frac{1}{q_{eT}} & 0 & \cdots & 0 \\ 0 & 0 & \cdots & 0 & 0 & \cdots & 0 \\ \vdots & \vdots & \vdots & \vdots & \vdots & \vdots & \vdots \\ 0 & 0 & \cdots & 0 & 0 & \cdots & \frac{1}{q_{eL}} \end{bmatrix} \tag{4.7.8}$$

The $[U]$ is the $n \times n$ unit or identity matrix, and $[m]$ is the coupling matrix. Additionally, $[T]$ is

the novel transistor matrix which describes a transistor, which is shown as

$$[T] = \begin{bmatrix} 0 & 0 & \cdots & 0 & 0 & \cdots & 0 \\ 0 & 0 & \cdots & 0 & 0 & \cdots & 0 \\ \vdots & \vdots & \vdots & \vdots & \vdots & \vdots & \vdots \\ 0 & 0 & \cdots & 0 & 0 & \cdots & 0 \\ 0 & 0 & \cdots & T_{gm} & T_{gd} & \cdots & 0 \\ \vdots & \vdots & \vdots & \vdots & \vdots & \vdots & \vdots \\ 0 & 0 & \cdots & 0 & 0 & \cdots & 0 \end{bmatrix} \tag{4.7.9}$$

In this circuit, one element of the coupling matrix $[m]$ is fixed by the transistor. In this topology given in Figure 4.7, $m_{ij} = m_{ji} = m_{gd}$. Physically, the coupling coefficient m_{gd} is determined by the internal transistor capacitance between gate to drain C_{gd} under common source configuration.

The $[m]$ matrix is displayed as

$$[m] = \begin{bmatrix} m_{11} & m_{12} & \cdots & m_{1i} & m_{1j} & \cdots & m_{1n} \\ m_{21} & m_{22} & \cdots & m_{2i} & m_{2j} & \cdots & m_{2n} \\ \vdots & \vdots & \vdots & \vdots & \vdots & \vdots & \vdots \\ m_{i1} & m_{i2} & \cdots & m_{ii} & m_{gd} & \cdots & m_{in} \\ m_{j1} & m_{j2} & \cdots & m_{gd} & m_{jj} & \cdots & m_{jn} \\ \vdots & \vdots & \vdots & \vdots & \vdots & \vdots & \vdots \\ m_{n1} & m_{n2} & \cdots & m_{ni} & m_{nj} & \cdots & m_{nn} \end{bmatrix} \tag{4.7.10}$$

The coupling matrix $[m]$ is derived where the transistor is placed between i^{th} and j^{th} resonator, which means that a transistor can be placed between any adjacent resonators for direct coupling design.

4.8 Two port network for S-parameters generation for the transistor coupled resonator circuit

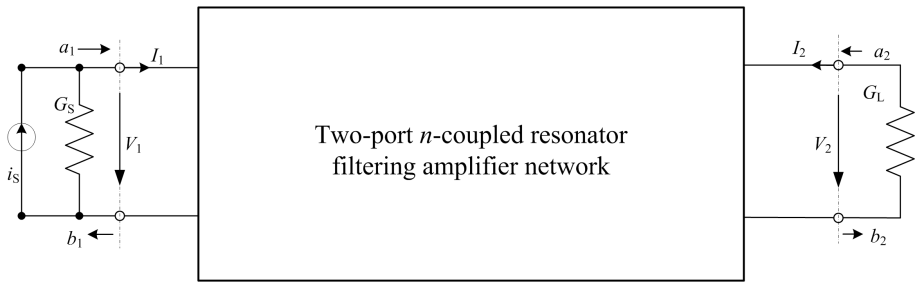

Figure 4.8: Two port network representation of n-coupled resonator circuits.

To derive the S-parameters for the coupled resonator circuit in Figure 4.5 and Figure 4.7 including a transistor and the conventional passive coupled resonator circuit in Figure 4.2, the circuit is represented by a two-port network in Figure 4.8. In the network, the transistor is enclosed in the network and this circuit network is valid for the topology of multiple transistors as well. In the case, $V_1 = v_1$, $V_2 = v_n$, and $I_1 = i_s - v_1 G_1$.

The variables a_1, a_2 and b_1, b_2 are defined as,

$$\begin{aligned} a_1 &= \frac{i_s}{2\sqrt{G_S}}, \quad b_1 = \frac{2v_1 G_S - i_s}{2\sqrt{G_S}} \\ a_2 &= 0, \quad b_2 = v_n \sqrt{G_L} \end{aligned} \tag{4.8.1}$$

$$\begin{aligned} S_{21} &= \left.\frac{b_2}{a_1}\right|_{a_2=0} = \frac{2\sqrt{G_S G_L} v_n}{i_s} \\ S_{11} &= \left.\frac{b_1}{a_1}\right|_{a_2=0} = \frac{2v_1 G_S}{i_s} - 1 \end{aligned} \tag{4.8.2}$$

The unknown node voltages v_1 and v_n are,

$$\begin{aligned} v_1 &= \frac{i_s}{\omega_0 C \cdot FBW} \left[\overline{Y}\right]^{-1}_{11} \\ v_n &= \frac{i_s}{\omega_0 C \cdot FBW} \left[\overline{Y}\right]^{-1}_{n1} \end{aligned} \tag{4.8.3}$$

where $\left[\overline{Y}\right]^{-1}_{ij}$ is the i th row and j th column element for $\left[\overline{Y}\right]^{-1}$ in Equation (4.6.13).

$$\begin{aligned} S_{21} &= \frac{2\sqrt{G_S G_L}}{\omega_0 C \cdot FBW} \left[\overline{Y}\right]^{-1}_{n1} \\ S_{11} &= \frac{2G_S}{\omega_0 C \cdot FBW} \left[\overline{Y}\right]^{-1}_{11} - 1 \end{aligned} \tag{4.8.4}$$

which can be simplified as

$$\begin{aligned} S_{21} &= 2\frac{1}{\sqrt{q_{eS} q_{eL}}} \left[\overline{Y}\right]^{-1}_{n,1} \\ S_{11} &= \frac{2}{q_{eS}} \left[\overline{Y}\right]^{-1}_{11} - 1 \end{aligned} \tag{4.8.5}$$

For the normalized admittance matrix $[\overline{Y}]$, it can be denoted as a general matrix $[A]$ for the n-coupled resonator circuits. Accordingly, Equations (4.8.5) can be converted into general forms as

$$\begin{aligned} S_{21} &= 2\frac{1}{\sqrt{q_{eS} q_{eL}}} [A]^{-1}_{n,1} \\ S_{11} &= \frac{2}{q_{eS}} [A]^{-1}_{11} - 1 \end{aligned} \tag{4.8.6}$$

4.9 Summary

In summary, a review of the coupling matrix and its synthesis has been given and the conventional coupling matrix is introduced based on passive coupled resonator circuits for filters. Later, an ideal transistor small signal circuit model consisting of the combination of lumped elements and a ideal model with a voltage controlled current source is presented to describe the fundamental amplification performance of a transistor. Two sets of general coupling matrices based on previous passive circuit synthesis has been developed with abilities to describe the integration of transistors into the coupled resonator matrix.

Here, this active coupling matrix is based on the two-port network with a simple transistor integrated into the network. They can be easily extended to accommodate multiple couplings with source or load [125]. Multiple transistors connected in series, forming multi-stage amplifier circuit can be described by extending the active coupling matrix discussed in this section. If multiple transistor are connected in parallel forming a balanced amplifier, a multi-port active coupling matrix can be generated based on the conventional coupling matrix for mutliport circuits such as power divider [139, 140].

Chapter 5 and Chapter 6 will give examples using the active coupling matrix including a transistor to design a microstrip filtering amplifier and a waveguide filtering amplifier, respectively.

Chapter 5

Microstrip Bandpass Filtering Amplifier

5.1 Introduction

Conventional matching for microstrip amplifiers uses impedance matching circuits with distributed transmission lines to achieve a conjugate match for maximum gain or optimal impedance match for optimal noise performance. When a filter is connected to an amplifier in most communication systems, the conventional way of integration is to design the filter and amplifiers separately for a common terminal impedance [155, 156]. Each circuit component is designed and matched to a standard input and output impedance, and 50 Ω is now widely adapted as the standard. However, the matching circuits and the connecting transmission lines can give additional losses as well as the cost of larger circuit sizes. The demand has increased for compact circuits with less transmission line loss. The concept of circuits and systems integration for amplifier design with filters is to eliminate the matching circuits and interconnection between amplifiers and other circuits. A novel amplifier design method is presented here based on the coupled resonator filter design technique using the coupling matrix formulation in Chapter 4. An example of a microstrip bandpass amplifier is given in this chapter using the novel matrix synthesis design technique.

5.2 Review of Bandpass Filtering Amplifier

Chapter 2 has given the literature review on THz electronics, and this section gives the literature review on bandpass filtering amplifiers for the circuits which combine filter and amplifier designs together. A number of X band amplifiers have been published using different fabrication processes and design technologies, and many amplifiers are reported in technical documents and data sheets in industry. Some of them are presented here. In papers [157–159], amplifiers are fabricated using MMIC techniques with impedance matching for the input and output circuits. Paper [3] has stated a technique of amplifier design with integration of substrate integrated waveguide (SIW) based on input and output impedance matching for the power gain. Other papers on small signal or low noise amplifiers designs discussed in [160–165] are designed based on input and output impedance match for the circuits either for power gain or optimal noise figure with the trade-off between gain and the noise performance. Papers [166, 167] propose new methodologies for designing and implementing power amplifiers using low-pass filter prototypes. Low-pass filter matching networks are designed and implemented for the transistor matching. Paper [168] presents a matching network design approach using filter prototype and the matching network elements can be determined mathematically. However, none of them utilise a coupling matrix synthesis approach.

Some examples of bandpass filtering amplifiers are reviewed as follows. In [155], a 20-to-40 GHz bandpass amplifier was fabricated with MMIC techniques. The bandpass filter is designed by introducing input match for lowpass and DC block and RF choke for highpass on both input and output matching networks. The impedance matching circuits on both input and output with the high-pass DC block and RF choke circuit gives the bandpass characteristic. The input and output matching networks are designed and analysed with image-parameter filter theory. In [156], a narrowband high-selective active bandpass filter with two passive filters adjacent with one amplifier is presented. Two separate filters are placed before and after the transistor,

and the transistor is matched with distributed network. The measured results give 6.8 dB gain at 2 GHz and the fractional bandwidth is 2.4 % with minimal noise figure of the active filter 2.6 dB of the passband. In these deigns [155, 156], the filters are connected with the matched amplifier, and matching networks for the transistor at the input and output are required.

5.3 A Simplified FET Small-Signal Model

General background about transistors are available in [1, 153, 169]. In this thesis, an FET named NE3210S01 [170] is employed in design using its small signal model at the operating point of $V_D = 2$ V and $I_D = 10$ mA. The simplified calculations are carried out for the small signal transistor model using the model in Figure 4.3 using the information in transistor datasheet [170] and comparing the simulation results that from the ADS [171] circuit model to the manufacturer S-parameters.

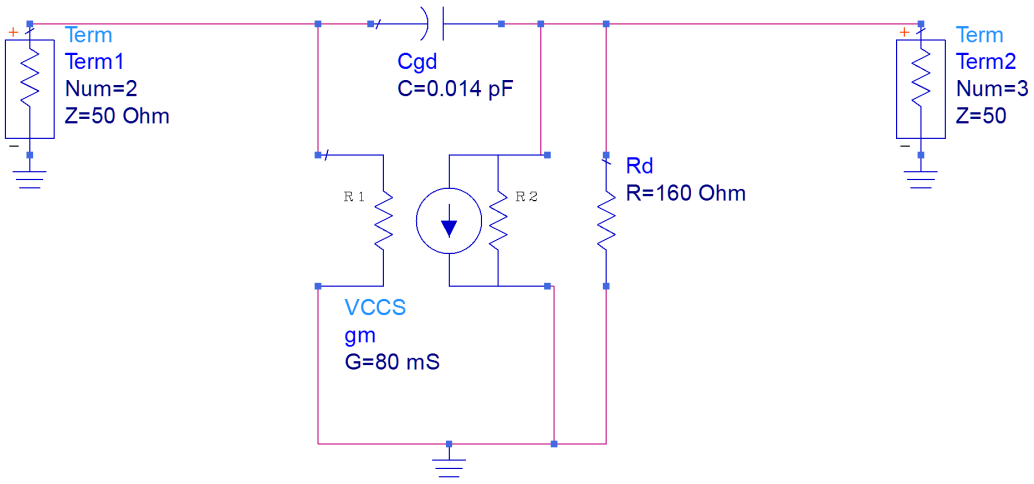

Figure 5.1: A simplified small signal transistor model with a voltage controlled current source for NE3210S01

Figure 5.1 shows the simple circuit small-signal model built in ADS for the NE3210S01 transistor which is constructed by a voltage controlled current source (VCCS) with specified $g_m = 80$ mS and an additional capacitor C_{gd} in parallel with capacitance as given from the data sheet as

0.014 pF. The drain resistance r_d is 160 Ω. This model can approximate the frequency responses for the transistor over the X-band frequency range in terms of S-parameters such as S_{21} and S_{12}, and is verified by the simulation results in the datasheet [170]. Note that the drain resistance r_d can be transformed into the drain conductance g_d by $g_d = 1/r_d$. The R1 and R2 are configured as open circuits and necessary resistance for the transistor has been considered using Rd.

The simulation results the simplified transistor model versus the transistor s2p data are shown in Figure 5.2. The blue curves are from the transistor data s2p and the red ones are from the simpler model. As this simpler circuit model does not include any parasitic elements for a transistor, approximations are acceptable for the model at X band from 8-10 GHz in terms of S_{11} and S_{21}. More accurate approximations can be archived, but it will lead to a more complex circuit model.

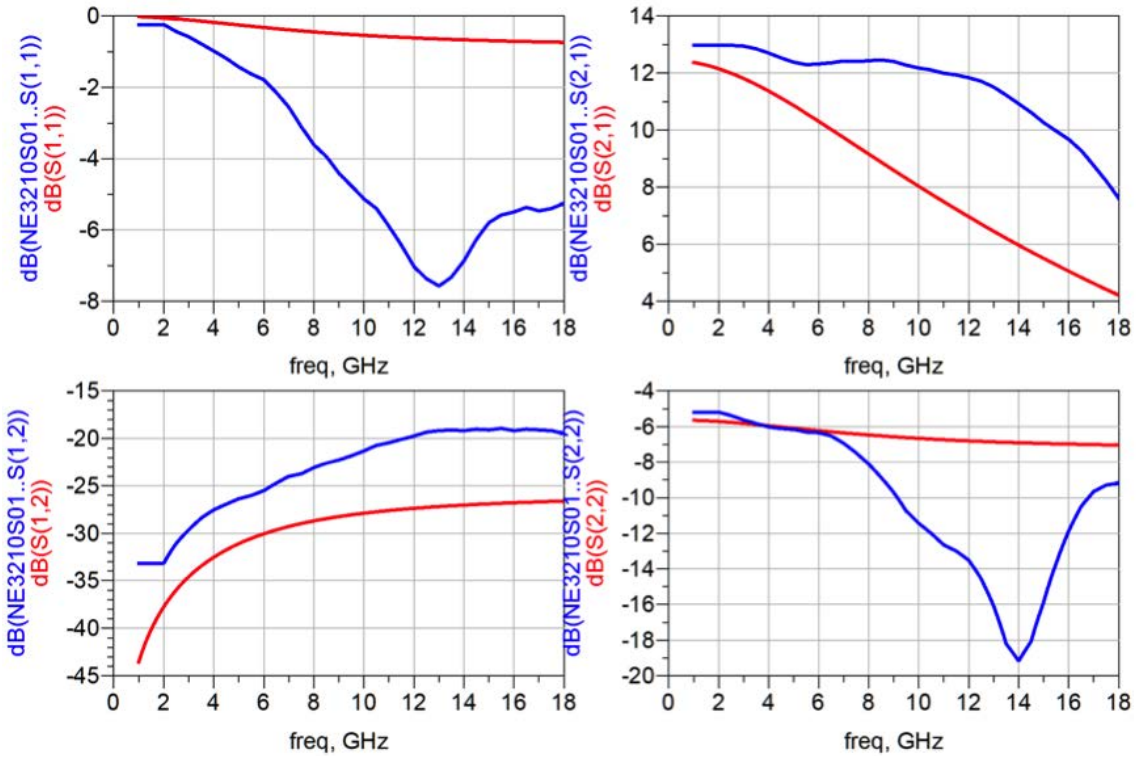

Figure 5.2: Simulation results for circuit model versus transistor s2p data.

In summary, the small-signal model for the transistor for the selected operating frequency is

simplified as a circuit consists of a VCCS with g_m = 80 mS, a capacitor C_{gd} = 0.014 pF and a resistor r_d = 160 Ω.

5.4 Microstrip Filtering Amplifier Design Overview

The coupled resonator circuit topology for the third order microstrip filtering amplifier is shown in Figure 5.3. This reflects the topology introduced in Section 4.6, Chapter 4 where a transistor is incorporated with the last resonator.

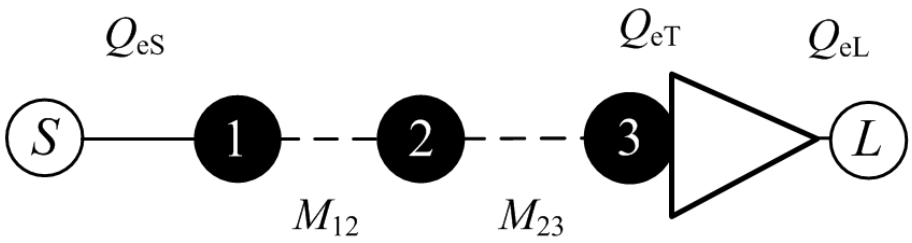

Figure 5.3: The topology for the waveguide filtering amplifier circuit

The source and load nodes are denoted as white circles, and three resonators are denoted as black circles. The dotted line between adjacent resonators mean the inter-resonator coupling. A transistor is incorporated with the third resonator. The corresponding coupling coefficients M and external quality factors Q are denoted.

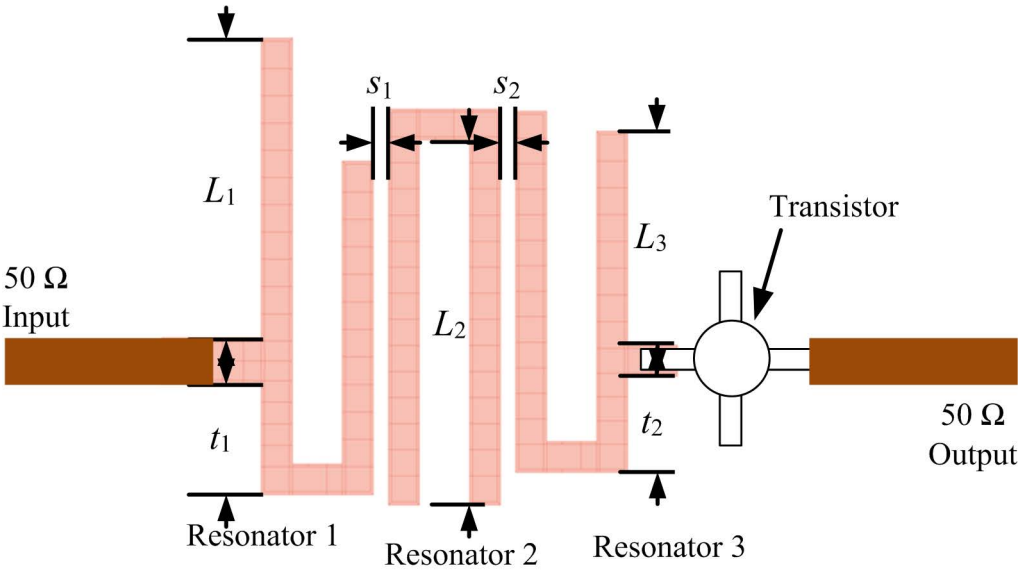

Figure 5.4: Microstrip hairpin filtering amplifier layout illustration

Figure 5.4 illustrates the structure for implementation with hairpin resonators. Practically, the first two resonators are constructed with conventional hairpin resonators and the conventional synthesis and design approach can apply to extract the physical dimensions [125] from the external quality factor Q_{eS} and coupling coefficients M. Conventional hairpin resonators (Resonator 1 and Resonator 2) are used with their resonating frequency determined by L_1, and the external quality factor Q_{eS} is controlled by the tapped position t_1. The critical point is to design the amplifier circuit as a coupled resonator circuit. In this design, the integrated transistor resonator structure is characterised by its overall external quality factor Q_{eT}, which is determined by t_2 and L_3. Resonator 3 is then coupled with other hairpin resonators with the inter-resonator coupling is described by coupling coefficients M_{21} and M_{32}, which is controlled by the coupling gap s_1 and s_2. More details are given from Section 5.6.1.

5.5 Microstrip Filtering Amplifier Coupling Matrix Description

We now consider more details of the microstrip filtering amplifier design with coupling matrix description. For this example microstrip filtering amplifier, the specification is a centre frequency of 8.4 GHz, bandwidth of 500 MHz with the third order Chebyshev filtering characteristics. The details of the matrix synthesis is based on Chapter 4 with the general circuit matrix $[A]$ to describe the third order filtering amplifier example, consisting of four separate sub-matrices $[q]$, $[U]$, $[m]$ and $[T]$ as,

$$[A] = [q] + p[U] - j[m] + [T] \tag{5.5.1}$$

The filtering characteristics coupling matrix synthesis is described first and then it is combined with amplification part.

Filtering characteristics matrix synthesis

The filtering characteristics of the third order filtering amplifier is assumed to be a synchronously tuned Chebyshev filter for simplicity. The general coupling matrix for the filter specification can be approximated with the synthesis by the lowpass filter prototype [125, 147]. It is a third order Chebyshev filter. The fractional bandwidth $FBW = 0.5/8.4 = 0.06$ with the centre frequency $f_0 = 8.4$ GHz. The g values for its lowpass prototype Chebyshev filter are tabulated in Table 5.1 for the specification of 20 dB return loss S_{11} in the passband.

g_0	g_1	g_2	g_3	g_4
1	0.8516	1.1032	0.8516	1

Table 5.1: Element values for Chebyshev Lowpass Prototype, third order, -20 dB S_{11} in passband.

The scaled external quality factor q_{eS} and q_{eT} are calculated by [125]

$$\begin{aligned} q_{eS} &= g_0 g_1 \\ q_{eT} &= g_3 g_4 \end{aligned} \tag{5.5.2}$$

then $q_{eS} = q_{eT} = 0.8516$.

The external quality factor $[q]$ matrix can be expressed as

$$[q] = \begin{bmatrix} 1.1743 & 0 & 0 & 0 \\ 0 & 0 & 0 & 0 \\ 0 & 0 & 1.1743 & 0 \\ 0 & 0 & 0 & \frac{1}{q_{eL}} \end{bmatrix} \tag{5.5.3}$$

The normalised coupling coefficients can be found via [125]

$$m_{i,i+1} = \frac{1}{\sqrt{g_i g_{i+1}}} \quad for\ i = 1\ , 2 \tag{5.5.4}$$

Thus the calculated normalised coupling coefficients are $m_{12} = m_{21} = m_{23} = m_{32} = 1.0317$, and they are used to estimate the filtering characteristics. The normalised coupling coefficients fill the corresponding elements of the normalised coupling matrix $[m]$ as

$$[m] = \begin{bmatrix} 0 & 1.0317 & 0 & 0 \\ 1.0317 & 0 & 1.0317 & 0 \\ 0 & 1.0317 & 0 & m_{gd} \\ 0 & 0 & m_{gd} & 0 \end{bmatrix} \tag{5.5.5}$$

Amplification characteristics matrix synthesis

To complete the matrix synthesis for the design, the amplifier characteristic matrix is described based on the extended coupling matrix with additional transistor matrix $[T]$. It includes the simplified transistor model consisting of the transconductance g_m, output drain conductance g_d and gate-to-drain capacitor C_{gd}. The provided values in the transistor model are given in Section 5.3 as $g_m = 80$ mS, $r_d = 160\ \Omega$ and $C_{gd} = 0.014$ pF.

The output circuit connects to a 50 Ω termination, namely, the load conductance $G_L = 0.02$ S. The scaled external quality factor therefore is $q_{eL} = 0.8516$ using the definition for scaled load external quality factor q_{eL} in Chapter 4. The scaled external quality factor matrix $[q]$ for the filtering amplifier is

$$[q] = \begin{bmatrix} 1.1743 & 0 & 0 & 0 \\ 0 & 0 & 0 & 0 \\ 0 & 0 & 1.1743 & 0 \\ 0 & 0 & 0 & 1.1743 \end{bmatrix} \tag{5.5.6}$$

The matrix $[U]$ is

$$[U] = \begin{bmatrix} 1 & 0 & 0 & 0 \\ 0 & 1 & 0 & 0 \\ 0 & 0 & 1 & 0 \\ 0 & 0 & 0 & 0 \end{bmatrix} \tag{5.5.7}$$

The coupling coefficient m_{gd} is defined from Equation (4.6.7) and (4.6.10), and is calculated as $m_{gd} = 0.04338$.

Thus, the full normalized coupling matrix $[m]$ is expressed as

$$[m] = \begin{bmatrix} 0 & 1.0317 & 0 & 0 \\ 1.0317 & 0 & 1.0317 & 0 \\ 0 & 1.0317 & 0 & 0.04338 \\ 0 & 0 & 0.04338 & 0 \end{bmatrix} \tag{5.5.8}$$

The newly introduced transistor matrix $[T]$ consists of two main elements, and their numerical values are $T_{g_m} = 4.6972$ and $T_{g_d} = 0.3670$ by Equation (4.6.18).

The numerical representation for the transistor matrix $[T]$ is shown as

$$[T] = \begin{bmatrix} 0 & 0 & 0 & 0 \\ 0 & 0 & 0 & 0 \\ 0 & 0 & 0 & 0 \\ 0 & 0 & 4.6972 & 0.3670 \end{bmatrix} \tag{5.5.9}$$

The calculated theoretical S-parameters by the matrix Equations (5.5.6)-(5.5.9) for the filtering amplifier are shown in Figure 5.5 with Equation (4.8.6) to generate the its corresponding scattering parameters.

So far, the coupling matrix synthesis is approximately based on synchronously tuned filter from the Ladder circuit model, however, the coupled resonator circuit model for the filtering amplifier introduced in Chapter 4 is not identical to the Ladder circuit model as additional conductance and capacitance components are introduced. The filter synthesis based on Chebyshev lowpass prototype filter can only give the approximations for the coupled resonator circuit with the transistor included. Hence, Figure 5.5 are not perfect Chebyshev responses.

Further coupling matrix manipulations are implemented by introducing self-coupling coefficients m_{11}, m_{22} and m_{33} into general normalised coupling matrix $[m]$ to recover the conventional Chebyshev filter responses. The resultant normalised coupling matrix with self coupling coeffi-

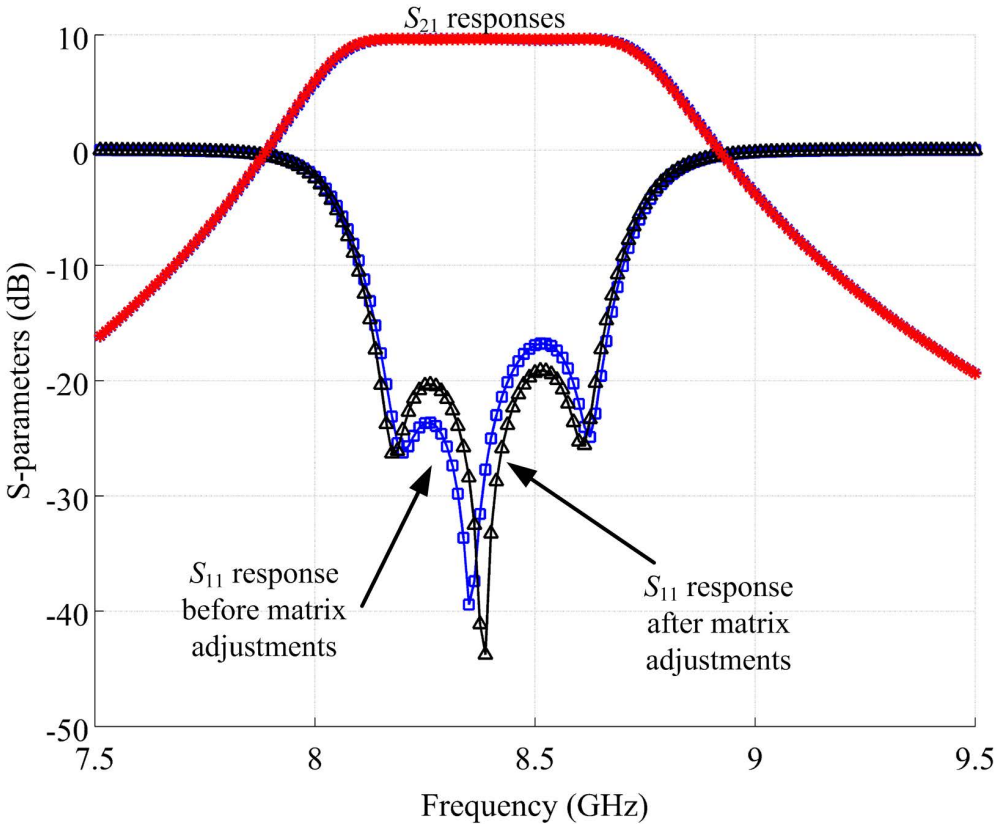

Figure 5.5: Theoretical calculation results for a third order Chebyshev filtering amplifier.

cients are obtained by optimisation for maximum 20 dB return loss in passband as

$$[m] = \begin{bmatrix} 0.01 & 1.0317 & 0 & 0 \\ 1.0317 & -0.04 & 1.0317 & 0 \\ 0 & 1.0317 & 0.02 & 0.04338 \\ 0 & 0 & 0.04338 & 0 \end{bmatrix} \tag{5.5.10}$$

The theoretical S-parameters from the circuit matrix are plotted again in Figure 5.5 with the new normalized coupling matrix Equation (5.5.10).

In terms of the design procedures, special treatments may be required for the asynchronously tuned resonators where $m_{ii} \neq 0$, which means that each resonator can resonate at another frequency rather than midband frequency f_c. The resonating centre frequency f_{ii} of each resonator

can be obtained with the equation given as [172]

$$f_{ii} = f_c \sqrt{\frac{2 + m_{ii} \times FBW}{2 - m_{ii} \times FBW}} \tag{5.5.11}$$

where f_c is the centre frequency of the midband filter design with $f_c = 8.4$ GHz in this case. The m_{ii} is the self-coupling coefficient for asynchronous tuning. FBW is the fractional bandwidth. The centre frequency of the filter is $f_c = 8.4$ GHz and the centre frequency of the resonators can be found with Equation (5.5.11) as $f_{11} = 8.4025$ GHz, $f_{22} = 8.3925$ GHz and $f_{33} = 8.4050$ GHz respectively from m_{11}, m_{22} and m_{33}.

5.6 Microstrip Filtering Amplifier Resonator Design using Coupling Matrix

The microstrip filtering amplifier is specified with the centre frequency at 8.4 GHz with bandwidth of 500 MHz from 8.15 GHz to 8.65 GHz with targeted best return loss for 20 dB in passband. By using the coupling matrix for this circuit presented previously in Section 5.5, the circuit matrix for the hairpin filtering amplifier has the filter scaled bandwidth coupling matrix $[M]$ using Equations (4.4.8) and (4.4.9) as,

$$[M] = \begin{bmatrix} 0.0006 & 0.0614 & 0 & 0 \\ 0.0614 & -0.0024 & 0.0614 & 0 \\ 0 & 0.0614 & 0.0012 & 0.00015 \\ 0 & 0 & 0.00015 & 0 \end{bmatrix} \tag{5.6.1}$$

with the external quality factors of $Q_{eS} = Q_{eT} = Q_{eL} = 14.3$.

Based on the calculations for the resonating frequencies f_{ii} using the self-coupling coefficients m_{ii} in the last section, the resonating frequencies for each resonator are very close to the filter centre frequency $f_c = 8.4$ GHz. These three resonators will be treated as resonating at f_c for

simplification.

Realisations on physical dimensions for each resonator as shown in Figure 5.4 are given below based on the Rogers 5870 substrate of 0.254 mm thick with dielectric constant of 2.33.

5.6.1 External quality factor extraction for Resonator 1

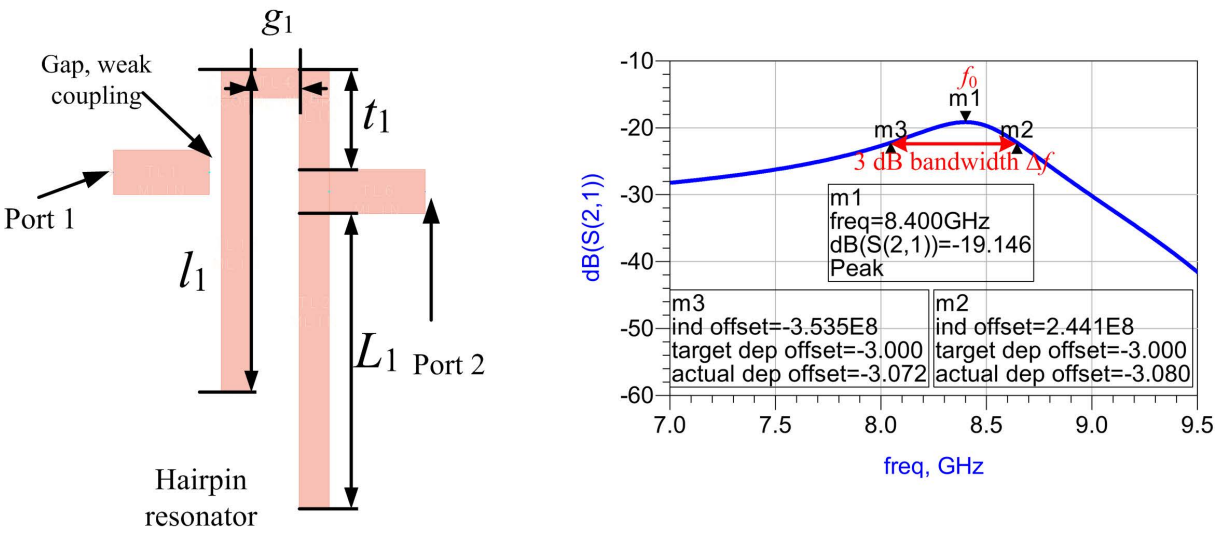

(a) (b)

Figure 5.6: (a) Hairpin resonator to extract the external quality factor Q_{eS}. (b) ADS Momentum simulation results of the hairpin resonator.

Figure 5.6 (a) shows the configuration to calculate the Q_{eS}. The external quality factor Q_{eS} can be calculated from the resonator centre frequency f_0 over the 3-dB bandwidth Δf from results of S_{21} in dB versus frequencies, thus the external quality factor Q_{eS} can be found as [125]:

$$Q_{eS} = \frac{f_0}{\Delta f} \tag{5.6.2}$$

The length of the hairpin resonator L_1 determines the centre resonant frequency and the feedline tapping position t_1 determine the external quality factor [125].

Figure 5.6 (b) shows the circuit response using ADS Momentum for the hairpin resonator. The quality factor is $Q_{eS} = 14.314$ at 8.4 GHz for a standard hairpin resonator. In this configuration,

the corresponding dimensions (in mm) are $l_1 = 5.4$, $L_1 = 4.8$, $g_1 = 0.8$, $t_1 = 1.7$.

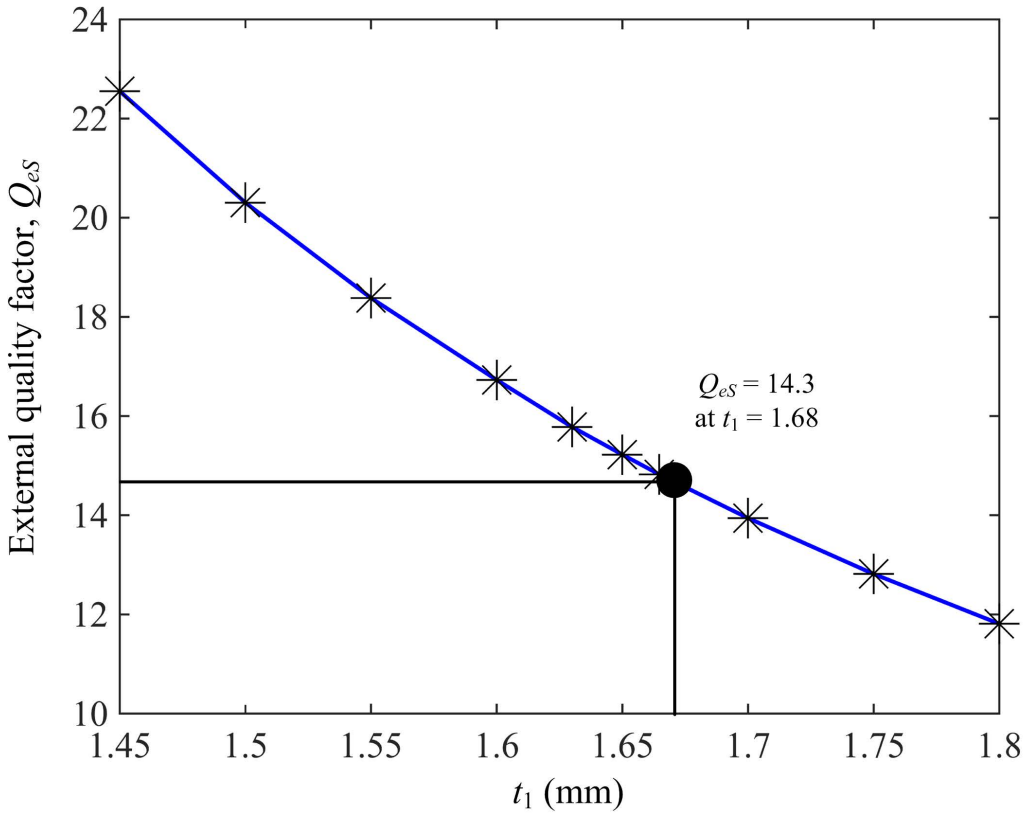

Figure 5.7: External quality factor Q_{eS} vs tapping position t_1

Additionally, Figure 5.7 shows the design curve of Q_{eS} versus the tapping position t_1. The required external Q_{eS} can be read off from the design curve in Figure 5.7.

5.6.2 External quality factor extraction for Resonator 3

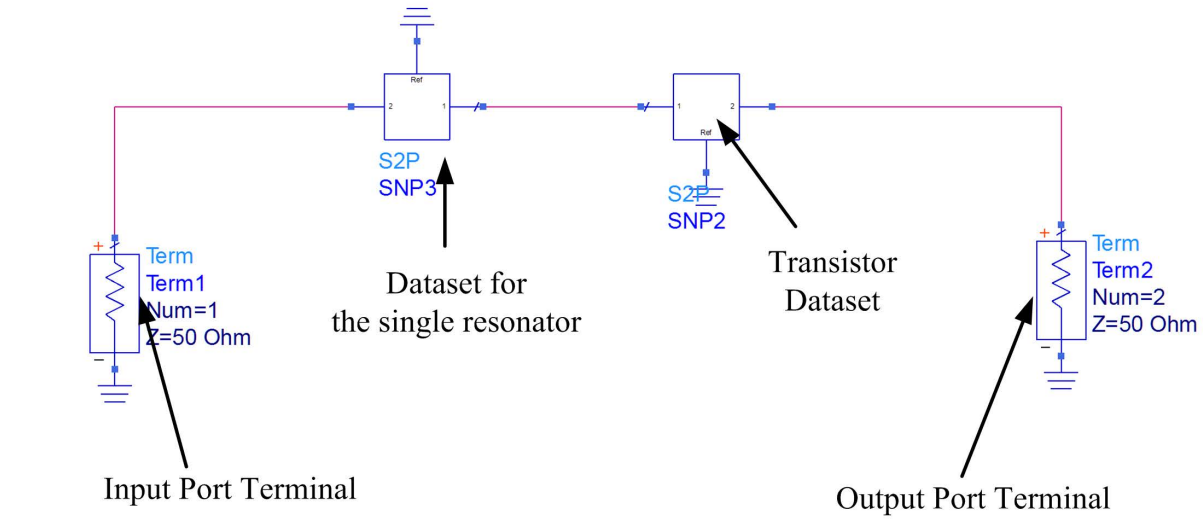

(a)

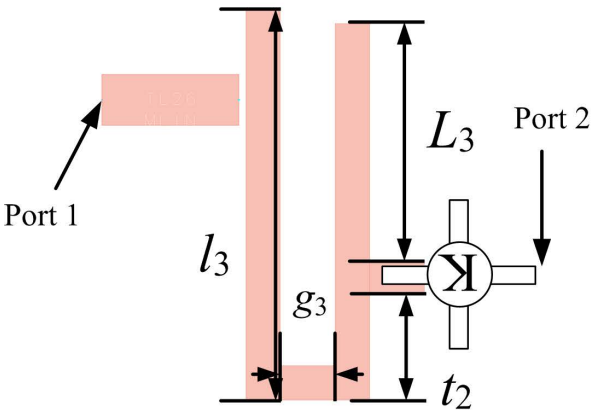

(b)

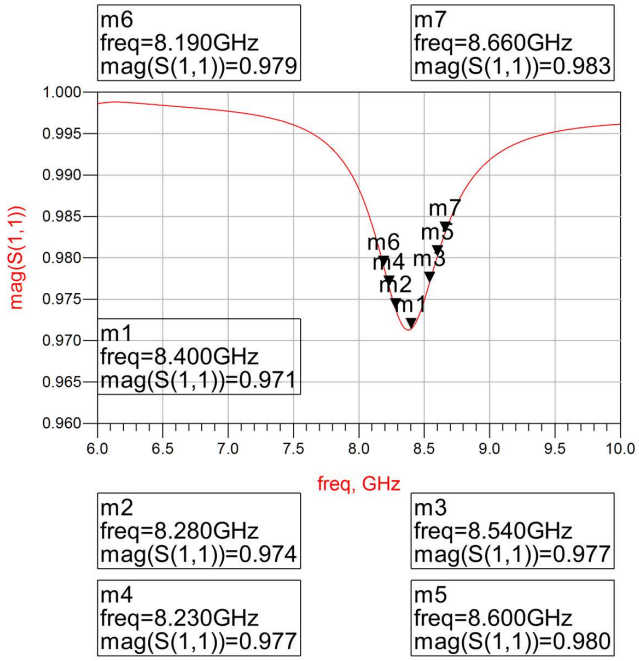

(c)

Figure 5.8: (a) Simulation configurations to extract the external quality factor Q_{eT} from the integrated hairpin resonator with the transistor. (b) The circuit layout for the integrated hairpin transistor resonator. (c)Simulation results for the integrated hairpin resonator with the transistor.

Figure 5.8 (a) illustrates the transistor input circuit connected with the hairpin resonator. It uses the measured transistor dataset for transistor NE3210S01 from the manufacturer. Figure 5.8 (b) is the circuit layout for the hairpin resonator with the transistor. The external quality factor $Q_{eT} = 13.867$ is calculated from the simulation results of the integrated hairpin resonator from Figure 5.8 (c) using the reflection response S_{11} in [173]. The corresponding dimensions (in mm) are $l_3 = 5.7$, $g_3 = 0.8$, $t_2 = 1.53$, $L_3 = 3.67$. The extraction for the external quality factor is described in Appendix A. As the resonator is weakly coupled, the differences of the magnitude in S_{11} are not obvious. A stronger coupling for the measurement in Figure 5.8 (b) can be used to achieve more accurate calculations.

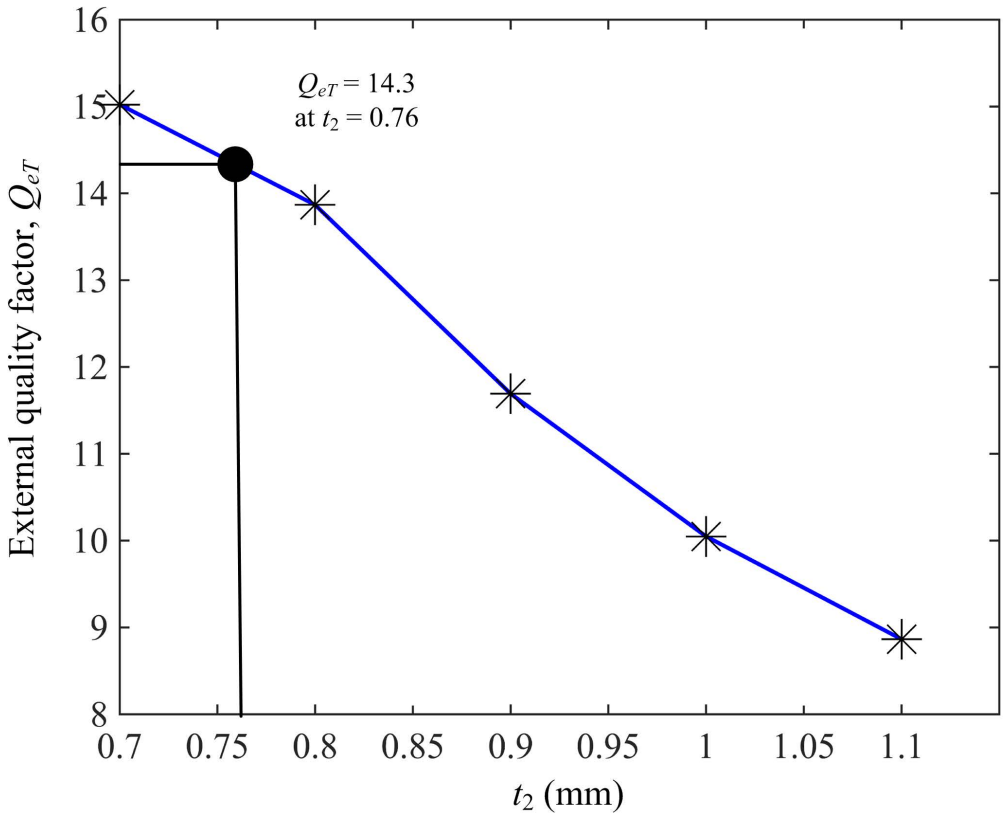

Figure 5.9: External quality factor Q_{eT} vs tapping position t_2

Figure 5.9 shows the relationship of the external quality factor Q_{eT} versus the tapping position t_2. The value for t_2 can be read off from the figure according to Equation (5.6.1).

5.6.3 Coupling coefficient extractions for Resonator 2

The coupling coefficient M is calculated based on the relationship between two resonators [125] as shown in Figure 5.10.

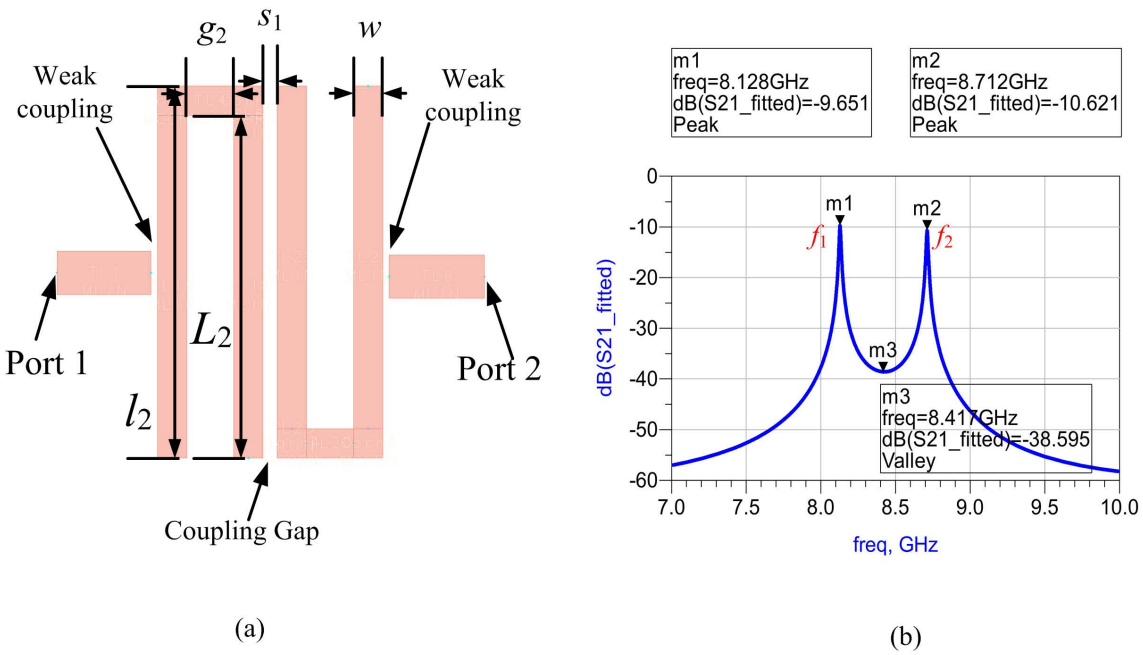

(a) (b)

Figure 5.10: (a) The circuit to extract the coupling coefficient. (b) Simulation results of two resonators to extract coupling coefficient.

Figure 5.10 (a) shows the circuit layout for calculating the coupling coefficient M using two ports with weak coupling for each resonator. The resonating centre frequency is determined by the hairpin arm length L_2. The distance between the adjacent resonators s_1 determines the coupling coefficient between the resonators [125]. Two identical resonators with the same length L_2 and width w are placed adjacently with gap s_1, and each resonator has the same centre frequency at 8.4 GHz. Both excitation ports are connected with 50 Ω microstrip lines and weakly coupled to the resonators for more accurate calculation.

The coupling coefficient M can be calculated with Equation (5.6.3) [125],

$$M = \frac{{f_1}^2 - {f_2}^2}{{f_1}^2 + {f_2}^2} \tag{5.6.3}$$

where f_1 and f_2 are the resonant frequencies, which are the frequencies of the peaks in S_{21}. In this case, f_1 and f_2 are denoted as m1 = 8.128 GHz and m2 = 8.712 GHz in Figure 5.10 (b), giving the coupling coefficient as $M = 0.61$. The corresponding dimensions (in mm) are $l_2 = 6.34$, $g_2 = 0.8$, $L_2 = 5.84$, $s_1 = 0.38$, $w = 0.5$.

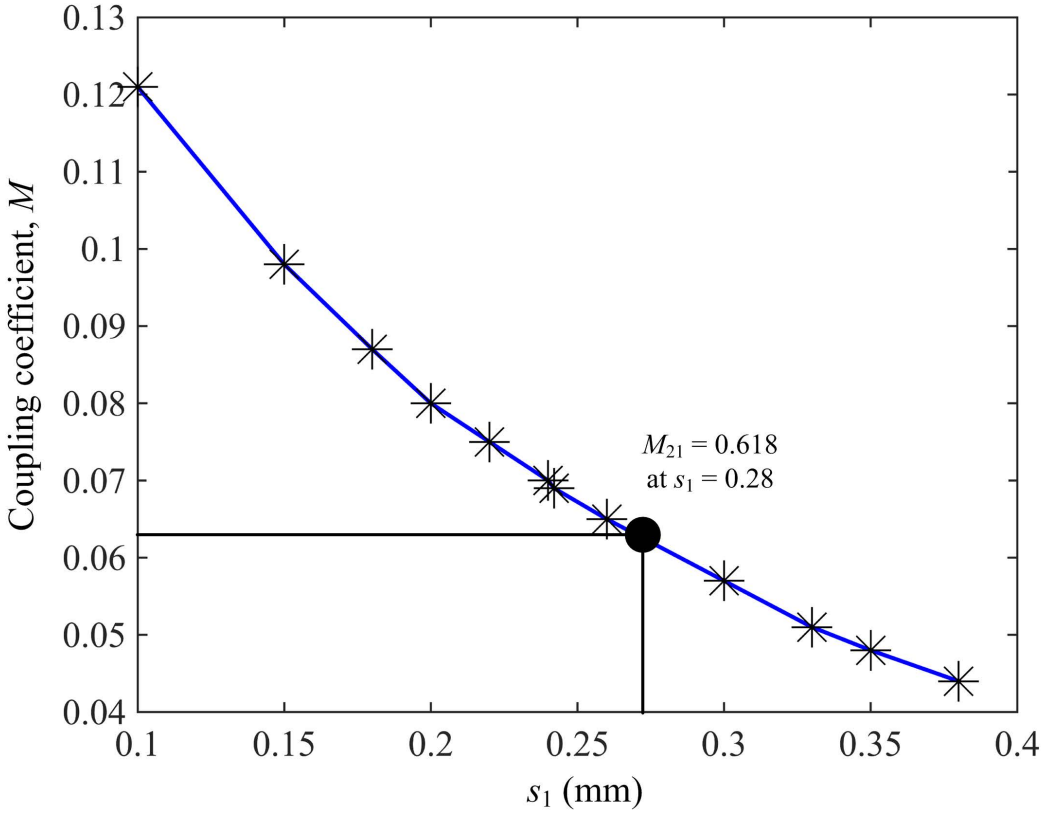

Figure 5.11: Coupling coefficient M_{21} vs coupling gap s_1

The relationship of coupling coefficient M_{21} versus the coupling gap s_1 is illustrated in Figure 5.11, where the dimension s_1 can be read off the figure according to Equation 5.6.1.

5.7 Microstrip Filtering Amplifier Full Implementation

With the previous calculations, the specific resonators for the microstrip hairpin filtering amplifier have been designed by extracting the external quality factors as well as the coupling coefficients for the specification.

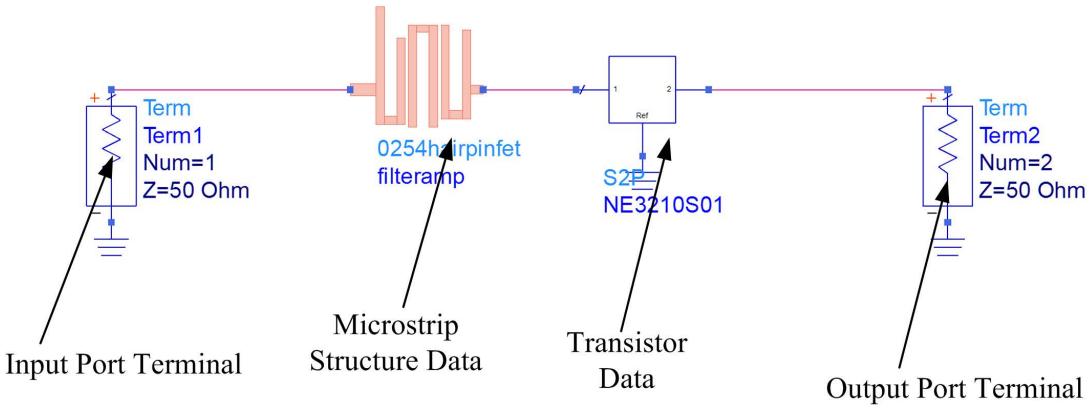

Figure 5.12: ADS schematics simulation for the microstrip structure with the transistor

As illustrated in the layout in Figure 5.12, the three hairpin resonators have been put together and the third hairpin resonator is integrated with the transistor input circuit, forming the microstrip amplifier. The transistor NE3210S01 data is represented by the manufacturer's measured S-parameter data [170]. In this circuit, the bias and stabilisation circuits are not included. Figure 5.13 shows the ADS simulation results with the circuit schematics in Figure 5.12. Figure 5.14 shows the circuit can achieve best noise performance 0.78 dB by simulation in the passband and it is unconditionally stable from 6 GHz to 10 GHz by ADS circuit simulations.

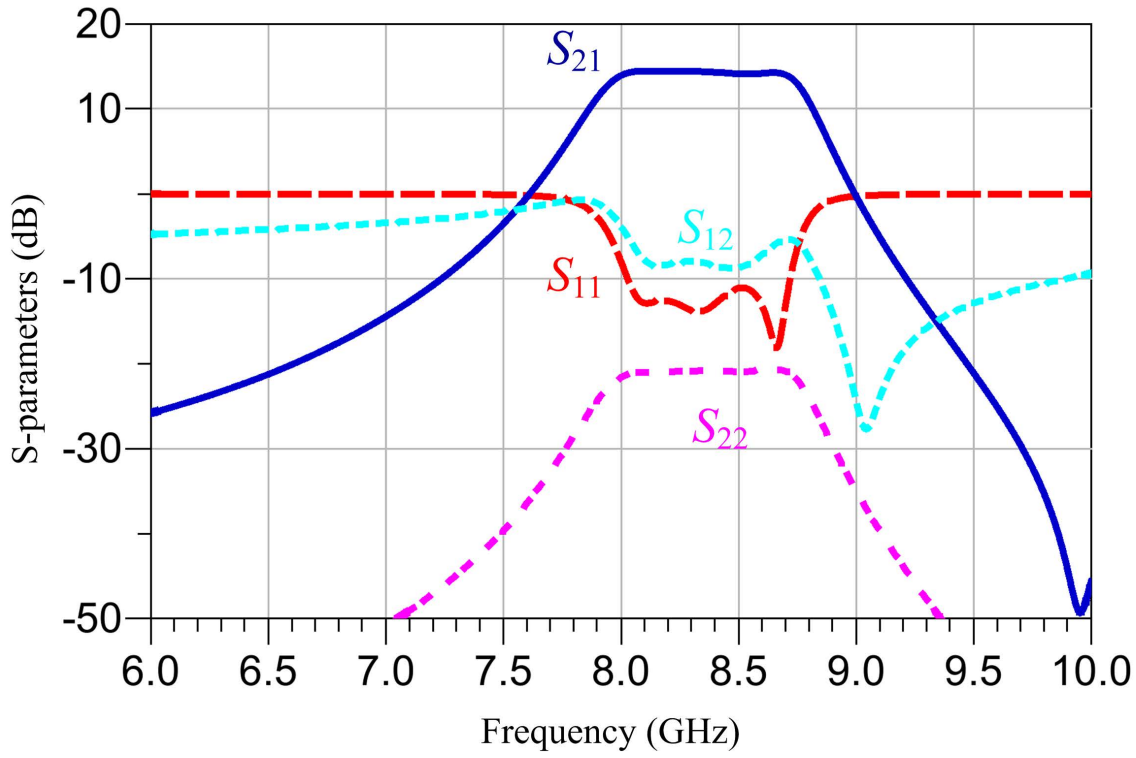

Figure 5.13: Simulated results for the microstrip structure with the transistor.

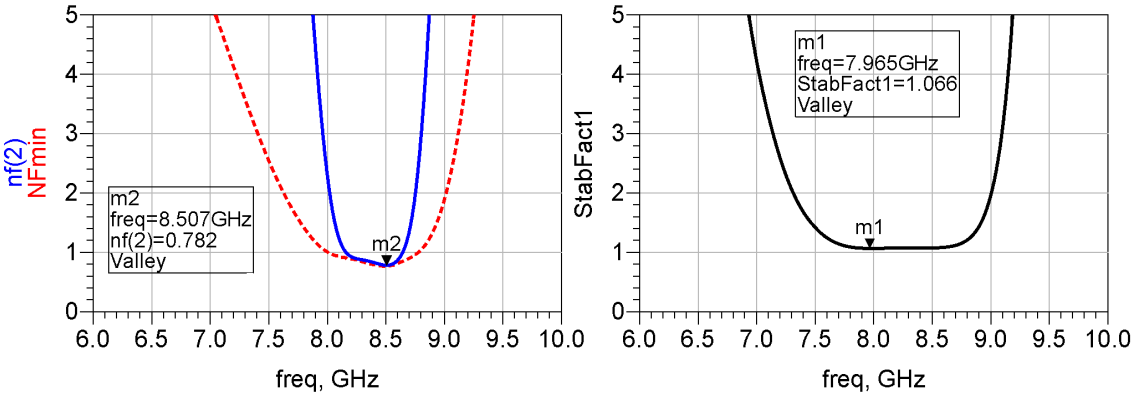

Figure 5.14: Simulated results for the microstrip amplifier for noise figure (in dB) and stability.

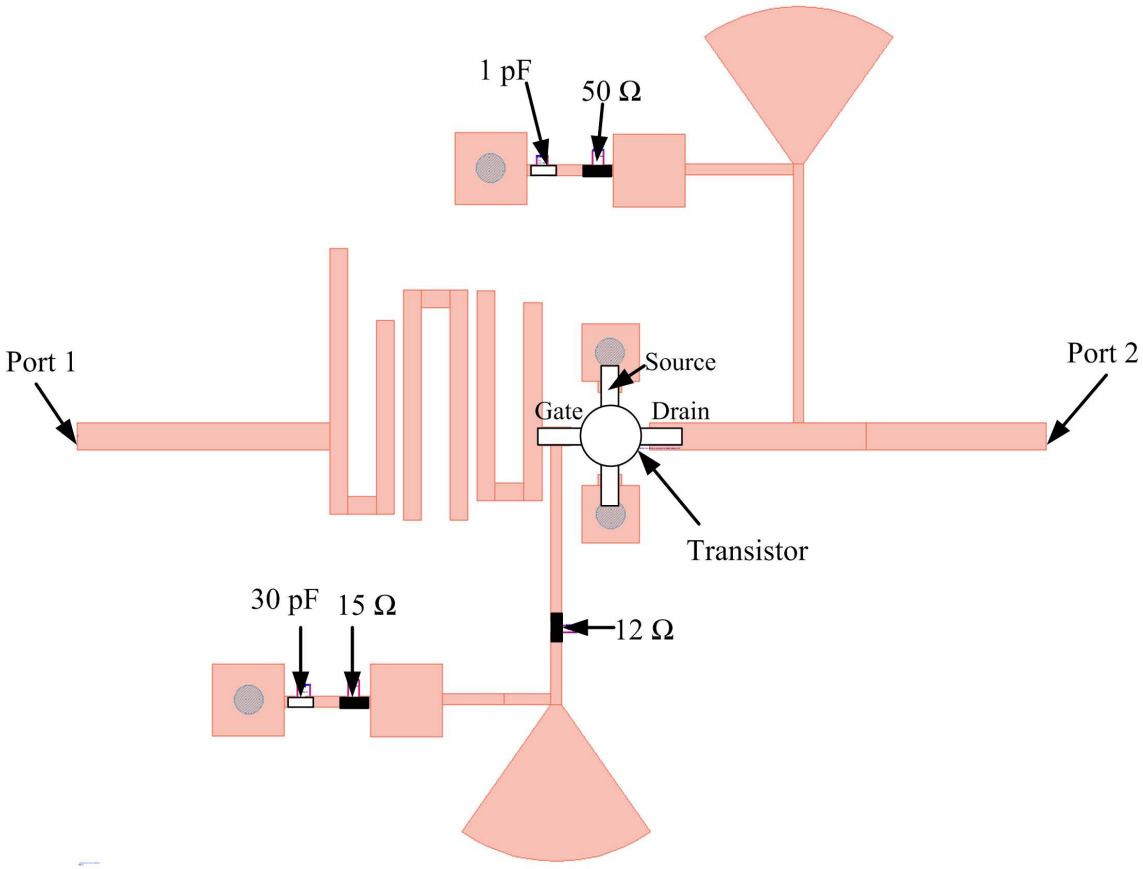

Figure 5.15: Circuit configurations for the full hairpin filtering amplifier

The micorstrip hairpin filtering amplifier layout is optimised for best S_{11} (e.g. target -20 dB for S_{11}) for the specified passband 500 MHz bandwidth and the optimised simulation results are shown together with the measurement results in Figure 5.19. Figure 5.15 shows the completed circuit and layout for the hairpin filtering amplifier. The circuit is terminated with two 50 Ω ports. The transistor bias and stabilisation circuits are designed using radial stubs [169]. It also shows the amplifier configuration for the whole microstrip amplifier with the Surface Mount Device (SMD) components (e.g., resistors, capacitors), and the components values are annotated as well. A 12 Ω resistor is used to improve the stability of the circuit but it will downgrade the overall noise performance. Figure 5.16 shows the stability and noise figure for the complete circuit.

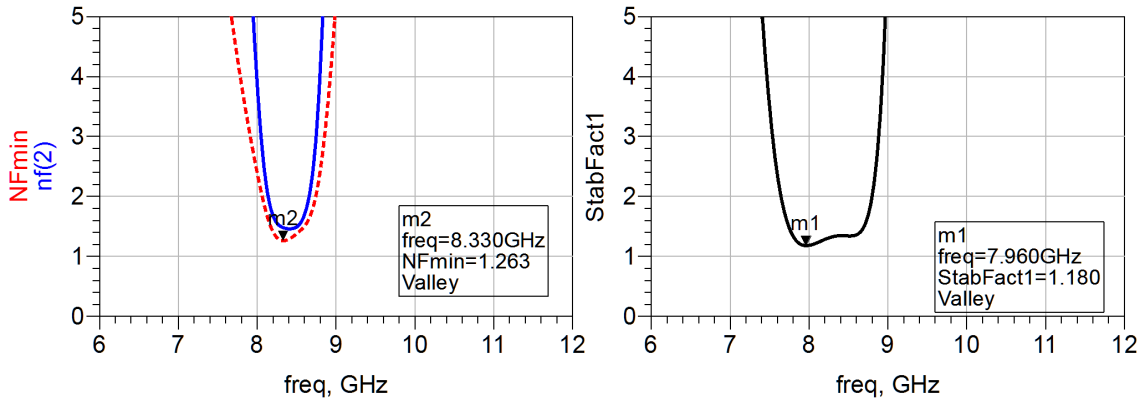

Figure 5.16: Simulated results for the complete amplifier for noise figure (in dB) and stability.

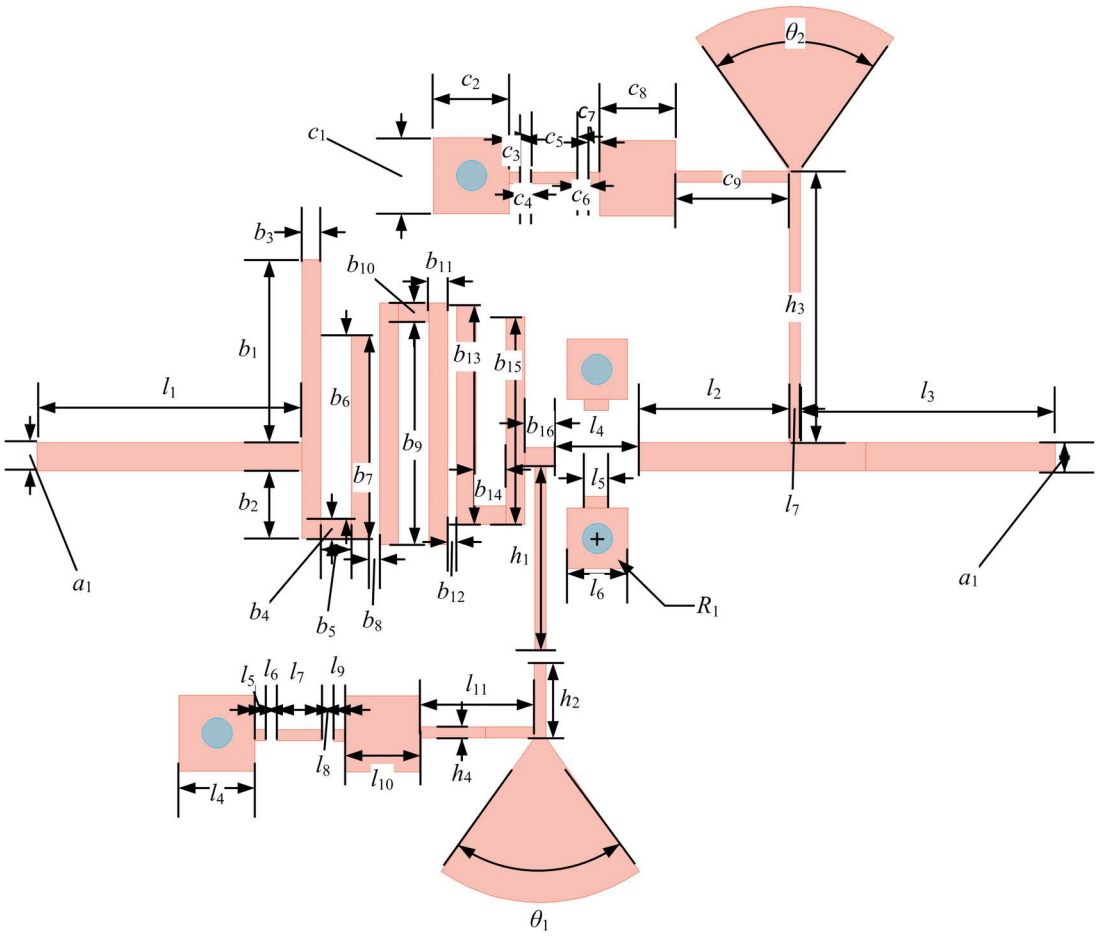

Figure 5.17: Layout for the complete microstrip filtering amplifier.

Figure 5.17 gives the dimensional details for the microstrip circuit using a 0.254 mm substrate with the dielectric constant of 2.33. The input and output are terminated by 50 Ω microstrip transmission lines with 0.74 mm wide for a_1.

The dimensions (in mm) are $a_1 = 0.74$, $b_1 = 4.83$, $b_2 = 1.79$, $b_3 = 0.5$, $b_4 = 0.5$, $b_5 = 0.8$, $b_6 = 4.878$, $b_7 = 5.378$, $b_8 = 0.242$, $b_9 = 5.883$, $b_{10} = 0.5$, $b_{11} = 0.5$, $b_{12} = 0.242$, $b_{13} = 5.821$, $b_{14} = 0.8$, $b_{15} = 5.5$, $b_{16} = 0.8$, $c_1 = 2.0$, $c_2 = 2.0$, $c_3 = 0.3$, $c_4 = 0.28$, $c_5 = 1.2$, $c_6 = 0.3$, $c_7 = 0.3$, $c_8 = 2.0$, $c_9 = 3.0$, $h_1 = 4.88$, $h_2 = 2.0$, $h_3 = 7.18$, $h_4 = 0.3$, $l_1 = 7.0$, $l_2 = 4.0$, $l_3 = 7.0$, $l_4 = 2.0$, $l_5 = 0.3$, $l_6 = 0.3$, $l_7 = 1.2$, $l_8 = 0.3$, $l_9 = 0.3$, $l_{10} = 2.0$, $l_{11} = 3.0$, $R_1 = 0.4$, and $\theta_1 = 70°$, $\theta_2 = 70°$.

5.8 Microstrip Amplifier Measurements and Discussions

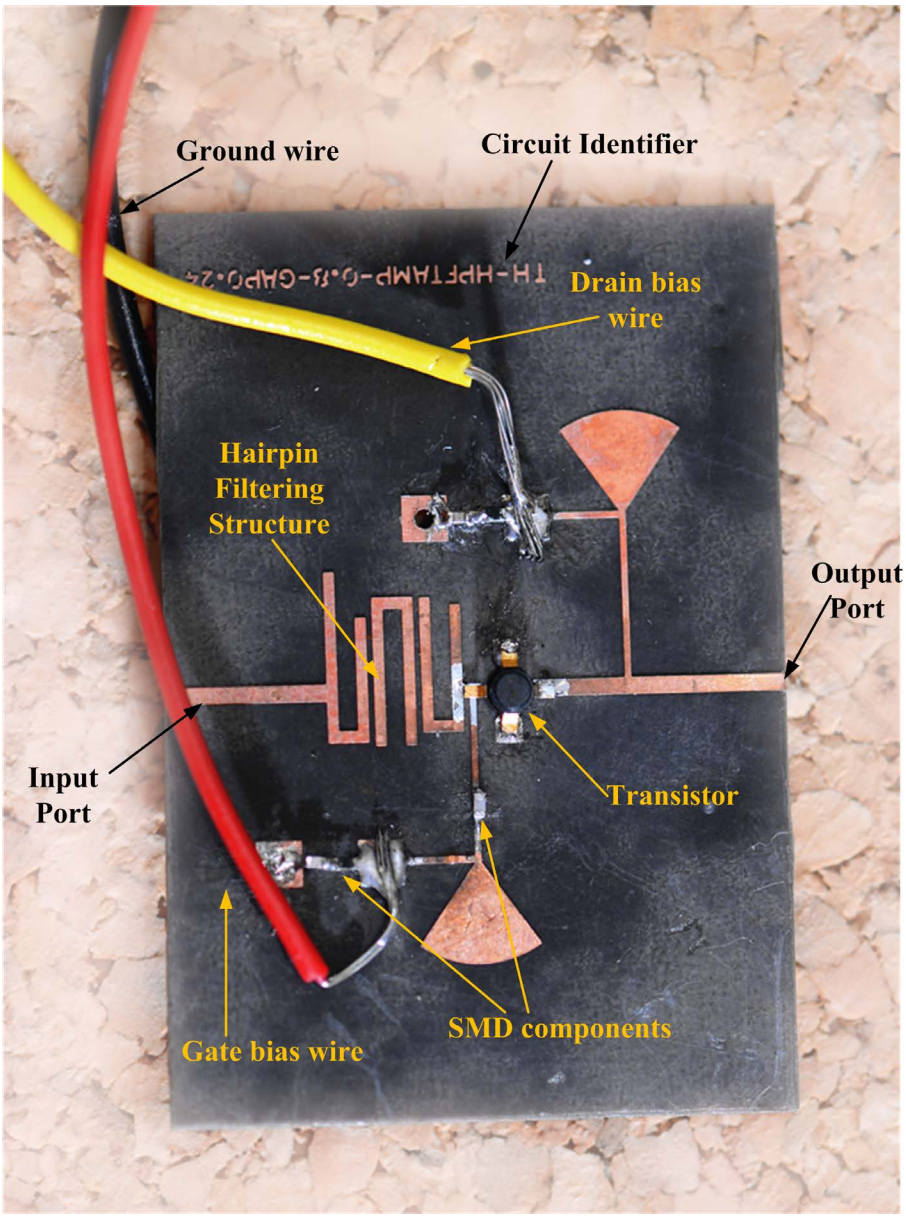

Figure 5.18: The photo of the fabricated circuit.

Figure 5.18 shows the fabricated and assembled microstrip amplifier. The circuit is fabricated on the Rogers Duroid 5870 substrate and its substrate thickness is 0.254 mm, 10 thou, 0.25 oz. copper cladding. The circuits are made and SMD components are mounted.

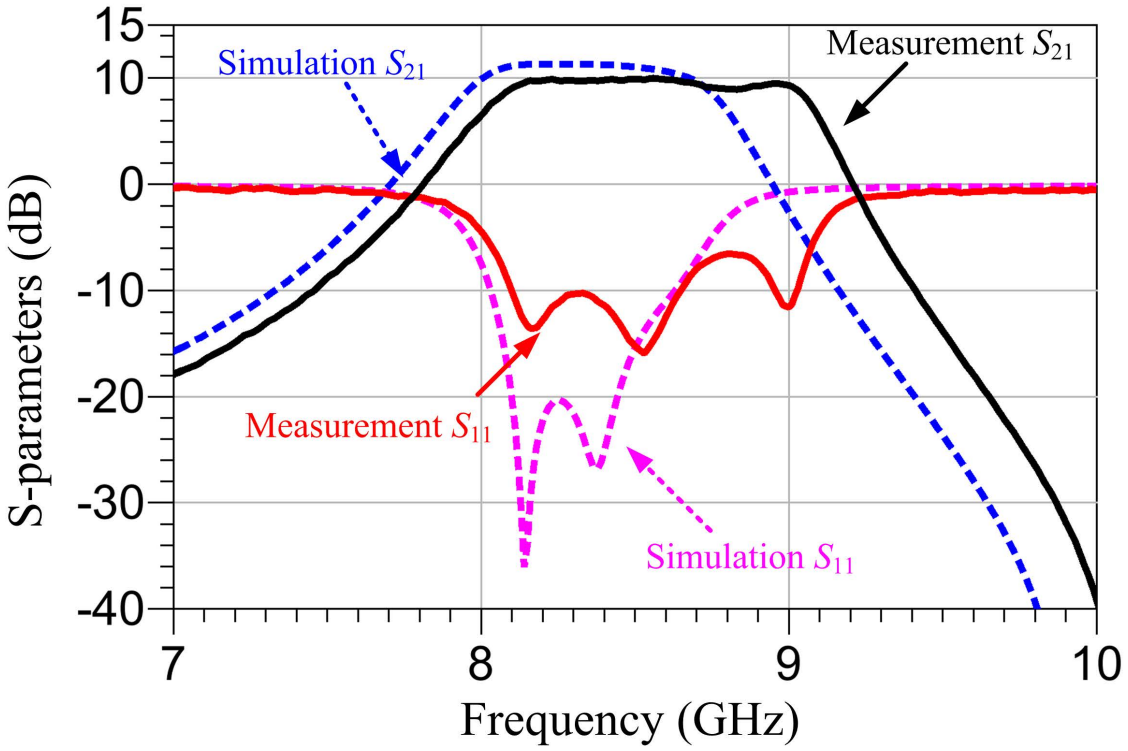

Figure 5.19: Measurement results of the microstrip filtering circuit.

Figure 5.19 shows the VNA measurement results of the microstrip hairpin filtering amplifier versus the simulation results biased at V_D = 2 V and I_D = 10 mA. The measurement results show 3 poles in S_{11} which agree with the third order filtering specification. The return loss S_{11} is at the level of -10 dB with the bandwidth 1 GHz from 8 GHz to 9 GHz as indicated in S_{11} and S_{21}. The simulation results by ADS show the bandwidth of 500 MHz from 8 GHz to 8.5 GHz in S_{11} at -20 dB and gain bandwidth of 600 MHz from 8 GHz to 8.6 GHz in S_{21} at 10 dB gain. The actual fabricated dimensions for the microstrip circuit are measured by a microscope. The critical dimensions illustrated in Figure 5.17 are tabulated in Table 5.2 with the measured dimensions and the modelling dimensions.

Figure 5.20 shows the simulation results using the fabricated microstrip circuit dimensions against the measurement results. As it is shown, the fabrication tolerance could lead to some degrees of the disagreement between the simulation results with the measured ones. The differ-

	Model	Actual		Model	Actual		Model	Actual		Model	Actual
a_1	0.74	0.734	b_4	0.5	0.511	b_8	0.242	0.253	b_{12}	0.242	0.252
b_1	4.83	4.826	b_5	0.8	0.792	b_9	5.883	5.82	b_{13}	5.821	5.813
b_2	1.79	1.804	b_6	4.878	4.762	b_{10}	0.5	0.509	b_{14}	0.8	0.818
b_3	0.5	0.491	b_7	5.378	5.311	b_{11}	0.5	0.492	b_{15}	5.5	5.476

Table 5.2: Microstrip amplifier EM modelling and actual fabricated dimensions.

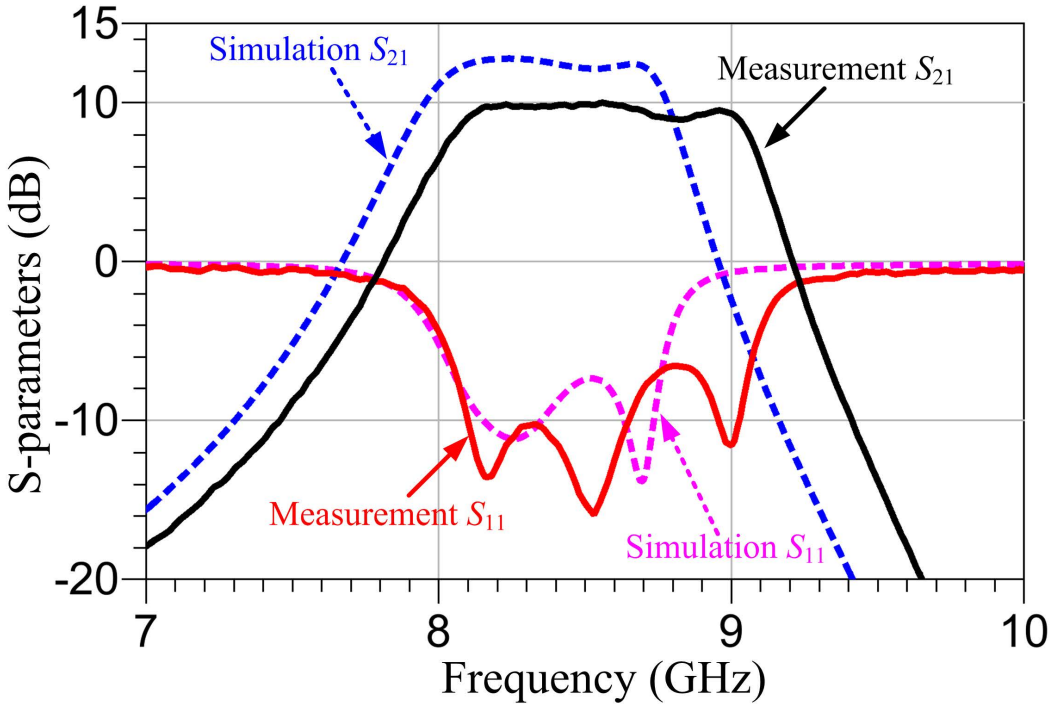

Figure 5.20: Measurement results versus the simulation results using the fabricated dimensions.

ence between the actual substrate dielectric constant and that from the given data sheet could change the electric length of the resonator, leading to a different filter centre frequency and bandwidth [125]. Also, the SMD components assembly and the circuit soldering can change the performance of the amplifier and introduce additional losses [125, 153].

5.9 Summary

In this chapter, a microstrip hairpin filtering amplifier has been demonstrated with the specification of a bandpass third order filter at centre frequency of 8.4 GHz with bandwidth 500 MHz and around 10 dB gain over the bandwidth. The filtering microstrip amplifier is synthesised using Chebyshev lowpass filter prototype based on the novel active coupling matrix introduced in Chapter 4. This design has been implemented by three microstrip resonators consisting of two conventional hairpin resonators and one quasi-hairpin resonator integrated with a transistor. The combined filtering and matching enables the filtering amplifier to be frequency selective as a filter, and transistor input matched for 10 dB gain as an amplifier. Also, the matching and connecting circuit for a combined filter and amplifier design has been largely removed. The measurement results show three clear poles in reflection S_{11} for the filtering characteristics with average -10 dB, and amplification around 10 dB gain from 8 GHz to 9 GHz for S_{21}. Compared to [155, 156], this design presented in this chapter can provide equivalently decent selectivity from the filter characteristics with small circuit size where the filter is integrated with the amplifier. Another demonstrator using the novel coupling matrix (in Chapter 4) is given in Chapter 6 using a waveguide structure.

Chapter 6

Waveguide Bandpass Filtering Amplifier

6.1 Introduction

As has been reviewed in Chapter 2, waveguide amplifier circuits for sub-millimetre or THz frequencies have waveguide input and output with active components or chips mounted onto the planar circuits, such as microstrip lines and coplanar waveguide. Rectangular waveguides are solutions for millimetre and sub-millimetre microwave circuits for low loss performance. A rectangular waveguide to planar circuit (e.g. microstrip, coplanar waveguide etc.) transition is used to couple the electromagnetic energy from the waveguide onto the planar circuit. Planar circuits hold the amplifiers or chips with the matching networks either for maximum gain or optimal noise figure.

In this chapter, the design of a rectangular waveguide amplifier integrated with planar circuits based on active coupling matrix synthesis (developed in Chapter 4) is demonstrated. A waveguide filter circuit is integrated with the matching network for the selected transistor by designing a quasi-waveguide resonator formed with the transistor circuit and a rectangular waveguide-to-microstrip transition. By this technique, the circuit losses can be minimised by removing the microstrip circuits conventionally used for impedance matching. The design process for amplifiers with filters as coupled resonator circuits presented in this chapter is applicable for THz

communication devices.

6.2 Integrated Waveguide Amplifiers

The literature review on bandpass filtering amplifier is presented in Chapter 5 which discusses several bandpass filtering circuits, and the literature review on sub-millimetre and THz waveguide amplifiers are given in Chapter 2. Here we review directly coupled transistor waveguide amplifiers of which there have been very few. However, Figure 6.1 shows a hypothetical substrate integrated waveguide (SIW) based microwave amplifier and a proposed amplifier embedded into the SIW as presented [3]. It has demonstrated an X-band amplifier of 10 dB gain and better than 10 dB of input and output return losses based on SIW. The design is presented for a single transistor with the input and output matching networks designed based on SIW in lieu of circuits on the planar MMIC. The input and output matching networks use SIW-based components instead of microstrip circuits, so that the overall size of the circuit with the matching networks can be reduced. The paper explains the design of the matching network using the standard design procedure and the DC-decoupled transition serves as a part of the matching structure. The transition is designed to stabilise the amplifier and suppress the power gain outside of the operating band. This work has proposed an approach for higher frequency devices. The loss of the SIW is lower than that of microstrip.

In this chapter, the rectangular waveguide filtering amplifier demonstrates a new integrated circuit approach for higher frequency applications using the coupling matrix synthesis method introduced in Chapter 4.

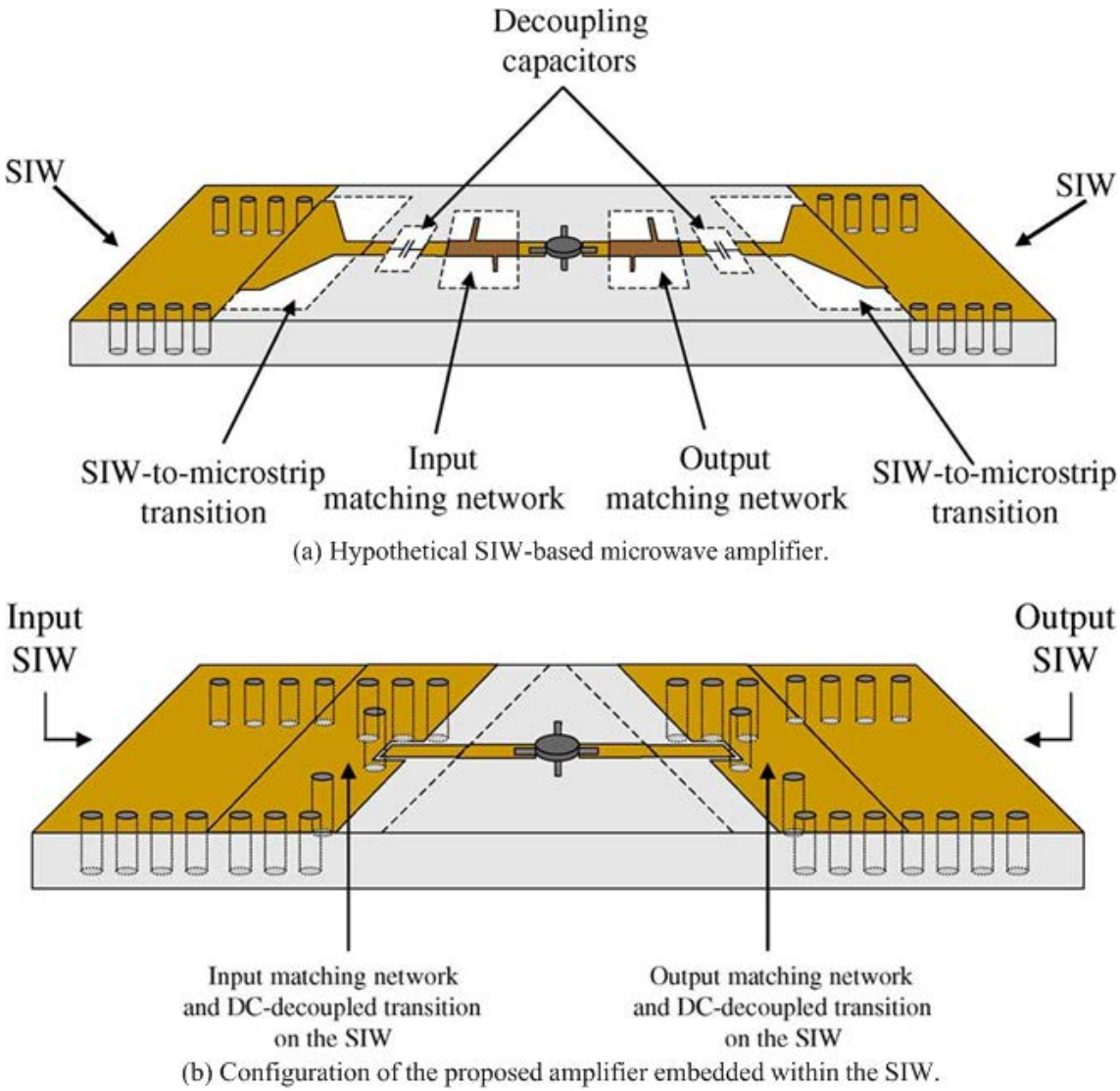

Figure 6.1: The X-band substrate integrated waveguide amplifier, taken from [3]

6.3 Waveguide Filtering Amplifier Coupling Matrix Synthesis

The overall topology for the integrated waveguide filtering amplifier is shown in Figure 6.2. This reflects the topology introduced in Section 4.6 where a transistor is incorporated with the last resonator. The source and load nodes are denoted as white circles and the three resonators are denoted in black circles. The $\triangleright$ indicate the transistor amplifier component. The dotted line between adjacent resonators represent the inter-resonator coupling.

In this implementation, there are three resonators based on rectangular waveguide structures. The first two resonators are conventional waveguide iris resonators and the conventional synthesis and design approach can apply. The transistor is incorporated within the last quasi-waveguide resonator with its input circuit via a waveguide to microstrip transition.

The general coupling matrix descriptions are introduced in Section 4.6 and this section will discuss the synthesis of the active coupling matrix.

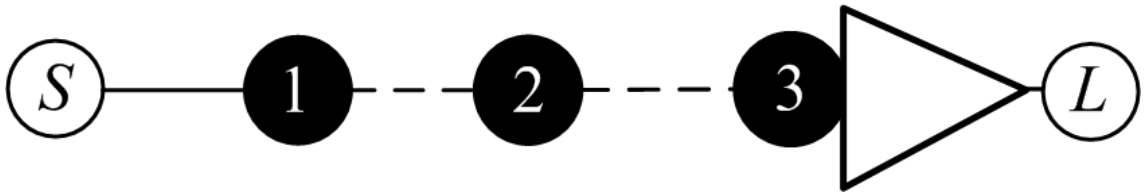

Figure 6.2: The topology for the waveguide filtering amplifier circuit

This example of a filtering amplifier has a specification with the centre frequency of 9.1 GHz, bandwidth of 400 MHz, and third order Chebyshev filtering characteristics.

The coupling matrix description according to Section 4.6, Chapter 4 for the waveguide amplifier is given below. The filtering characteristics of the third order filtering amplifier is assumed to be a synchronously tuned Chebyshev filter for simplicity, and the general coupling matrix for the filter specification can be found by the method described in Chapter 4. It is a third order Chebyshev filter which means $n = 3$. The fractional bandwidth $FBW = 0.044$ with the centre

frequency f_0 = 9.1 GHz. According to conventional table and formulas in [125], the g values for its lowpass prototype Chebyshev filter is tabulated in Table 6.1 for the specification of 20 dB return loss S_{11} in the pass band.

g_0	g_1	g_2	g_3	g_4
1	0.8516	1.1032	0.8516	1

Table 6.1: Element values for Chebyshev Lowpass Prototype, third order, -20 dB S_{11} in pass-band.

From Chapter 4, the overall general circuit matrix $[A]$ to describe the third order filtering amplifier example consists of four separate sub-matrices $[q]$, $[U]$, $[m]$ and $[T]$ as,

$$[A] = [q] + p[U] - j[m] + [T] \tag{6.3.1}$$

The full representation for those matrices are generated with the same procedures as stated in Chapter 5. Those values for each matrix elements are given below.

The scaled external quality factor matrix $[q]$ for the third order filtering amplifier is from Equation 4.6.16

$$[q] = \begin{bmatrix} 1.1743 & 0 & 0 & 0 \\ 0 & 0 & 0 & 0 \\ 0 & 0 & 1.1743 & 0 \\ 0 & 0 & 0 & 1.1743 \end{bmatrix} \tag{6.3.2}$$

The full details for matrix $[U]$ is

$$[U] = \begin{bmatrix} 1 & 0 & 0 & 0 \\ 0 & 1 & 0 & 0 \\ 0 & 0 & 1 & 0 \\ 0 & 0 & 0 & 0 \end{bmatrix} \tag{6.3.3}$$

The general normalised coupling matrix [m] is expressed from Equation 4.6.19 as

$$[m] = \begin{bmatrix} 0 & 1.0317 & 0 & 0 \\ 1.0317 & 0 & 1.0317 & 0 \\ 0 & 1.0317 & 0 & 0.0469 \\ 0 & 0 & 0.0469 & 0 \end{bmatrix} \tag{6.3.4}$$

The transistor matrix [T] is consist of two main elements, and their numerical values for $T_{gm} = 4.6970$ and $T_{gd} = 0.3670$ using the same calculations described in Chapter 5 for transistor NE3210S01 [170].

The numerical representation for the transistor matrix [T] is shown as

$$[T] = \begin{bmatrix} 0 & 0 & 0 & 0 \\ 0 & 0 & 0 & 0 \\ 0 & 0 & 0 & 0 \\ 0 & 0 & 4.6970 & 0.3670 \end{bmatrix} \tag{6.3.5}$$

The calculated theoretical results by those matrix Equations (6.3.2)-(6.3.5) for the filtering amplifier is shown in Figure 6.3 with Equation 4.8.6 to generate the its corresponding S-parameters. It can be seen that the best return loss in the pass band is not at 20 dB though 3 poles can be clearly observed. To recover the conventional Chebyshev filter characteristics, further coupling matrix adjustments are implemented by introducing self-coupling coefficients m_{11}, m_{22} and m_{33} into general normalised coupling matrix [m].

$$[m] = \begin{bmatrix} m_{11} & m_{12} & 0 & 0 \\ m_{21} & m_{22} & m_{23} & 0 \\ 0 & m_{32} & m_{33} & m_{gd} \\ 0 & 0 & m_{gd} & 0 \end{bmatrix} \tag{6.3.6}$$

Matrix adjustments are done with mathematical optimisation for goals at flatness and maximum return loss S_{11} for the pass band 400 MHz at centre frequency 9.1 GHz while keeping the inter-resonator couplings unchanged. The resultant normalised coupling matrix with self coupling coefficients is

$$[m] = \begin{bmatrix} 0.02 & 1.0317 & 0 & 0 \\ 1.0317 & -0.04 & 1.0317 & 0 \\ 0 & 1.0317 & 0.03 & 0.0469 \\ 0 & 0 & 0.0469 & 0 \end{bmatrix} \tag{6.3.7}$$

The plotted frequency response from this circuit matrix is shown in Figure 6.3 with the new normalised coupling matrix Equation (6.3.7). With the matrix adjustments, S_{11} can show the maximum -20 dB level with 3 poles.

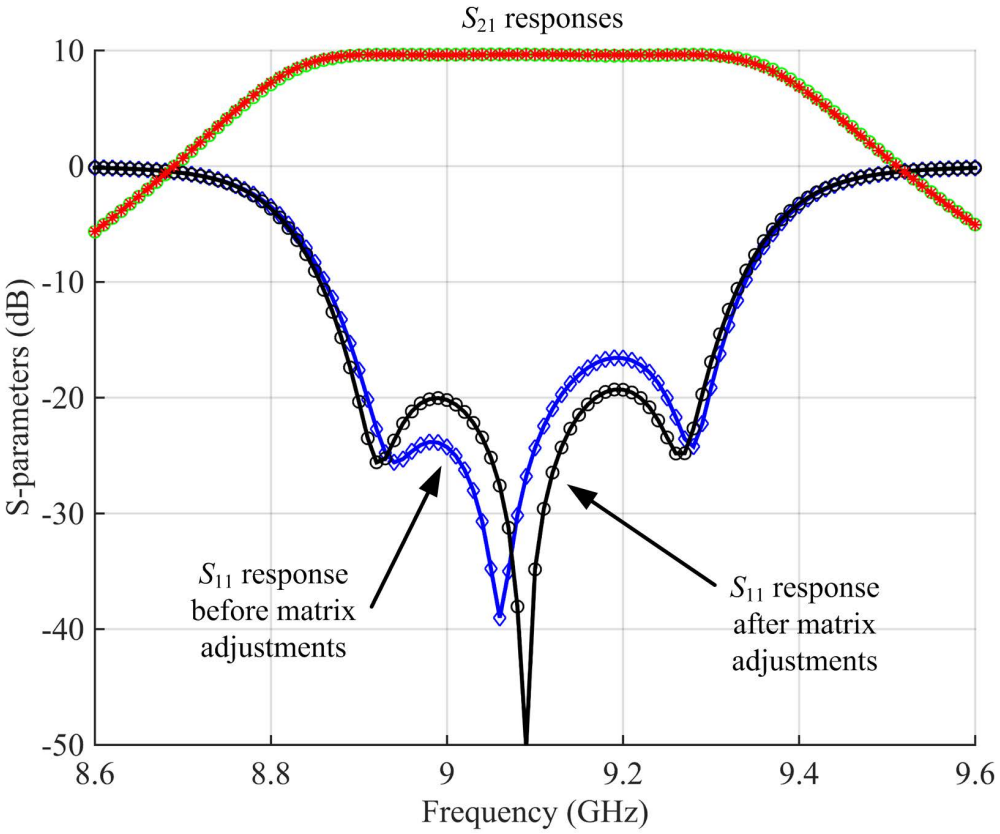

Figure 6.3: Theoretical calculation results for a third order Chebyshev filtering amplifier

6.4 Waveguide Amplifier Coupling Matrix Design Process

In this section, detailed design procedures are given based on extracting the desired external quality factors and coupling coefficients with the computer aided design software packages (e.g., CST [124], ADS [171]). The filtering amplifier is designed based on the X-band rectangular waveguide with the standard aperture size 22.86 mm × 10.16 mm. For this design, three waveguide resonators are presented and they require 2 external quality factors (e.g. Q_{eS} and Q_{eT}) and 4 coupling coefficients (M_{12}, M_{23}, M_{21} and M_{32}) to be extracted from the quality factor matrix $[Q]$ and coupling matrix $[M]$.

In terms of the design procedures, special treatments are required for the asynchronously tuned resonators where $m_{ii} \neq 0$, which means that each resonator can resonate at another frequency rather than the centre frequency f_c. In this case, the centre frequency of the filter is 9.1 GHz and the centre frequency of the resonators can be found with Equation (5.5.11) as f_{11} = 9.102 GHz, f_{22} = 9.094 GHz and f_{33} = 9.104 GHz respectively from m_{11}, m_{22} and m_{33}. As those self resonating frequencies f_{11}, f_{22} and f_{33} are so close to the centre frequency f_c that in this case they will be taken be the resonating frequency at 9.1 GHz for simplicity during the physical design process.

In this waveguide filtering amplifier it is assumed that $m_{21} = m_{32}$ as shown in coupling matrix $[m]$ in Equation (6.3.7). First of all, the normalised coupling matrix $[m]$ and the scaled quality factor matrix $[q]$ are transformed into coupling matrix $[M]$ and quality factor matrix $[Q]$ for the device.

The coupling matrix $[M]$ is found from Equation (6.3.7) as,

$$[M] = \begin{bmatrix} 0.0008 & 0.04535 & 0 & 0 \\ 0.04535 & -0.0016 & 0.04535 & 0 \\ 0 & 0.04535 & 0.0012 & 0.0025 \\ 0 & 0 & 0.0025 & 0 \end{bmatrix} \tag{6.4.1}$$

The quality factor matrix $[Q]$ is found from Equation (6.3.2) as

$$[Q] = \begin{bmatrix} 19.3735 & 0 & 0 & 0 \\ 0 & 0 & 0 & 0 \\ 0 & 0 & 19.3735 & 0 \\ 0 & 0 & 0 & 19.3735 \end{bmatrix} \tag{6.4.2}$$

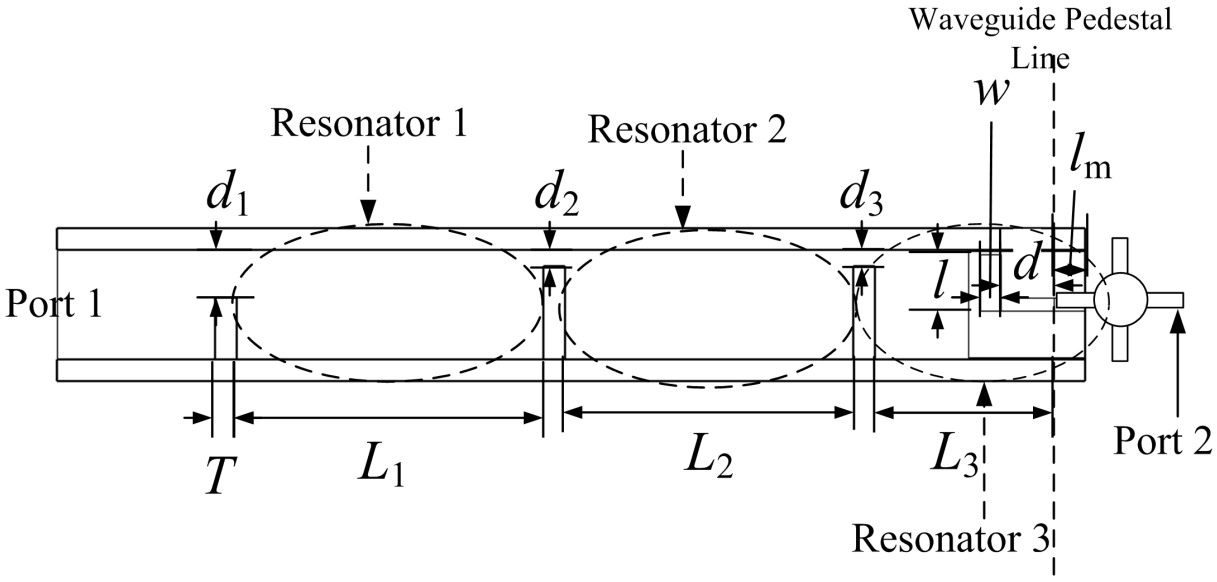

Figure 6.4: The equivalent layout for the waveguide filtering amplifier resonators incorporated with a transistor.

It is informative to illustrate the completed waveguide components as shown in Figure 6.4 before discussing the design procedures.

Three resonators are required to demonstrate the third order filter, the resonator lengths are L_1, L_2 and L_3 as shown in Figure 6.4. The iris aperture size d_1 determines the external quality factor Q_{eS}. The transition dimensions such as the transition antenna length l, transition feedline d and transition width w and microstrip interconnection length l_m determine the external quality factor Q_{eT} for the second integrated resonator. The iris aperture size d_2 and d_3 determine the inter-resonator couplings between resonators, e.g., M_{21} and M_{32}. According to the symmetry of the filter which gives that the same coupling coefficients $M_{32} = M_{21}$, thus the iris aperture size

$d_3 = d_2$. The iris thickness is fixed as $T = 2$ mm [103]. The detailed design process for physical realisation for the waveguide amplifier is given from Session 6.4.1 to Session 6.4.3.

6.4.1 Extraction the external quality factor for Resonator 1

The practical approach on extraction external quality factor for the first resonator is presented as follows [125].

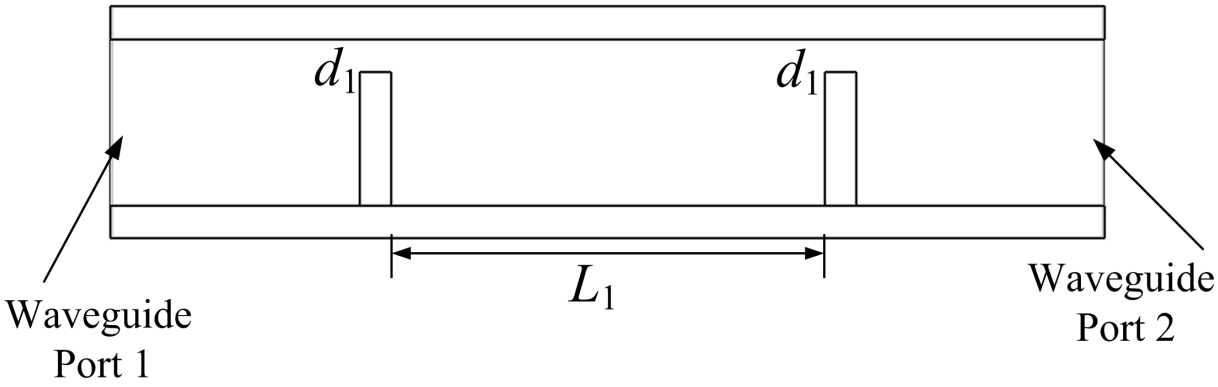

Figure 6.5: The waveguide structure to extract the external quality factor.

The EM simulation configuration is shown in Figure 6.5. The dimension d_1 for the waveguide resonator iris height determines the value of the external quality factor Q_{eS}. The resonator length L_1 determines the centre frequency f_0.

The simulation results of the waveguide resonator structure as shown in Figure 6.5 is illustrated in Figure 6.6 (a). There is a peak in the S_{21} in dB at the resonating frequency 9.1 GHz. By changing the iris aperture size d_1, the external quality factor Q_{eS} can be tuned under the same resonating frequency by slightly changing L_1. Figure 6.6 (b) shows relationship between the external quality factor Q_{eS} against the physical iris size d_1. The value for d_1 is read off from the figure as $d_1 = 3.8$ mm with $L_1 = 27.3$ mm for $Q_{eS} = 19.3$ as in Equation 6.4.2.

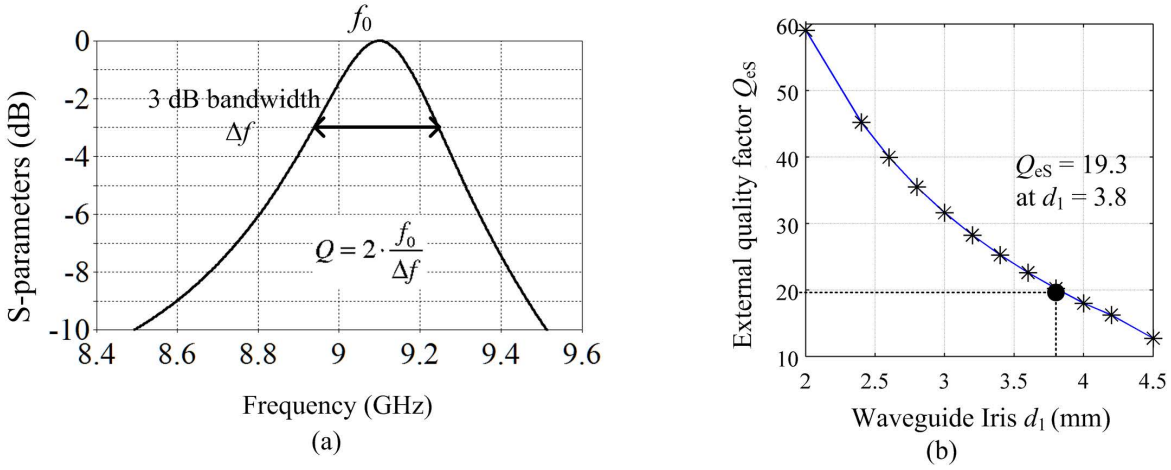

Figure 6.6: (a) The simulation results of the waveguide structure extracting the external quality factor Q_{eS}. (b) The relationship of Q_{eS} versus waveguide iris dimension d_1.

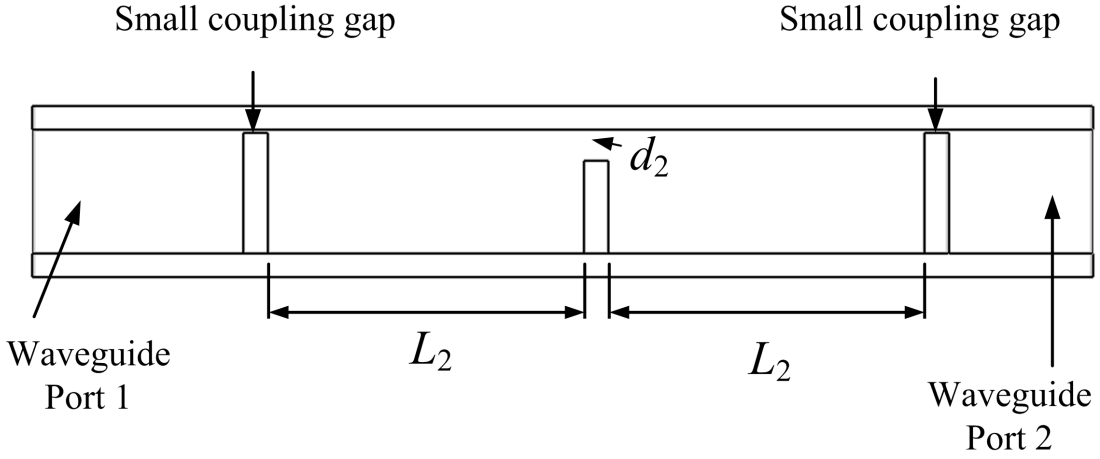

Figure 6.7: The waveguide structure to extract the coupling coefficient.

6.4.2 Extraction of the coupling coefficient for Resonator 2

Figure 6.7 shows the waveguide structure to extract the coupling coefficient with two identical waveguide resonators both with the same resonator length of L_2 and the middle resonator iris d_2. The resonators are weakly coupled into the external waveguide by two small coupling gaps. The iris size d_2 determines the value of the coupling coefficient [103]. The simulation results of the waveguide structure are shown in Figure 6.8 (a) with two peaks as f_1 and f_1. The coupling

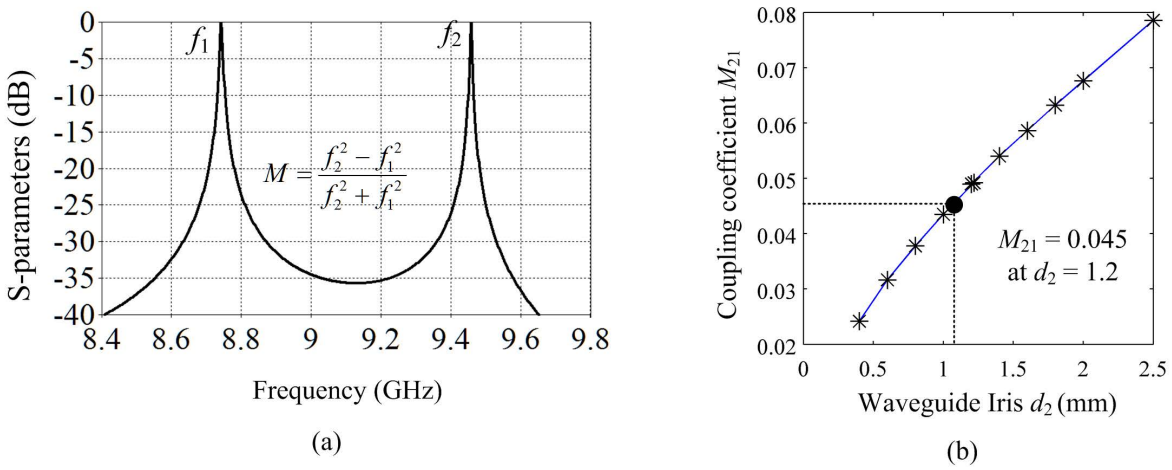

Figure 6.8: (a) The simulation results of the waveguide structure extracting the coupling coefficient. (b) The relationship of M versus waveguide iris dimension d_2.

coefficient M can be found via the equation given in the figure. Changing the iris size d_2 can give different coupling coefficient M, with the resonator length L_2 controlling the resonating frequency. Figure 6.8 (b) gives the relationship between the coupling coefficient M against the iris d_2. The required iris size is $d_2 = 1.2$ mm read from the figure and $d_3 = d_2$ with $L_3 = L_2 = 26.2$ mm.

6.4.3 Extraction of the external quality factor for Resonator 3

Here we consider the design process for Resonator 3 which is an integrated resonator with quasi-waveguide structure with the transistor.

Figure 6.9 (a) shows the simulation configuration for the waveguide transistor resonator. Two external ports in the square boxes are the terminations for the cascaded waveguide structure model and the transistor file data model for NE3210S01 [170]. It enables circuit simulation of the waveguide structure with the transistor.

Figure 6.9 (b) shows the resonator structure which is the transition model in Figure 6.9 (a). One port is the waveguide port, and the other port is the microstrip port connected to a transistor. The CST model stops at the dotted line. The microstrip circuit is the double-sided dipole antenna

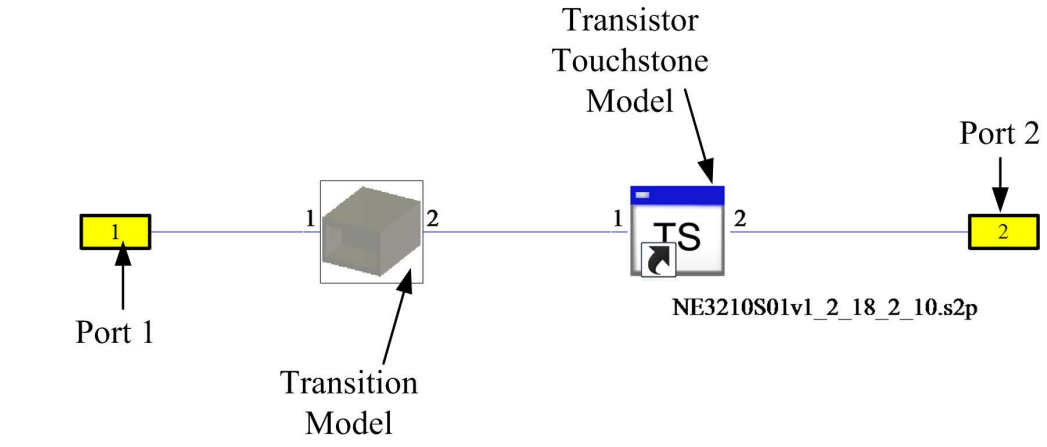

(a)

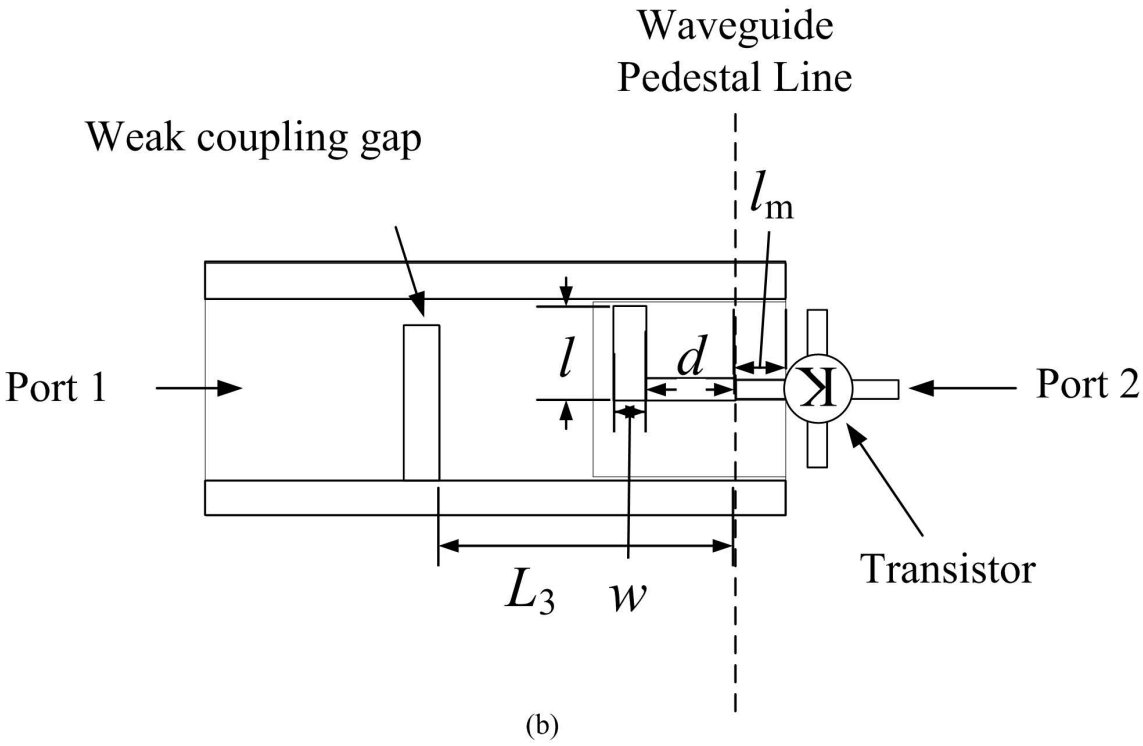

(b)

Figure 6.9: (a) The configurations in CST DS for co-simulation for the waveguide structure with transistor dataset. (b) The equivalent simulation artwork for the waveguide co-simulation with transition with dimensional annotations

transition to coupling the waves from the waveguide [174]. The waveguide iris is a small gap adjacent to the top waveguide wall so that weak coupling is formed at the iris. The resonator length L_3 controls the resonating centre frequency. The structures for transitions such as antenna

feedline d, antenna width w, antenna length l and microsttrip interconnection l_m can change the external quality factor Q_{eT}. The transition can degrade the overall amplifier noise performance due to its ohmic loss.

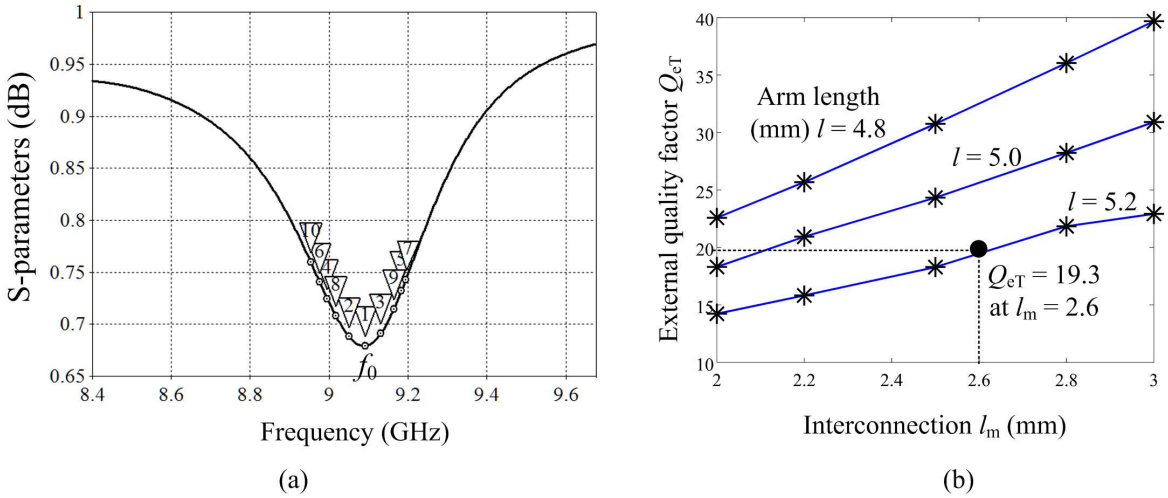

Figure 6.10: (a) Simulation result S_{11} of the waveguide structure with the transistor. (b) The Q_{eT} versus the interconnection l_m.

Figure 6.10 (a) shows the simulated result (S_{11} in dB) of the co-simulation of the 3D structure with the transistor, and the Q_{eT} is calculated using this one port measurement of the reflection coefficient S_{11} magnitude [173]. The details to extract the external quality factor using the one port reflection method is given in Appendix A.

Figure 6.10 (b) shows the relationship of external quality factor Q_{eT} against the microstrip interconnection length l_m with three different antenna length l. The dimension l_m = 2.79 mm for the required Q_{eT} can be read off from Figure 6.10 (b) with L_3 = 16.23 mm, w = 1.87 mm, d = 4.96 mm, l = 5.26 mm.

6.5 Waveguide Amplifier Simulated Design with a Transistor

Once the dimensions for the waveguide amplifier are determined according to the desired external quality factor Q and coupling matrix M, the waveguide amplifier is constructed.

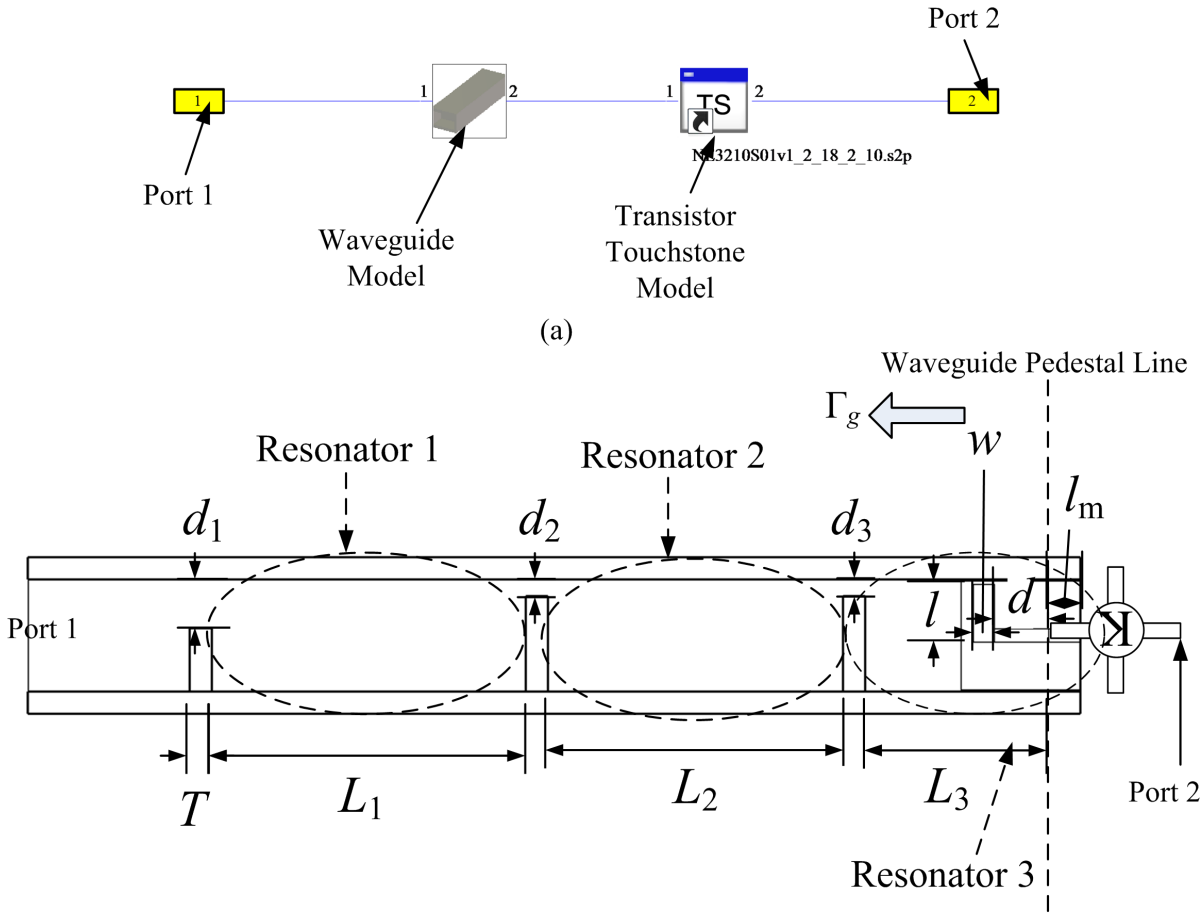

Figure 6.11: (a) The configurations in CST for the waveguide structure with the transistor dataset. (b) The equivalent layout for the waveguide co-simulation with transistor.

Figure 6.11 (a) illustrates the simulation schematic with two external ports, where the transistor NE3210S01 [170] is presented as a dataset, and the waveguide structure is presented as a waveguide model. Using this configuration, the simulated results from the waveguide structure is connected with the transistor dataset by the shared microstrip transmission line.

Figure 6.11 (b) show the waveguide amplifier equivalent layout. Two rectangular waveguide iris

resonators are modelled and they are named as Resonator 1 and Resonator 2. The third resonator is the integrated one via the transition with a transistor included, which is named Resonator 3. Dimensions for the waveguide structure are obtained from the previous Section 6.4.1 to Section 6.4.3.

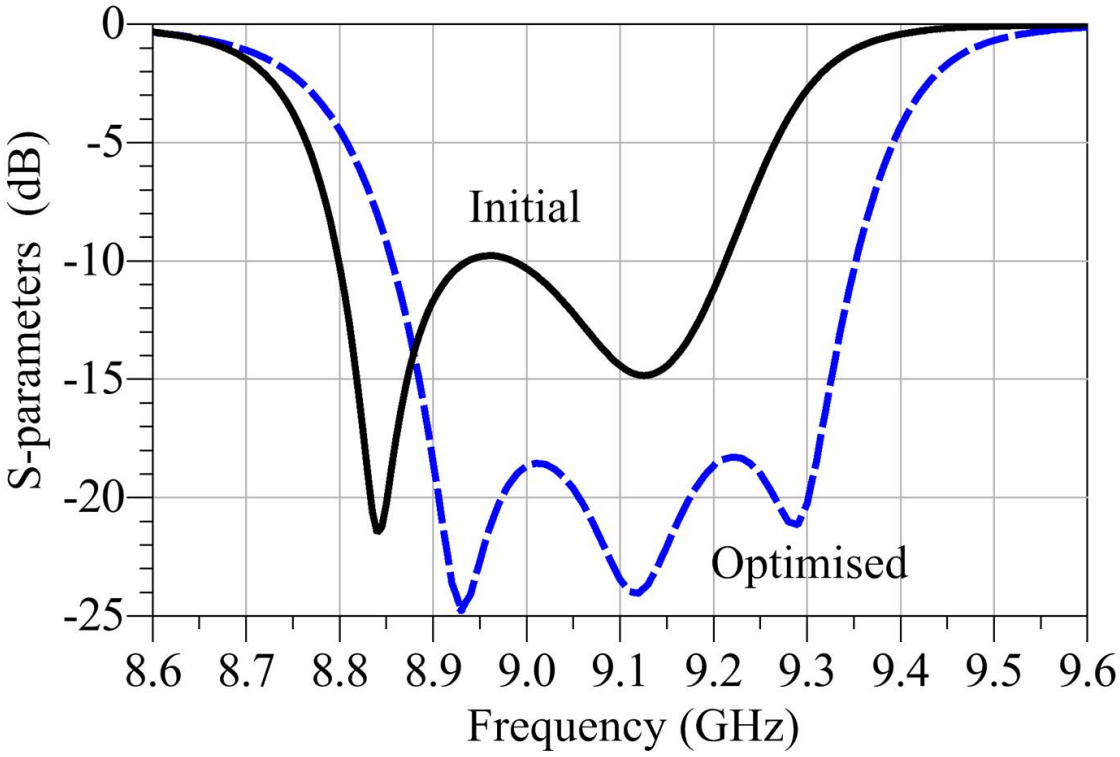

Figure 6.12: Simulation return loss for the waveguide amplifier.

The waveguide amplifier is simulated and optimized in CST with the target for the -20 dB S_{11} for the passband from 8.9 GHz to 9.3 GHz. Figure 6.12 shows the simulated and optimised return loss for the waveguide amplifier using the simulation setup in Figure 6.11 (a).

After the optimisation, the critical circuit dimensions indicated in Figure 6.11 (b) are given in mm as $d_1 = 4.40$, $d_2 = 1.54$, $d_3 = 1.54$, $L_1 = 28.30$, $L_2 = 26.68$, $L_3 = 16.59$, $w = 1.87$, $d = 4.96$, $l = 5.26$, $l_m = 2.79$.

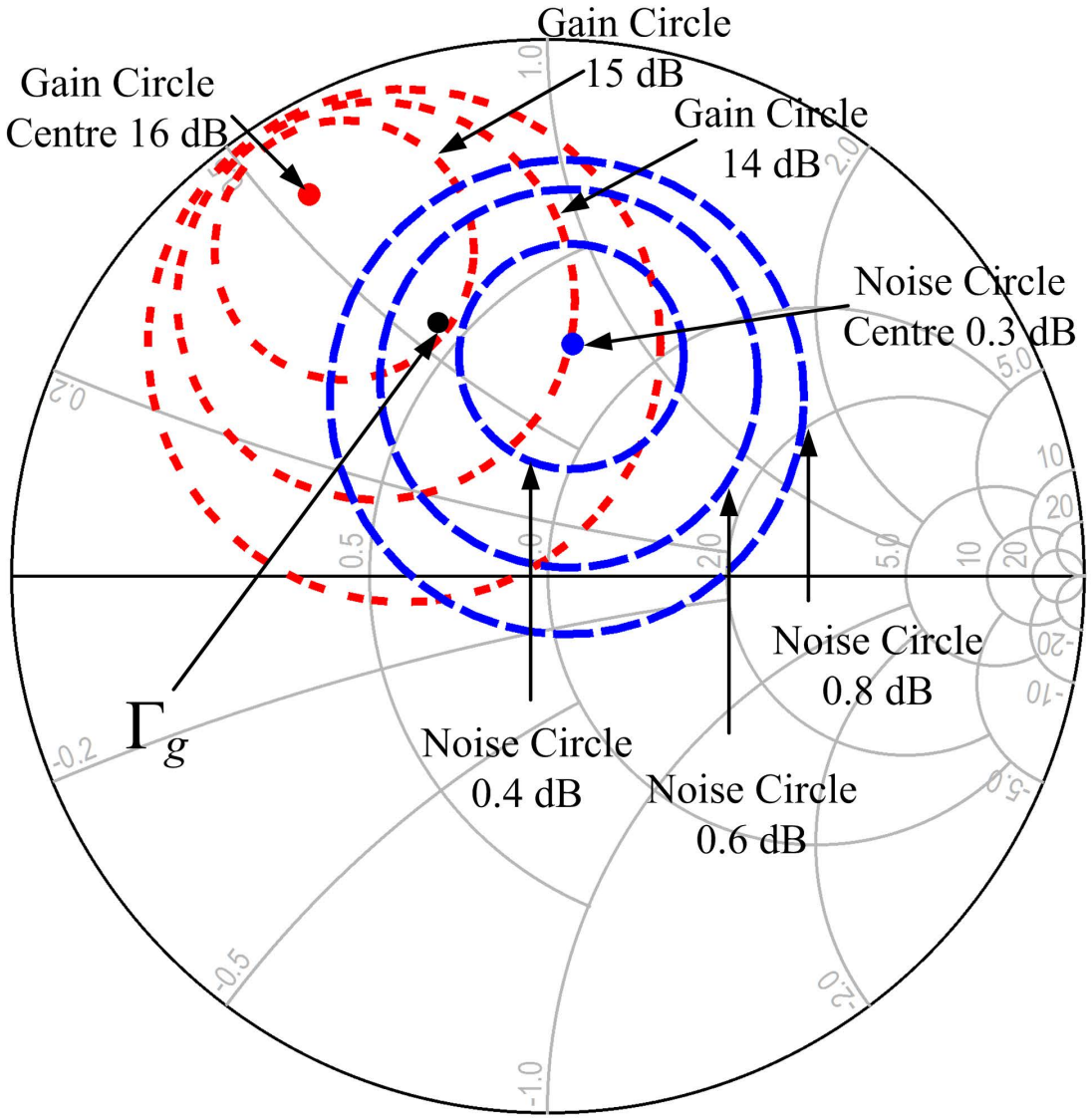

Figure 6.13: Smith Chart: the plots of amplifier noise and gain circles

Figure 6.13 shows the simulated reflection coefficient Γ_g corresponds to the impedance seen into the input matching circuit from the gate terminal at the centre frequency 9.1 GHz. This response is plotted with the constant available gain and noise circles calculated from the measured S-parameters and noise parameters for the transistor provided by the manufacturer at 9.1 GHz. In this design, the input matching by the coupling matrix synthesis can meet a good tradeoff for both the gain and the noise performance.

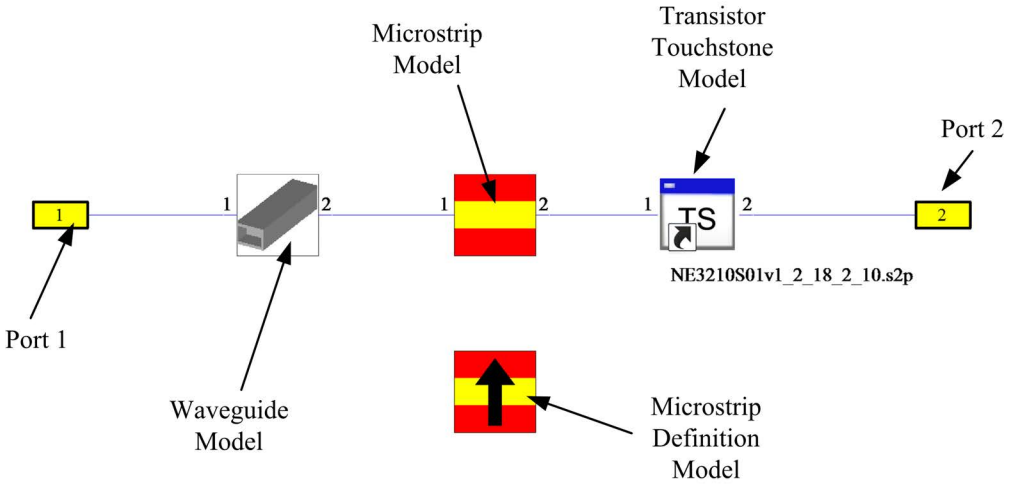

Figure 6.14: Simulation environment in CST with microstrip line for de-embedded waveguide model.

As it is not easy and fast to design the microstrip circuit with a transistor in CST, ADS is used for the microstrip circuit design and complete waveguide amplifier simulation. In order to design the microstrip circuit using ADS, a starting piece of microstrip circuit is needed to connect the designs. Figure 6.14 shows the CST co-simulation environment. At Port 2 in Figure 6.11 (b), the microstrip port is de-embeded with a length of 2.8 mm from the microstrip transmission lines which is the same length for the microstrip interconnection length l_m. By this method, the phase and magnitude information of the microstrip is de-embedded backwards. As long as the cascaded simulations components share the same field and transmission modes, the design could apply the cascading components simulation approach according to [124]. The electric fields of the de-embedded microstrip lines agree with the microstrip Q-TEM mode by verifying the simulation port mode in CST. They share the same transmission mode with the simple CST planar microstrip model, thus cascading components method is valid. After the simulation de-embedded plane is referenced backward from the original microstrip port, an additional piece of microstrip line with the same length l_m is added which verifies the design method of cascading simulation components. The rest of the microstrip circuit can built with the starting microstrip length of the de-embedded piece of microstip interconnection l_m.

6.6 Microstrip Circuit for Waveguide Filtering Amplifier

The planar microstrip circuit is modelled in ADS design environment with the design starting from the de-embedded microstrip interconnection length l_m. The whole microstrip circuit fits into the waveguide height without touching the waveguide wall.

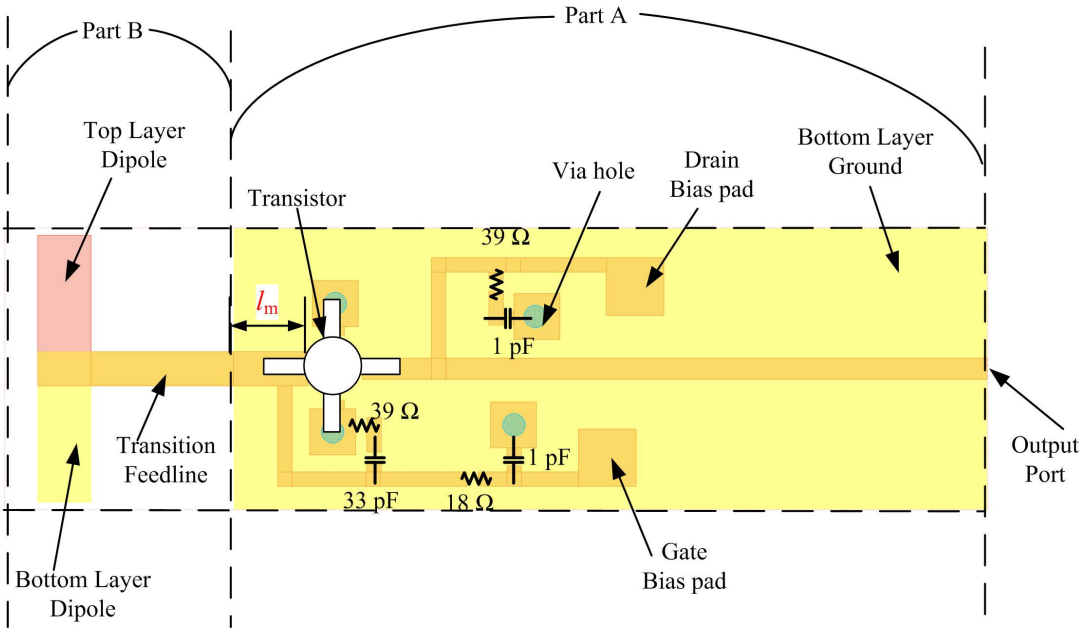

Figure 6.15: Circuit layout for the microstrip circuit for waveguide amplifier

Figure 6.15 shows the microstrip circuit for the waveguide filtering amplifier. In this design, the microstrip width is 9.8 mm which is narrower than the standard X band rectangular waveguide height. This circuit is divided into two circuit parts: Part A is for the amplifier bias circuitry, and Part B is waveguide to microstrip transition. Part B is identical to the transition model in waveguide model discussed in Session 6.4.3. The microstrip circuit for Part B has two sides which are indicated in different colours. The two arms for the dipole antenna are patterned on the top and bottom layers separately on Part B of the circuit. The transistor NE3210S01 [170] is mounted onto the microstip mounting pads and the DC bias lines are designed to fit into the whole waveguide width. The input part of the microstrip circuit is the rectangular waveguide-

to-microstrip transition which is identical to Figure 6.11. The output of the microstrip circuit is connected with a SMA connector through a 50 Ω microstrip output for measurement. In terms of the planar microstrip circuit, 0402 size SMD components including capacitors, resistors and the transistor are used. The resistors, capacitors on the bias lines can degrade the overall noise performance.

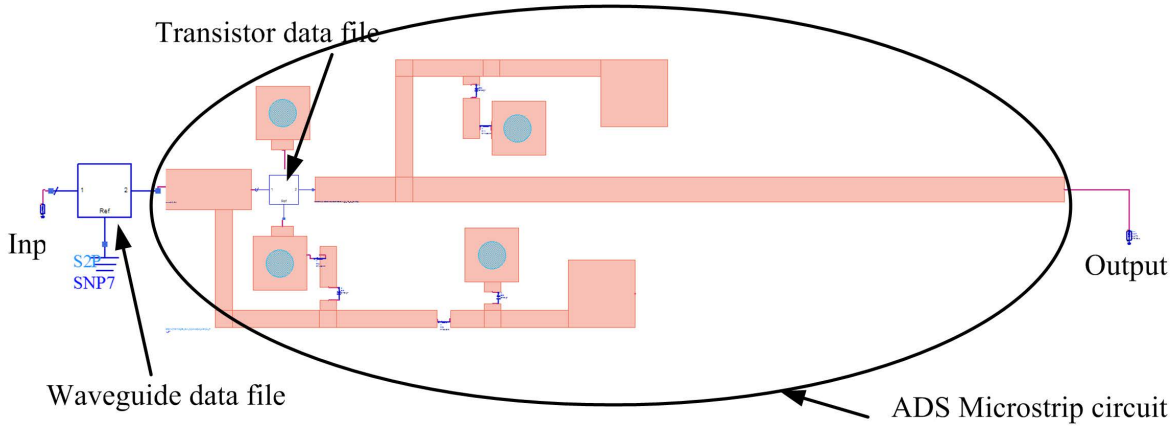

Figure 6.16: Simulation configuration for the complete waveguide amplifier.

Figure 6.16 illustrates the ADS simulation configuration for the complete waveguide amplifier. The same waveguide structure simulated data file shown in Figure 6.14 is used in this simulation. The ADS microstrip circuit is modelled and simulated with the SMD components represented as lumped element models. The circuit for the waveguide to microstrip is included into the waveguide structure. This microstrip circuit follows the identical layout and SMD configurations given in Figure 6.15 for Part A.

Figure 6.17 shows the simulation results for the complete waveguide amplifier including the bias circuits. It shows 10 dB gain in S_{21} and clear 3 poles in S_{11} around -20 dB. It indicates that the circuit is unconditionally stable from 6 GHz to 10 GHz as the stability factor is larger than 1. The simulated result shows the achieved noise figure of 1.4 dB for the passband.

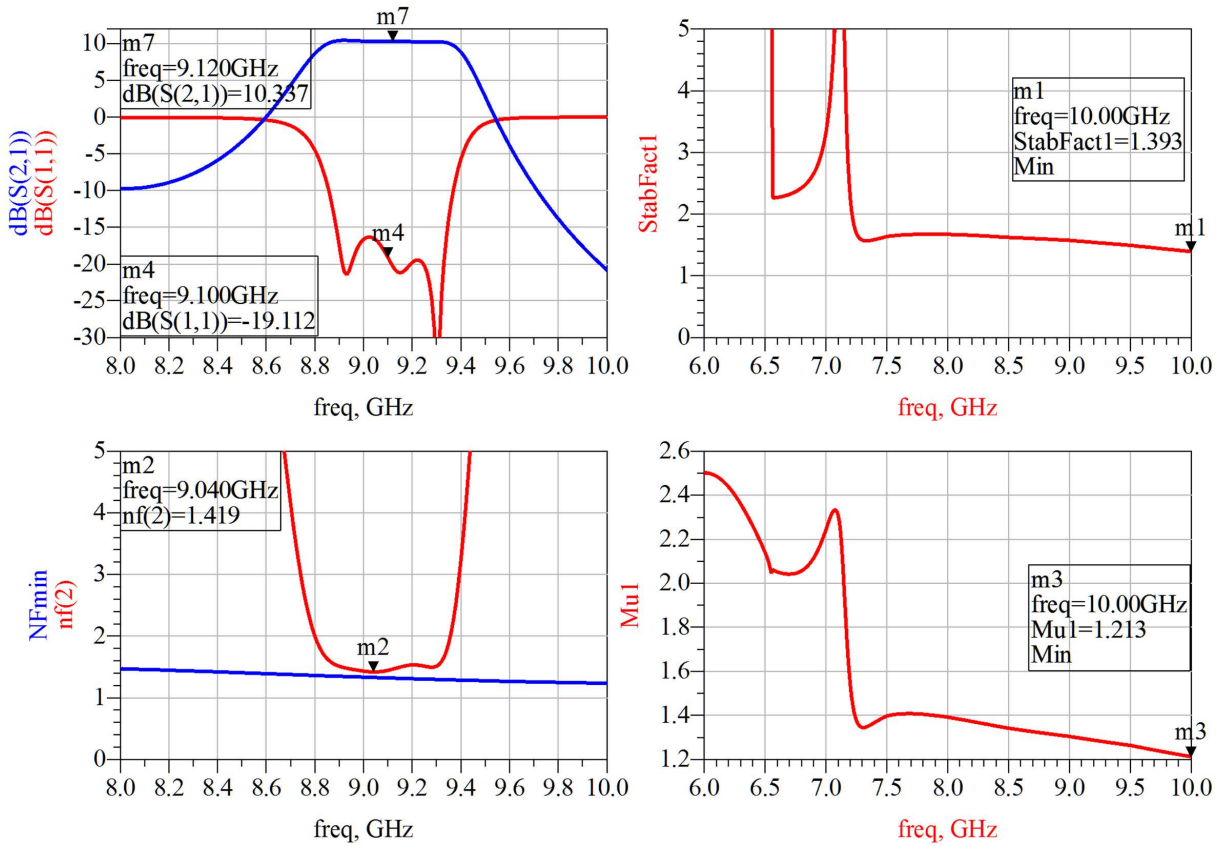

Figure 6.17: ADS simulation S-parameter results for the complete waveguide amplifier, noise figure in dB and stability factor.

Figure 6.18 provides the layout artwork and dimensional information of the microstrip circuit for the waveguide amplifier.

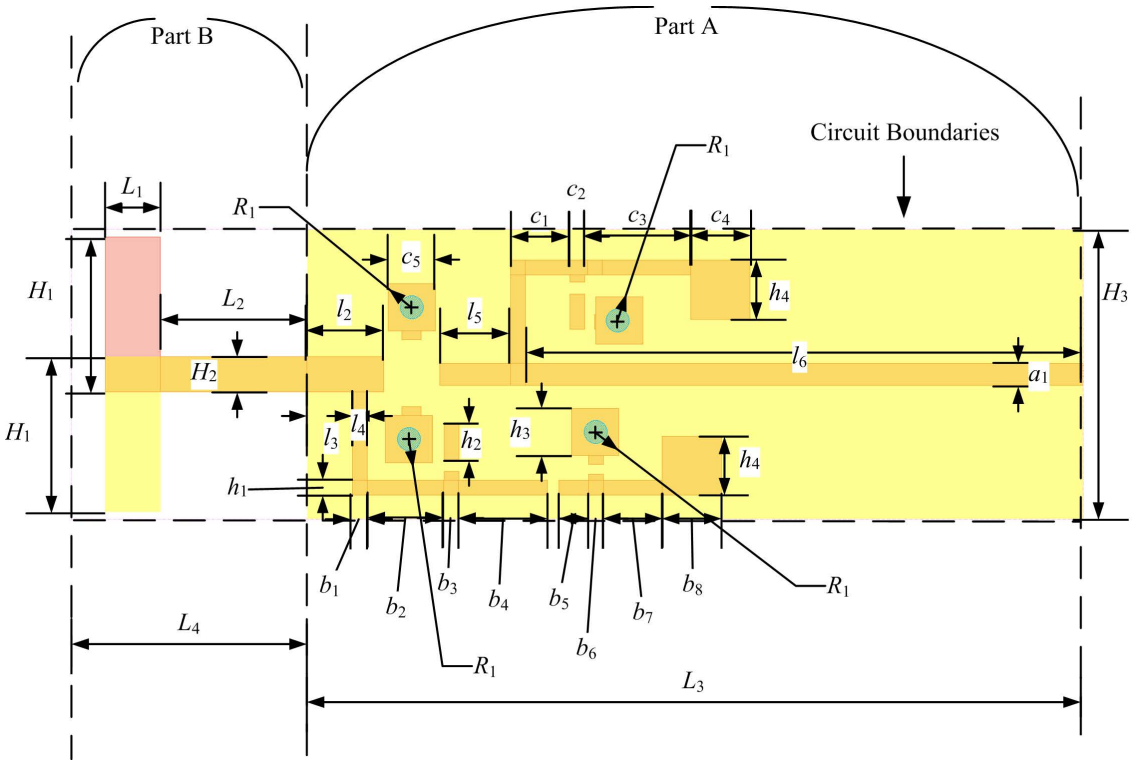

Figure 6.18: Circuit artwork for the microstrip circuit for waveguide amplifier.

The dimensions (in mm) for the microstrip circuit are: L_1 = 1.8706, L_2 = 4.9682, L_3 = 26.0, L_4 = 7.986, H_1 = 5.26, H_2 = 1.2, H_3 = 9.8226, a_1 = 0.74, a_2 = 1.2, b_1 = 0.5, b_2 = 2.6, b_3 = 0.5, b_4 = 3.0, b_5 = 1.0, b_6 = 0.5, b_7 = 2.0, b_8 = 2.0, c_1 = 2.0, c_2 = 0.5, c_3 = 3.6, c_4 = 2.0, h_1 = 0.5, h_2 = 1.2, h_3 = 1.6, h_4 = 2.0, l_1 = 6.1, l_2 = 2.6, l_3 = 1.5, l_4 = 0.5, l_5 = 2.4, l_6 = 18.5, L_3 = 26.0, R_1 = 0.2.

6.7 Waveguide Amplifier Fabrication

6.7.1 Waveguide metal blocks

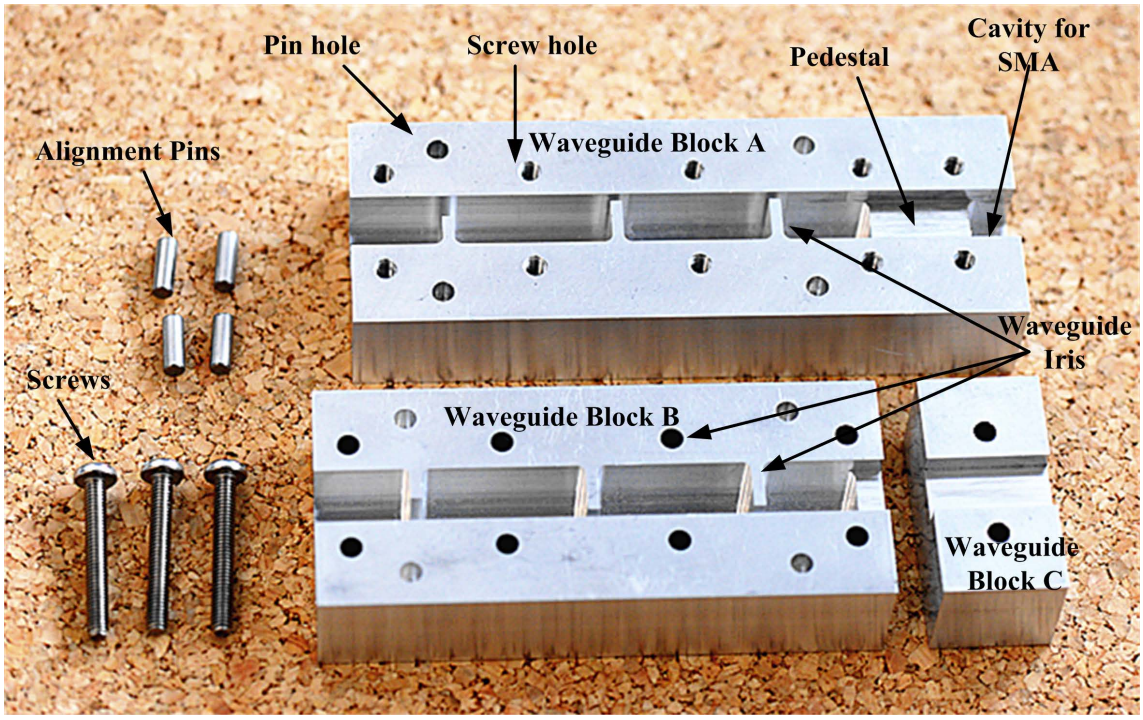

Figure 6.19: The photo of the machined waveguide structure.

Figure 6.19 shows the machined metal parts for waveguide in two halves cutting through the centre of the waveguide aperture long edge. The microstrip circuit is bonded onto the pedestal in Block A. A cavity at the output end is designed to accommodate an SMA connector. The waveguide structure is further separated into Blocks B and C. Mechanically, the waveguide structure is fabricated with three separate parts indicated as A, B and C. Additionally, holes for screws are drilled at the waveguide input port for measurement flange configurations.

6.7.2 Microstrip circuit for waveguide amplifier

Figure 6.20 displays a photo of the assembled microstrip circuit with top and bottom views of the waveguide amplifier with bias wires soldered. The circuit dimensions are 34.28 mm × 9.82 mm. At the left end, it is the waveguide to microstrip transition structure. The measurement

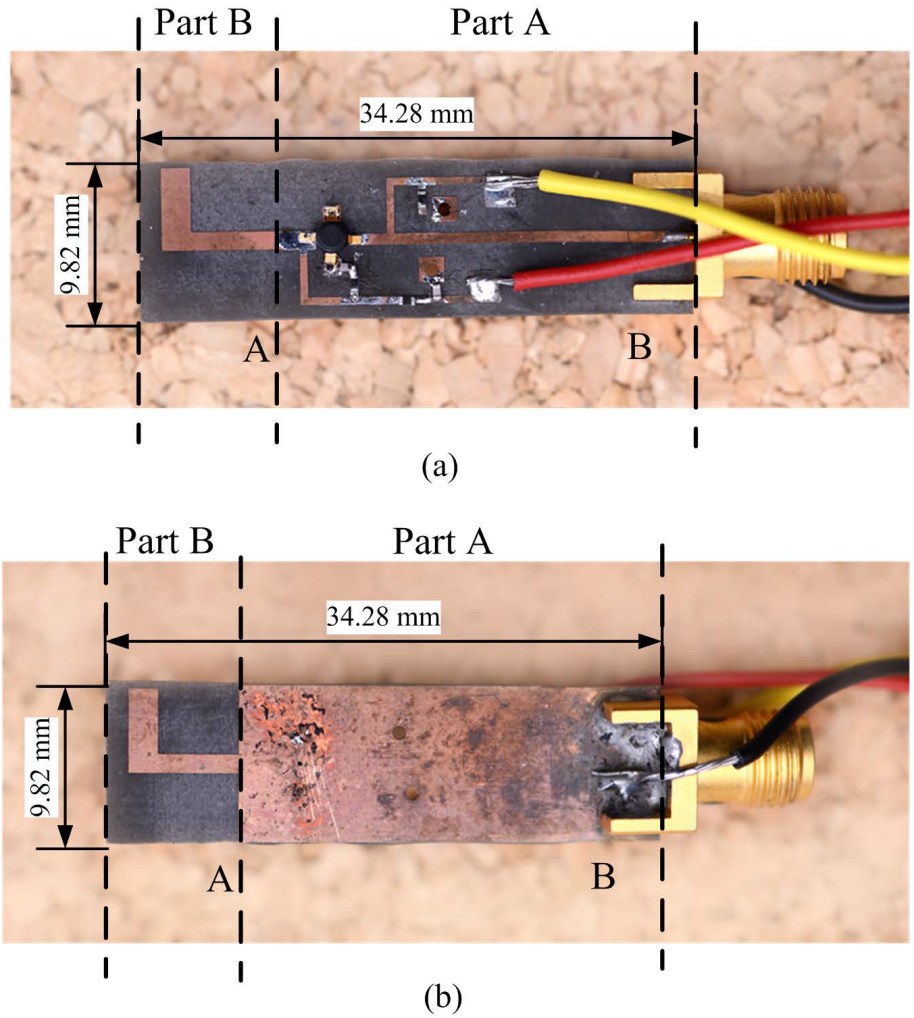

Figure 6.20: The photo of the fabricated microstrip circuit for waveguide amplifier (a) top view (b) bottom view.

output port is terminated with a SMA connector at the right end. The circuit Part A and Part B reflect two circuit parts in Figure 6.18. Part A circuit has been verified as unconditionally stable. The microstrip circuit is then bonded onto the waveguide Block A in Figure 6.19.

6.7.3 Waveguide amplifier assembly

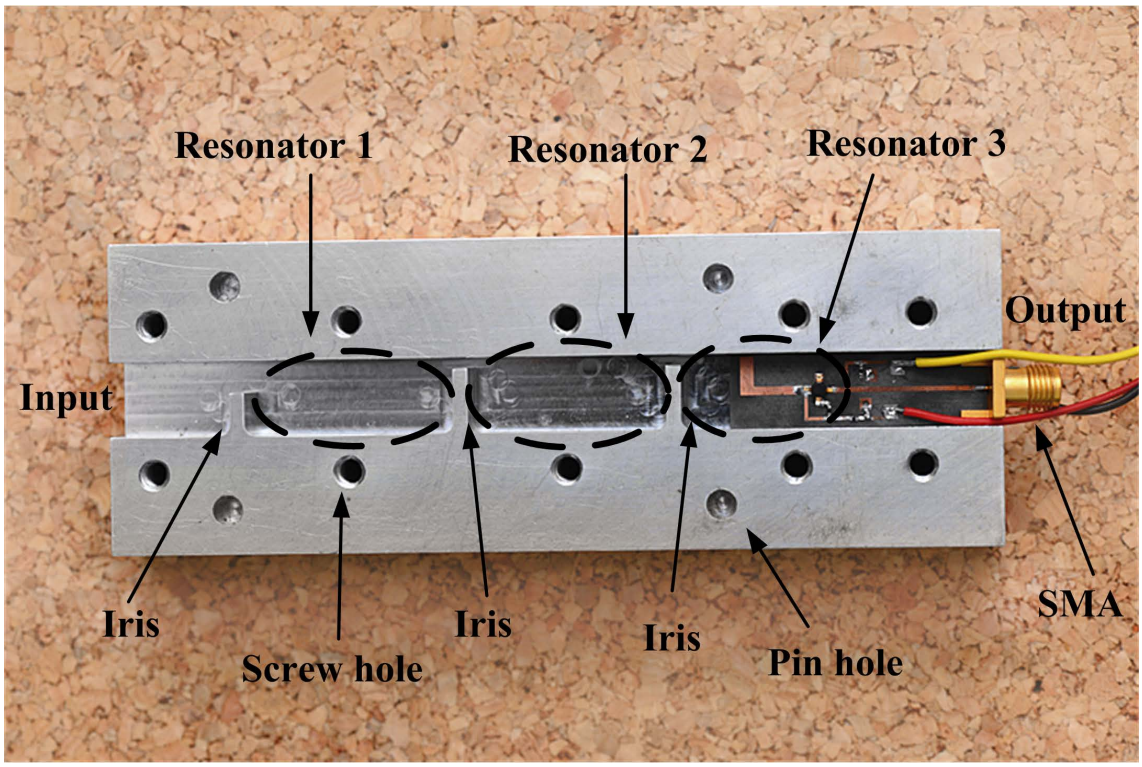

Figure 6.21: The photo of the fabricated microstrip circuit for waveguide amplifier.

Figure 6.21 shows the lower half of the assembled waveguide amplifier with the microstrip circuit bonded onto the waveguide pedestal. An SMA connector is soldered onto the microstrip circuit as well as the bias wires. The three resonators are clearly indicated in the figure.

6.8 Waveguide Amplifier Measurements and Discussions

In this section, the measurements for the waveguide filtering amplifier are presented. The measurement system is calibrated, and the device under test is illustrated in Figure 6.22.

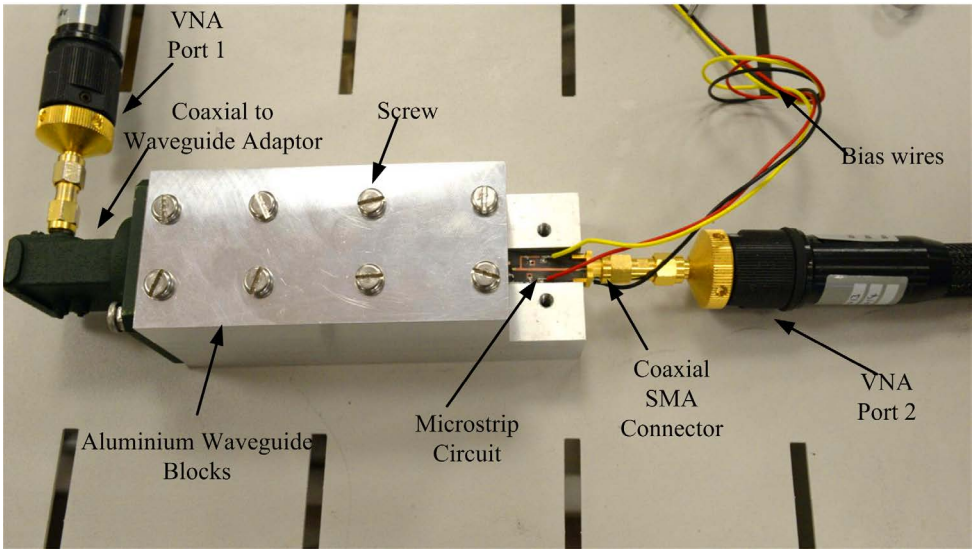

Figure 6.22: Device under test: the waveguide amplifier with two measurement ports

The measurement is carried with the Agilent vector network analyser PNA E8362B with two measurement ports. Measurement Port 1 is connected with a coaxial to waveguide adaptor and the adaptor is not calibrated. Connection to the waveguide input port (VNA Port 1) is tested using a WR-90 to coaxial transition with losses less than 0.1 dB by measurement verification. Port 2 is connected with the coaxial SMA connector. The waveguide metal Block C is removed as it offers flexibility for tuning the circuit. The electromagnetic waves from the waveguide input port can couple onto the microstrip circuit by the waveguide-to-microstrip transition without the microstrip circuit covered.

Figure 6.23 shows the measurement results as well as the simulation results from EM modelling software package and theoretical results from the active coupling matrix with a transistor for the waveguide amplifier. For the waveguide amplifier, the simulations results have the best S_{11} of -20 dB over the design bandwidth and have achieved over 10 dB gain. The measurement

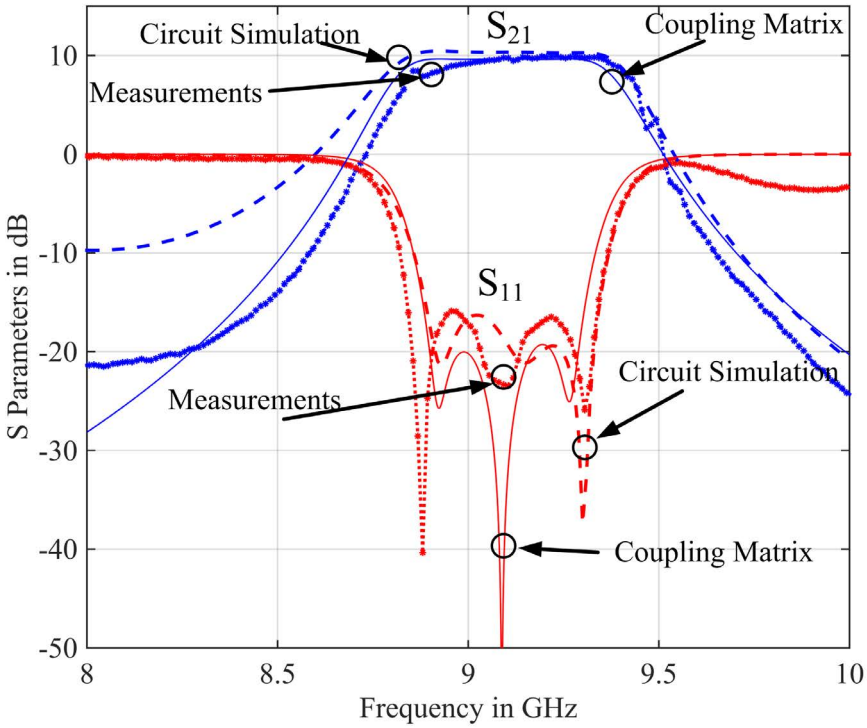

Figure 6.23: Measurement results of waveguide amplifier

results have return loss averaging around 18 dB and the gain from amplifier is 10 dB. Both the roughness of the waveguide cavity surface and poor contacts between the waveguide parts of the device lead to the additional insertion loss of the measured results [175]. The waveguide adaptor at the input port can give additional losses though which can be neglected as less than 0.1 dB. In summary, with the precision waveguide structure and assembled microstrip circuit, measurement results agree well with the EM simulation results and theoretical calculated responses in terms of the return loss levels and achieved gain.

6.9 Summary

The waveguide filtering amplifier is a demonstration at X band using the active coupling matrix in Chapter 6. The design process is a low frequency demonstration for the proposed THz amplifier circuits. It is specified as a third order Chebyshev filtering amplifier with the centre frequency 9.1 GHz and 400 MHz bandwidth. The description using the coupling matrix given in Chapter 4 is presented. In the design, there are three resonators constructed within the waveguide. Two of the resonators are conventional waveguide iris resonators and the other one is a quasi-waveguide resonator which integrates the transistor via a rectangular-waveguide to microstrip transition. The transistor is mounted onto the microstrip circuit which is bonded onto a supporting waveguide pedestal. The waveguide amplifier has been assembled and tested with a vector network analyser. The calculated S-parameter responses using the coupling matrix, EM simulated results and measurement results by vector analyser agree with each other. This waveguide amplifier has achieved 10 dB gain and 18 dB return loss in the passband. Paper [3] has presented similar integrated waveguide amplifier with similar 10 dB gain and this filtering amplifier is selective with the integrated waveguide filter. 18 dB return loss in this waveguide amplifier is better than that of 10 dB in [3]. This is a demonstration of the techniques to design a filter with amplification that is, an amplifier with frequency filtering features. The close correlation between the S-parameter response using the coupling matrix and the circuit measurement has validated the matrix description.

Chapter 7

Conclusions and Future Work

7.1 Conclusions

This conclusion summaries the core subjects that have been worked on which can be categorised into two main parts: (i) the circuits and systems for THz (300-10,000 GHz) wireless communications from Chapter 2 to Chapter 3; (ii) The coupling matrix method and its synthesis with design examples at X band (8-12 GHz) from Chapter 4 to Chapter 6.

For the first part of the thesis starting from Chapter 2, a THz wireless communication concept has been proposed which aimed to work at 300 GHz. The block diagram for the communication system is given which consists of basic communication system components such as filter, mixers, amplifiers and antennas for both transmission and receiver chains. Conventional sub-millimetre and THz communication electronics and systems have been reviewed, which are mostly based on individual components in CNC machined metal blocks with MMIC design for active circuitry. Additionally, various of micromachining techniques have been briefly reviewed for components and systems at THz frequency range. A micromachining technique based on SU-8 photoresist lithography technology has been introduced to accommodate the fabrication needs for low-cost and high precision THz components.

Additionally, a novel design concept for a waveguide amplifier for the THz communication

system is given in Chapter 2 along with the novel inherent matching and filtering technique proposed to minimise the system losses by removing the on-chip planar circuit matching for amplifiers or mixers into waveguide structures. The underlying principles of the inherent matching and filtering techniques are based on the fact that waveguides are superior to planar transmission lines (e.g. microstrips, coplanar waveguides, etc.) in terms of losses in the THz frequency range.

A WR-3 band (220-325 GHz) rectangular waveguide has been designed, fabricated and measured in Chapter 3 as the fundamental component for the THz wireless communication system. The rectangular waveguide is constructed with 5 layers and each layer is of the thickness 288 μm. Two rectangular waveguide devices of 15.95 mm long with novel bends have been designed with CST and then fabricated using the SU-8 micromachining technology, Later, they have been measured with a VNA. The measured losses for the rectangular waveguides have achieved the best average insertion loss at 0.031 dB/mm, which is very comparable to CNC machined waveguide at the same operating frequency with the insertion loss of 0.02 dB/mm. Chapter 3 has demonstrated that micromachined THz circuits using SU-8 micromachining technology can offer low loss solutions for THz components and systems.

The second part of the thesis is for the novel theoretical synthesis method with physical examples. The well documented coupling matrix based on coupled resonator circuits for microwave filters [125] has been presented with one simple synthesis method based on Chebyshev lowpass prototype filter in Chapter 4. The novel coupled resonator circuit is presented which extends the conventional coupled resonator theory to include a transistor. Different topologies for the coupled resonator circuits with a transistor can lead to two forms of circuits. One form of the circuit is where a transistor is included into the last resonator. The other form is where the transistor is included between adjacent resonators. Mathematical derivations for the coupled resonator circuits including the transistor are presented as well as formula to generate theoretical S-parameters. A novel matrix $[T]$ is introduced to describe the characteristics of the

transistor. Chapter 4 has given the theoretical part of the thesis, and enables the design process for filters integrated with amplifiers using simple coupling matrix synthesis methods. To the author's knowledge, it is the first coupling matrix that incorporated an active device (transistor) into a coupled resonator circuit. Using this novel coupling matrix, designs for filters can be achieved with small signal transistor amplifiers with predicted frequency responses.

Design examples using novel coupling matrix method in Chapter 4 are demonstrated as a microstrip filtering amplifier in Chapter 5 and a waveguide filtering amplifier in Chapter 6.

The microstrip filtering amplifier is discussed in Chapter 5, which is third order and built using hairpin resonators at a centre frequency of 8.4 GHz and 500 MHz bandwidth. In this microstrip implementation, three resonators are used with two conventional hairpin resonators and a quasi-hairpin resonator integrating the transistor. Details of mathematical procedures for the coupling matrix are given for the hairpin filtering amplifier with a simple Chebyshev lowpass filter. The hairpin amplifier is fabricated on a commercially available substrate and tested. The measurement results show 3 clear poles with 10 dB return loss in the passband and 10 dB gain. This microstrip design example has successfully demonstrated that filtering amplifiers can be designed using the simple coupling matrix synthesis method. Using this design approach, the circuits for impedance matching and interconnection transmission lines between a filter and an amplifier has been largely removed.

The objective of the work described in Chapter 6 is to demonstrate that a coupling matrix can be formulated to design a waveguide filter with an amplifier. This example is given with a third order waveguide amplifier with 9.1 GHz centre frequency and 400 MHz bandwidth. There are three resonators constructed with waveguides for this design. Two of the resonators are conventional waveguide resonators and the other one is a quasi-waveguide resonator which integrates the transistor via a rectangular waveguide-to-microstrip transition. For the X band circuit demonstrator described a third order Chebyshev with -20 dB reflection in the passband at centre frequency of 9.1 GHz for the bandwidth of 400 MHz is used. The close correlation between the

S-parameter response using the coupling matrix and the circuit measurement validates that the matrix description is sufficiently accurate to constitute a useful approach.

To summarise the design processes in Chapter 5 and Chapter 6, an additional matrix $[T]$ introduced in Chapter 4 describing the transistor characteristics which is added into conventional passive coupling matrix for filters, and this leads to an overall circuit response which predicts return losses and amplification gains close to the theoretically predicted values. Further frequency offsets in the form of non-zero diagonal coupling matrix terms are added to compensate for the asymmetry in the amplifier equivalent circuit. Therefore, a completely populated matrix can be formed for the amplifier circuit. Semi-empirical simulation trials are used to realise physical geometries corresponding to the matrix values for a given circuit technology. The work described here makes it possible to extend this methodology to amplifier circuit designs. The novel design of combined matching and filtering by removing the planar matching circuits into waveguide can be a promising application for very high frequencies for lower loss (e.g. THz circuits and systems in Chapter 2).

This design approach using coupling matrix has some limitations. At the moment, filtering amplifiers are described with filter characteristics such as bandwidth, centre frequency, order and ripples. In the design examples, good simulated noise performances have been achieved using coupling matrix for the microstrip amplifier in Chapter 5 and waveguide amplifier in Chapter 6. It is believed that the optimal simulated noise performances are achieved coincidentally with good tradeoffs between gains and noise figures. However, designers of amplifiers such as low noise amplifiers are interested in noise figure, gains. To achieve the best noise performance for amplifiers, the transistor should be designed for the optimal noise performance impedance at the input and maximum gain at the output. Using this coupling matrix design method, filtering amplifiers are not able to design for a particular input impedance for any achievable noise performance or gain.

7.2 Future Work

In this section, possible future development based on the work in the thesis are given below:

* Terahertz Waveguide Amplifiers

  In Chapter 6, an X band rectangular waveguide amplifier is presented with a standard X band rectangular waveguide input and a microstrip output and tested with an SMA connector. Circuits with these port configurations are difficult to measure at higher frequencies (e.g. over 100 GHz). Waveguide flanges are commonly used for higher frequencies measurement over 100 GHz. For an amplifier to work in THz frequency range the waveguide ports are required at both ends. The same waveguide measurement flanges are used as those presented in Chapter 3 for the WR-3 band rectangular waveguide. A THz waveguide amplifier with both waveguide ports can be designed using the design approach given in Chapter 6. The physical structure and layout possibly follow the diagrams presented in Chapter 2.

* Coupling Matrix for Communication Components and Systems

  The general coupling matrix and its synthesis have been investigated for microwave filters for microwave systems. It has also been extended to mupltiport circuits, for instance, power dividers [139], diplexers [139, 140] and multiplexer [123, 141]. Also the coupling matrix synthesis methods have been used for applications with antennas [142–144] and 90 degree hybrid couplers [145]. In this thesis, the novel transistor matrix $[T]$ is introduced in Chapter 4 as an additional matrix which can be integrated in the coupling matrix for filters. Those documented coupling matrices for passive circuits such as power dividers, multiplexers, antennas and couplers can be also extended with the $[T]$ matrix for communication components to enable a design approach for passive circuits with amplifiers. A whole communication system could possibly be described with a coupling matrix as a

large complete matrix.

* Coupling Matrix Synthesis for transistors between resonators circuit model.

  In this thesis, the filtering amplifier circuits have been demonstrated either on microstrip in Chapter 5 or with waveguide in Chapter 6. Both circuits follow the coupled resonator circuit model where one transistor is included into the last resonator for the whole filter circuit, documented in Section 4.6. The synthesis method of the coupling matrix for both circuits uses the simple but well-documented Chebyshev circuit prototype to estimate the responses with assumptions that each resonator shares a common centre resonating frequency. There is a possibility using the coupled resonator circuit model in Section 4.7 where a transistor is placed between resonators. In this model, the capacitor between the transistor gate to drain is used as the inter-resonator coupling factor between adjacent resonators. New synthesis or optimisation algorithms for the filter characteristics are needed rather than conventional Chebyshev lowpass filter prototype synthesis method.

Appendix A

One-port measurement for external quality factor

One port measurement method can be used to extract the quality factor, which has been used to extract the quality factor Q_{eT} in Chapter 5 and Chapter 6 for the integrated transistor resonator. The calculation presented in this appendix is based on [173] using the circuit model given in Chapter 5.

Figure A.1 (a) shows the reflection coefficient, the S_{11} in magnitude for a resonator. In this case, the centre frequency f_0 = 8.4 GHz with magnitude 0.971 and other frequencies are tabulated in Table A.1. Figure A.1 (b) is the corresponding Smith chart.

Freq(f_i)	8.280	8.540	8.230	8.600	8.190	8.660
Magnitude	0.974	0.977	0.977	0.980	0.979	0.983

Table A.1: Simulation sampling points of the one port Q measurement.

For the one-port measurement method by reflection coefficient to extract the quality factor, the key things are to find the coupling coefficient β and the centre frequency f_0 and the magnitude of S_{11} at points other than the resonant frequency.

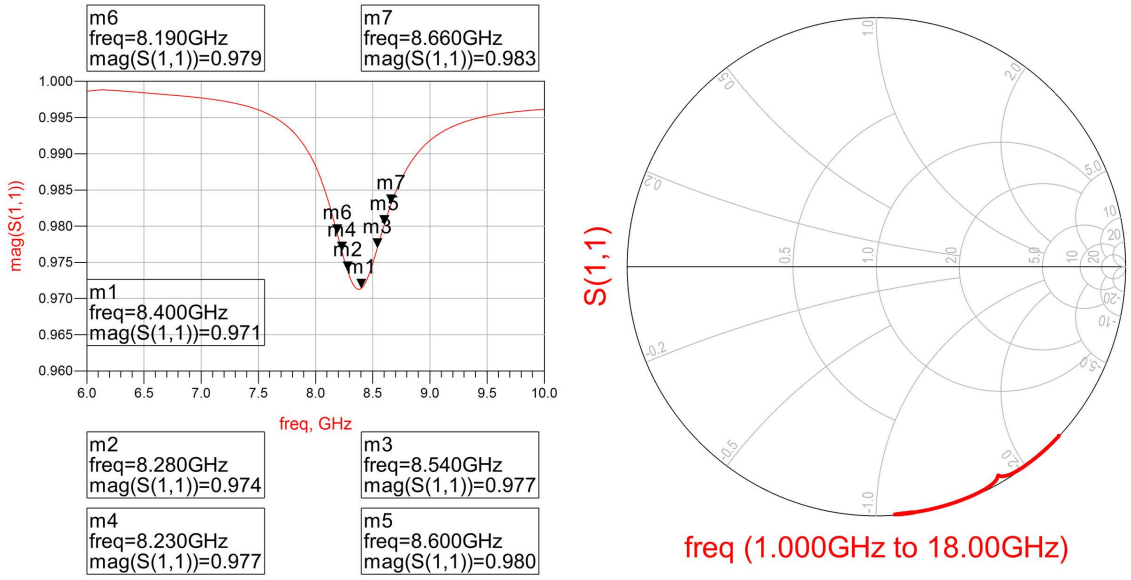

(a) (b)

Figure A.1: (a) Simulation magnitude of a cavity resonator. (b) A Smith chart of one resonator circuit.

The coupling coefficient β is determined as,

$$\beta = \frac{1 + |S_{11}(f_0)|}{1 - |S_{11}(f_0)|} \tag{A.0.1}$$

where $|S_{11}(f_0)|$ is the magnitude of S_{11} at f_0. Using the data given in Figure A.1 (a), it gives β = 67.9655.

The unloaded quality factor of the resonator Q_0 is defined as

$$Q_0 = \frac{1}{\Delta(f_i)} \sqrt{\frac{|S_{11}(f_i)|^2(1+\beta)^2 - (1-\beta)^2}{1 - |S_{11}(f_i)|^2}} \tag{A.0.2}$$

where f_i is some frequency other the resonant frequency f_0 and the magnitude of S_{11} can be measured accurately, which is given in Table A.1. Usually another frequency $f_i = 1.5 f_0$ can be used to find out the unloaded quality factor Q_0. The $\Delta(f_i)$ is defined as,

$$\Delta(f_i) = 2(\frac{f_i - f_0}{f_0}) \tag{A.0.3}$$

However, it is suggested that a more accurate value for Q_0 can be found by considering more frequencies f_i around the f_0 and take the average of the values of Q_{0i} for each f_i over the sample number n as,

$$Q_0 = \frac{\sum_{i=1}^{n} Q_{0i}}{n} \tag{A.0.4}$$

The loaded quality factor Q_L is defined as,

$$Q_L = \frac{Q_0}{1+\beta} \tag{A.0.5}$$

Finally, the external quality factor Q_e follows this equation,

$$Q_e = \frac{1}{\frac{1}{Q_L} - \frac{1}{Q_0}} \tag{A.0.6}$$

The resultant is $Q_e = 13.4359$ in this example.

Appendix B

WR-3 Rectangular Waveguide Fabrication Procedures

A WR-3 band (220-325 GHz) rectangular waveguide with bends is designed with 5 layer structure in Chapter 3. The standard waveguide aperture dimensions for WR-3 band are 864 μm × 432 μm. The 864 μm wide wall is divided into constructions of 3 layers, and each layer has 288 μm thickness. The WR-3 band rectangular waveguide consists of 5 SU-8 layers in total. The fabrication can integrate the top and bottom two layers with double layer fabrication techniques, thus making three standalone SU-8 pieces in lieu of 5 individual pieces. The top and bottom joint pieces are of same thickness 576 μm and the middle piece is of 288 μm. The fabrication is completed by the SU-8 photolithography micromachining method with double joint layer techniques to minimise the number of assembly gaps between SU-8 pieces. All the procedures are carried out in the in-house class 10,000 clean room facilities. The metallisation stage is completed in-house facility by evaporation. For instance, the fabrication process for the joined top piece for layer 1 and layer 2 follows [99, 100]:

1. Spin Coat the first layer: A small amount SU-8 50 photoresist is dispensed and spun onto the polished surface of a 100-mm Silicon wafer, the weighted SU-8 50 of 3.6 gram giving

the final SU-8 substrate thickness of 288 μm.

2. Soft Bake the first layer: The SU-8 wafer is heated from room temperature to 65 °C for 20 minutes after it has rested overnight on a leveled stage (at least 6 hours). After the pre-heating of the hotplate, the temperature is increased to 95 °C for a constant bake for 3 hours. The SU-8 wafer will cool down to room temperature naturally.

3. Exposure for the first layer: The SU-8 photoresist wafer is loaded into the Canon PLA-510 mask aligner. It is then exposed for 30 seconds with UV filters PL360 and L39. This exposure is repeated for another 3 times with intervals of 2 minutes between every exposure. After completing the exposure, another batch of exposures with only filter PL360 loaded for 30 seconds each time with 4 exposures in total.

4. Post-Exposure Bake (PEB) the first layer: The bake is started immediately after the completion of the exposure. The SU-8 photoresist wafer is baked at 70 °C for 15 minutes on hotplate and rested to cool down to room temperate. This short time post-exposure bake can create weak cross links in the photoresist.

5. Spin Coat for the second layer: The second spin coat starts after the SU-8 photoresist wafer is at room temperature with the same amount 3.6 gram of SU-8 50 photoresist spun onto the first layer, giving the thickness of 576 μm.

6. Soft Bake for the joined layers: The soft bake start soon after the spin coating. The soft bake is set for the whole SU-8 photoresist wafer at 70 °C for 5.5 hours.

7. Exposure for the joint layers: This exposure follows the same operation procedures as the first exposure. The SU-8 photoresist wafer is exposed for 30 seconds for four times with 2 minutes intervals between each exposure, filters PL360 and L39 loaded. The next round of exposure starts with only filter PL360 are loaded. This round of exposures are 4 times of 30 minutes exposures with 2 minute intervals. During this round of exposure

of the second layer, the long wave UV light was able to penetrate both SU-8 layers and a strong cross-link is formed and bond the layers together seamlessly.

8. Post Exposure Bake for the joint layers: The post exposure bake is set to 30 minutes at 70 °C for the SU-8 photoresist wafer and 2 hours of bake at 95 °C.

9. Development for the SU-8 piece: After the baked SU-8 photoresist wafer has cooled down to room temperature, it was put into the EC solvent for 30 minutes at 110 °C to release and separate the SU-8 from the Silicon substrate wafer. After development, the two joint SU-8 layers are released from the Silicon wafer with 10 % sodium hydroxide solution rinsed.

10. Metallisation for the SU-8 piece: Evaporation process is used to metallise the SU-8 pieces in a Cressington 308R metal evaporator. The SU-8 pieces are cleaned by oxygen plasma for 30 seconds and then a 100 nm Cr layer is deposited as an adhesive layer. A 2 μm thick silver thin film is then deposited on the surface of SU-8. To achieve a full coverage on the sidewalls, the sample was tilted to 30° and rotated during the evaporation so that the sidewalls are fully covered by silver. The same metallisation procedures are repeated for the other side of the SU-8 layer.

11. Repetition for other SU-8 pieces: Repeat the previous procedures of fabrication and metallisation for other SU-8 pieces.

12. Assembly for the SU-8 device: Once all the SU-8 pieces are made and coated, all those SU-8 pieces are carefully assembled and sandwiched by two brass plates with the precisely made screws, alignment pins.

REFERENCES

[1] D.M. Pozar. *Microwave engineering*. J. Wiley, 2005.

[2] Shang Xiaobang, Tian Yingtao, M. J. Lancaster, and S. Singh. A su8 micromachined wr-1.5 band waveguide filter. *Microwave and Wireless Components Letters, IEEE*, 23(6):300–302, 2013.

[3] M. Abdolhamidi and M. Shahabadi. X-band substrate integrated waveguide amplifier. *Microwave and Wireless Components Letters, IEEE*, 18(12):815–817, 2008.

[4] D. Pukala, L. Samoska, T. Gaier, A. Fung, X. B. Mei, W. Yoshida, J. Lee, J. Uyeda, P. H. Liu, W. R. Deal, V. Radisic, and R. Lai. Submillimeter-wave inp mmic amplifiers from 300-345 ghz. *Microwave and Wireless Components Letters, IEEE*, 18(1):61–63, 2008.

[5] A. Tessmann, A. Leuther, V. Hurm, H. Massler, M. Zink, M. Kuri, M. Riessle, R. Losch, M. Schlechtweg, and O. Ambacher. A 300 ghz mhemt amplifier module. In *Indium Phosphide and Related Materials, 2009. IPRM '09. IEEE International Conference on*, pages 196–199.

[6] E. Laskin, P. Chevalier, A. Chantre, B. Sautreuil, and S. P. Voinigescu. 80/160-ghz transceiver and 140-ghz amplifier in sige technology. In *Radio Frequency Integrated Circuits (RFIC) Symposium, 2007 IEEE*, pages 153–156.

[7] E. Laskin, P. Chevalier, A. Chantre, B. Sautreuil, and S. P. Voinigescu. 165-ghz transceiver in sige technology. *Solid-State Circuits, IEEE Journal of*, 43(5):1087–1100, 2008.

[8] S. M. Marazita, W. L. Bishop, T. M. Cunningham, P. J. Koh, T. W. Crowe, and R. M. Weikle Ii. Planar gaas schottky barrier diodes. pages 208–223. 8th Int. Symp. Terahertz Technol.

[9] Mou Jinchao, Yuan Yong, Lv Xin, Yu Weihua, He Dawei, Wang Jinghui, and Xiao Guohua. Design and fabrication of planar gaas schottky barrier diodes for submillimeter-wave applications. In *Microwave and Millimeter Wave Technology (ICMMT), 2010 International Conference on*, pages 1746–1749.

[10] B. Thomas, B. Alderman, D. Matheson, and P. de Maagt. A combined 380 ghz mixer/doubler circuit based on planar schottky diodes. *Microwave and Wireless Components Letters, IEEE*, 18(5):353–355, 2008.

[11] Roberto Sorrentino and Giovanni Bianchi. *Microwave and RF engineering*, volume 1. John Wiley and Sons, 2010.

[12] Javier Gozalvez. Mobile traffic expected to grow more than 30-fold [mobile radio]. *Vehicular Technology Magazine, IEEE*, 6(3):9–15, 2011.

[13] Song Ho-Jin and T. Nagatsuma. Present and future of terahertz communications. *Terahertz Science and Technology, IEEE Transactions on*, 1(1):256–263, 2011.

[14] G Roberto Aiello and Gerald D Rogerson. Ultra-wideband wireless systems. *Microwave Magazine, IEEE*, 4(2):36–47, 2003.

[15] Peter Smulders. Exploiting the 60 ghz band for local wireless multimedia access: prospects and future directions. *Communications Magazine, IEEE*, 40(1):140–147, 2002.

[16] Robert C Daniels and Robert W Heath. 60 ghz wireless communications: emerging requirements and design recommendations. *Vehicular Technology Magazine, IEEE*, 2(3):41–50, 2007.

[17] Nan Guo, Robert C Qiu, Shaomin S Mo, and Kazuaki Takahashi. 60-ghz millimeter-wave radio: Principle, technology, and new results. *EURASIP Journal on Wireless Communications and Networking*, 2007(1):48–48, 2007.

[18] Stephen G Wilson, Mat Brandt-Pearce, Qianling Cao, and James H Leveque III. Free-space optical mimo transmission with-ary ppm. *Communications, IEEE Transactions on*, 53(8):1402–1412, 2005.

[19] Neda Cvijetic, Dayou Qian, and Ting Wang. 10gb/s free-space optical transmission using ofdm. In *Optical Fiber Communication Conference*, page OThD2. Optical Society of America.

[20] Song Ho-Jin, K. Ajito, A. Wakatsuki, Y. Muramoto, N. Kukutsu, Y. Kado, and T. Nagatsuma. Terahertz wireless communication link at 300 ghz. In *Microwave Photonics (MWP), 2010 IEEE Topical Meeting on*, pages 42–45.

[21] Y. Kado. Sub-terahertz ultrahigh-speed wireless links. In *Circuits and Systems (MWSCAS), 2011 IEEE 54th International Midwest Symposium on*, pages 1–4.

[22] R. Piesiewicz, T. Kleine-Ostmann, N. Krumbholz, D. Mittleman, M. Koch, J. Schoebel, and T. Kurner. Short-range ultra-broadband terahertz communications: Concepts and perspectives. *Antennas and Propagation Magazine, IEEE*, 49(6):24–39, 2007.

[23] M. Koch. Terahertz applications and techniques. In *Optical Fiber Communication and the National Fiber Optic Engineers Conference, 2007. OFC/NFOEC 2007. Conference on*, pages 1–3.

[24] F. Khan and Pi Zhouyue. mmwave mobile broadband (mmb): Unleashing the 3-300ghz spectrum. In *Sarnoff Symposium, 2011 34th IEEE*, pages 1–6.

[25] C. M. Armstrong. The truth about terahertz. *Spectrum, IEEE*, 49(9):36–41, 2012.

[26] Huang Kao-Cheng and Wang Zhaocheng. Terahertz terabit wireless communication. *Microwave Magazine, IEEE*, 12(4):108–116, 2011.

[27] Thomas Kleine-Ostmann and Tadao Nagatsuma. A review on terahertz communications research. *Journal of Infrared, Millimeter, and Terahertz Waves*, 32(2):143–171, 2011.

[28] R. Piesiewicz, T. Kleine-Ostmann, N. Krumbholz, D. Mittleman, M. Koch, and T. Kurner. Concept and perspectives of future ultra broadband thz communication systems. In *Infrared Millimeter Waves and 14th International Conference on Teraherz Electronics, 2006. IRMMW-THz 2006. Joint 31st International Conference on*, pages 96–96.

[29] John Federici and L. Moeller. Review of terahertz and subterahertz wireless communications. *Journal of Applied Physics*, 107(11):111101–111101–22, 2010.

[30] Rieh Jae-Sung and Kim Dong-Hyun. An overview of semiconductor technologies and circuits for terahertz communication applications. In *GLOBECOM Workshops, 2009 IEEE*, pages 1–6.

[31] Rieh Jae-Sung, Jeon Sanggeun, and Kim Moonil. An overview of integrated thz electronics for communication applications. In *Circuits and Systems (MWSCAS), 2011 IEEE 54th International Midwest Symposium on*, pages 1–4.

[32] L. A. Samoska. An overview of solid-state integrated circuit amplifiers in the submillimeter-wave and thz regime. *Terahertz Science and Technology, IEEE Transactions on*, 1(1):9–24, 2011.

[33] W. Deal, X. B. Mei, K. M. K. H. Leong, V. Radisic, S. Sarkozy, and R. Lai. Thz monolithic integrated circuits using inp high electron mobility transistors. *Terahertz Science and Technology, IEEE Transactions on*, 1(1):25–32, 2011.

[34] R. Appleby and H. B. Wallace. Standoff detection of weapons and contraband in the 100 ghz to 1 thz region. *Antennas and Propagation, IEEE Transactions on*, 55(11):2944–2956, 2007.

[35] N. Kukutsu, A. Hirata, M. Yaita, K. Ajito, H. Takahashi, T. Kosugi, H. Song, A. Wakatsuki, Y. Muramoto, T. Nagatsuma, and Y. Kado. Toward practical applications over 100 ghz. In *Microwave Symposium Digest (MTT), 2010 IEEE MTT-S International*, pages 1–1.

[36] Elizabeth Berry, Gillian C Walker, Anthony J Fitzgerald, NN Zinovev, Martyn Chamberlain, Stephen W Smye, Robert E Miles, and Michael A Smith. Do in vivo terahertz imaging systems comply with safety guidelines? *Journal of Laser Applications*, 15(3):192–198, 2003.

[37] RH Clothier and N Bourne. Effects of thz exposure on human primary keratinocyte differentiation and viability. *Journal of biological physics*, 29(2-3):179–185, 2003.

[38] A. Fitzgerald, E. Pickwell, V. Wallace, A. Purushotham, S. Pinder, M. Linan, R. Pye, and T. Ha. Medical applications of broadband terahertz pulsed radiation. In *Lasers and Electro-Optics Society, 2005. LEOS 2005. The 18th Annual Meeting of the IEEE*, pages 120–121.

[39] M. Walther, B. Fischer, M. Schall, H, and P. Uhd Jepsen. Far-infrared vibrational spectra of all-trans, 9-cis and 13-cis retinal measured by thz time-domain spectroscopy. *Chemical Physics Letters*, 332(34):389–395, 2000.

[40] C. Jastrow, S. Priebe, B. Spitschan, J. Hartmann, M. Jacob, T. Kurner, T. Schrader, and T. Kleine-Ostmann. Wireless digital data transmission at 300 ghz. *Electronics Letters*, 46(9):661–663, 2010.

[41] C. Jastrow, K. Munter, R. Piesiewicz, T. Kurner, M. Koch, and T. Kleine-Ostmann. 300 ghz transmission system. *Electronics Letters*, 44(3):213–214, 2008.

[42] DM Britz. Evolution of extreme bandwidth personal and local area terahertz wireless networks. In *Extended abstracts of 2nd international workshop on terahertz technology (TeraTech09)*, pages 113–120.

[43] M. Satyanarayanan. Pervasive computing: vision and challenges. *Personal Communications, IEEE*, 8(4):10–17, 2001.

[44] Zhang Bo, Fan Yong, and Chen Zhe. 220-ghz-band wireless link system using all-electronic technologies for 20gbit/s data transmission. In *Intelligent Signal Processing and Communication Systems (ISPACS), 2010 International Symposium on*, pages 1–3.

[45] M. Y. W. Chia, C. K. Ang, B. Luo, and S. W. Leong. Wideband 307 ghz transceiver system for high speed digital wireless at 12.5 gbps. In *Microwave Symposium Digest (MTT), 2011 IEEE MTT-S International*, pages 1–4.

[46] P.H. Siegel, R.J. Dengler, I. Mehdi, J.E. Oswald, W.L. Bishop, T.W. Crowe, and R.J. Mattauch. Measurements on a 215-ghz subharmonically pumped waveguide mixer using planar back-to-back air-bridge schottky diodes. *Microwave Theory and Techniques, IEEE Transactions on*, 41(11):1913–1921, 1993.

[47] P.H. Siegel, RJ Dengler, I. Mehdi, WL Bishop, and TW Crowe. A 200 ghz planar diode subharmonically pumped waveguide mixer with state-of-the-art performance. pages 595–598 vol. 2. IEEE.

[48] FP Mena, J. Kooi, AM Baryshev, CFJ Lodewijk, TM Klapwijk, W. Wild, V. Desmaris, D. Meledin, A. Pavolotsky, and V. Belitsky. Rf performance of a 600c720 ghz sideband-separating mixer with all-copper micromachined waveguide mixer block.

[49] G. Narayanan, CK Walker, H. Knoepfle, and J. Capara. Design of mixer elements for the hht 345 ghz heterodyne array receiver. pages 433–442.

[50] C.W. Kim, S.S. Lee, B.H. Park, Y. Shim, and S.G. Lee. A cmos direct-conversion i/q up-mixer block for ultra-wideband system. volume 1, pages 230–232. IEEE.

[51] A. Baryshev, E. Lauria, R. Hesper, T. Zijlstra, and W. Wild. Fixed-tuned waveguide 0.6 thz sis mixer with wide band if. pages 1–4.

[52] I. Mehdi, TH Lee, DA Humphrey, SC Martin, RJ Dengler, JE Oswald, A. Pease, RP Smith, and PH Siegel. 600 ghz planar-schottky-diode subharmonic waveguide mixers. volume 1, pages 377–380 vol. 1. IEEE.

[53] J. Schur, S. Biber, O. Cojocari, B. Mottet, LP Schmidt, and HL Hartnagel. 600 ghz heterodyne mixer in waveguide technology using a gaas schottky diode.

[54] E.T. Schlecht, J.J. Gill, R.H. Lin, R.J. Dengler, and I. Mehdi. A 520c590 ghz crossbar balanced fundamental schottky mixer. *Microwave and Wireless Components Letters, IEEE*, 20(7):387–389, 2010.

[55] J. Schur, S. Biber, F. Gumbmann, B. Mottet, O. Cojocari, L. P. Schmidt, and H. L. Hartnagel. Micromachined split-block schottky-diode mixer for 600 ghz. In *Infrared and Millimeter Waves, 2004 and 12th International Conference on Terahertz Electronics, 2004. Conference Digest of the 2004 Joint 29th International Conference on*, pages 325–326.

[56] K. Hui, J. L. Hesler, D. S. Kurtz, W. L. Bishop, and T. W. Crowe. A micromachined 585 ghz schottky mixer. *Microwave and Guided Wave Letters, IEEE*, 10(9):374–376, 2000.

[57] Y. Serizawa, Y. Sekimoto, M. Kamikura, W. Shan, and T. Ito. A 400c500 ghz balanced sis mixer with a waveguide quadrature hybrid coupler. *International Journal of Infrared and Millimeter Waves*, 29(9):846–861, 2008.

[58] C.Y.E. Tong, R. Blundell, K.G. Megerian, J.A. Stern, and H.G. LeDuc. A 650 ghz fixed-tuned waveguide sis distributed mixer with no integrated tuning circuit. *Applied Superconductivity, IEEE Transactions on*, 13(2):680–683, 2003.

[59] AR Kerr, SK Pan, AW Lichtenberger, N. Horner, JE Effland, and K. Crady. A single-chip balanced sis mixer for 200c300 ghz. page 251C259. Citeseer.

[60] AM Baryshev, FP Mena, R. Hesper, T. Zijlstra, CFJ Lodewijk, W. Wild, and TM Klapwijk. A waveguide nbtin sis mixer for thz array applications. pages 392–392. IEEE.

[61] D. Meledin, A. Pavolotsky, V. Desmaris, I. Lapkin, C. Risacher, V. Perez, D. Henke, O. Nystrom, E. Sundin, and D. Dochev. A 1.3-thz balanced waveguide heb mixer for the apex telescope. *Microwave Theory and Techniques, IEEE Transactions on*, 57(1):89–98, 2009.

[62] P.P. Munoz, S. Bedorf, M. Brandt, T. Tils, N. Honingh, and K. Jacobs. Thz waveguide mixers with nbtin hebs on silicon nitride membranes. *Microwave and Wireless Components Letters, IEEE*, 16(11):606–608, 2006.

[63] P. Putz, K. Jacobs, M. Justen, F. Schomaker, M. Schultz, S. Wulff, and CE Honingh. Nbtin hot electron bolometer waveguide mixers on membranes at thz frequencies. *Applied Superconductivity, IEEE Transactions on*, (99):1–1, 2011.

[64] L. Jiang, S. Shiba, K. Shimbo, N. Sakai, T. Yamakura, M. Sugimura, PG Ananthasubramanian, H. Maezawa, Y. Irimajiri, and S. Yamamoto. Development of thz waveguide nbtin heb mixers. *Applied Superconductivity, IEEE Transactions on*, 19(3):301–304, 2009.

[65] I. Ederra, L. Azcona, B.E.J. Alderman, A. Laisne, R. Gonzalo, C.M. Mann, D.N. Matheson, and P. de Maagt. A 250 ghz subharmonic mixer design using ebg technology. *Antennas and Propagation, IEEE Transactions on*, 55(11):2974–2982, 2007.

[66] SMX Claude, CT Cunningham, AR Kerr, and SK Pan. Design of a sideband-separating balanced sis mixer based on waveguide hybrids. *ALMA Memo Series, Memo*, 316, 2000.

[67] AR Kerr, SK Pan, and HG LeDuc. An integrated sideband separating sis mixer for 200-280 ghz. pages 17–19.

[68] Jiao Yuqing, Zhu Yunpeng, Hong Xuezhi, Shi Yaocheng, Xu Lei, and He Sailing. An integrated optical mixer based on su8 polymer for pdm-qpsk demodulation. *Photonics Technology Letters, IEEE*, 23(20):1490–1492, 2011.

[69] J. D. Albrecht, M. J. Rosker, H. B. Wallace, and Chang Tsu-Hsi. Thz electronics projects at darpa: Transistors, tmics, and amplifiers. In *Microwave Symposium Digest (MTT), 2010 IEEE MTT-S International*, pages 1118–1121.

[70] L. Samoska, W. R. Deal, G. Chattopadhyay, D. Pukala, A. Fung, T. Gaier, M. Soria, V. Radisic, X. Mei, and R. Lai. A submillimeter-wave hemt amplifier module with integrated waveguide transitions operating above 300 ghz. *Microwave Theory and Techniques, IEEE Transactions on*, 56(6):1380–1388, 2008.

[71] W. Y. Liu, D. Steenson, and M. B. Steer. Membrane-supported cpw with mounted active devices. *Microwave and Wireless Components Letters, IEEE*, 11(4):167–169, 2001.

[72] D. Mirshekar-Syahkal and B. J. Davies. Accurate solution of microstrip and coplanar structures for dispersion and for dielectric and conductor losses. *Microwave Theory and Techniques, IEEE Transactions on*, 27(7):694–699, 1979.

[73] M.J. Lancaster, J. Zhou, M. Ke, Y. Wang, and K. Jiang. Design and high performance of a micromachined k-band rectangular coaxial cable. *Microwave Theory and Techniques, IEEE Transactions on*, 55(7):1548–1553, 2007.

[74] Ke Maolong, Wang Yi, K. Jiang, and M. J. Lancaster. Micromachined rectangular coaxial line and cavity resonator for 77 ghz applications using su8 photoresist. In *Microwave Conference, 2008. APMC 2008. Asia-Pacific*, pages 1–4.

[75] P. J. Bruneau, H. D. Janzen, and J. S. Ward. Machining of terahertz split-block waveguides with micrometer precision. In *Infrared, Millimeter and Terahertz Waves, 2008. IRMMW-THz 2008. 33rd International Conference on*, pages 1–2.

[76] Christopher E Groppi, Brian Love, Matthew Underhill, and Christopher Walker. Automated cnc micromachining for integrated thz waveguide circuits. *Work*, 300:250x220x200mm, 2010.

[77] Li Yuan, I. Mehdi, A. Maestrini, R. H. Lin, and J. Papapolymerou. A broadband 900-ghz silicon micromachined two-anode frequency tripler. *Microwave Theory and Techniques, IEEE Transactions on*, 59(6):1673–1681, 2011.

[78] S. Biber, J. Schur, Arnd Hofmann, and L. Schmidt. Design of new passive thz devices based on micromachining techniques. In *Physics and Engineering of Microwaves, Millimeter, and Submillimeter Waves, 2004. MSMW 04. The Fifth International Kharkov Symposium on*, volume 1, pages 26–31 Vol.1.

[79] S. Biber, J. Schur, and L. P. Schmidt. Technological issues for micromachining of new passive thz-components based on deep-trench silicon etching. In *Infrared and Millimeter Waves, 2004 and 12th International Conference on Terahertz Electronics, 2004. Conference Digest of the 2004 Joint 29th International Conference on*, pages 145–146.

[80] Shang Xiaobang, Ke Maolong, Wang Yi, and M. J. Lancaster. Wr-3 band waveguides and filters fabricated using su8 photoresist micromachining technology. *Terahertz Science and Technology, IEEE Transactions on*, 2(6):629–637, 2012.

[81] Ren Yang and Wanjun Wang. A numerical and experimental study on gap compensation and wavelength selection in uv-lithography of ultra-high aspect ratio su-8 microstructures. *Sensors and Actuators B: Chemical*, 110(2):279–288, 2005.

[82] S. Shimizu, K. Kuribayashi, M. Ohno, T. Taniguchi, and T. Ueda. Low temperature reactive ion etching for bulk micromachining. In *Emerging Technologies and Factory Automation, 1994. ETFA '94., IEEE Symposium on*, pages 48–52.

[83] C. Marxer and N. F. de Rooij. Micro-opto-mechanical 2 x 2 switch for single-mode fibers based on plasma-etched silicon mirror and electrostatic actuation. *Lightwave Technology, Journal of*, 17(1):2–6, 1999.

[84] P. Blondy, A. R. Brown, D. Cros, and G. M. Rebeiz. Low-loss micromachined filters for millimeter-wave communication systems. *Microwave Theory and Techniques, IEEE Transactions on*, 46(12):2283–2288, 1998.

[85] Li Yuan, P. L. Kirby, and J. Papapolymerou. Silicon micromachined w-band folded and straight waveguides using drie technique. In *Microwave Symposium Digest, 2006. IEEE MTT-S International*, pages 1915–1918.

[86] Y. Li, P. L. Kirby, O. Offranc, and J. Papapolymerou. Silicon micromachined w-band hybrid coupler and power divider using drie technique. *Microwave and Wireless Components Letters, IEEE*, 18(1):22–24, 2008.

[87] Tai-Ran Hsu. *MEMS and Microsystems: Design, Manufacture, and Nanoscale Engineering*. John Wiley and Sons, 2008.

[88] Yunn-Shiuan Liao and Ying-Tung Chen. Precision fabrication of an arrayed micro metal probe by the laser-liga process. *Journal of Micromechanics and Microengineering*, 15(12):2433, 2005.

[89] Radosvet Arnaudov, Bojidar Avdjiiski, Aleksandar Kostov, Valentin Videkov, Svetozar Andreev, and Nikola Yordanov. Novel microcontacts in microwave chip carriers developed by uv-liga process. *Advanced Packaging, IEEE Transactions on*, 29(1):122–130, 2006.

[90] Chantal Khan Malek and Volker Saile. Applications of liga technology to precision manufacturing of high-aspect-ratio micro-components and-systems: a review. *Microelectronics Journal*, 35(2):131–143, 2004.

[91] T. L. Willke and S. S. Gearhart. Liga micromachined planar transmission lines and filters. *Microwave Theory and Techniques, IEEE Transactions on*, 45(10):1681–1688, 1997.

[92] C. H. Smith, A. Sklavonuos, and N. S. Barker. Su-8 micromachining of millimeter and submillimeter waveguide circuits. In *Microwave Symposium Digest, 2009. MTT '09. IEEE MTT-S International*, pages 961–964.

[93] W. H. Chow, A. Champion, and D. P. Steenson. Measurements to 320 ghz of millimetre-wave waveguide components made by high precision and economic micro-machining techniques. In *High Frequency Postgraduate Student Colloquium, 2003*, pages 90–93.

[94] Hubert Lorenz, M Despont, N Fahrni, N LaBianca, Philippe Renaud, and P Vettiger. Su-8: a low-cost negative resist for mems. *Journal of Micromechanics and Microengineering*, 7(3):121, 1997.

[95] John D Williams and Wanjun Wang. Study on the postbaking process and the effects on uv lithography of high aspect ratio su-8 microstructures. *Journal of Micro/Nanolithography, MEMS, and MOEMS*, 3(4):563–568, 2004.

[96] M. Ke, Y. Wang, and M. Lancaster. Design and realisation of low loss airfilled rectangular coaxial cable with bent quarterwavelength supporting stubs. *Microwave and Optical Technology Letters*, 50(5):1443–1446, 2008.

[97] M. Despont, H. Lorenz, N. Fahrni, J. Brugger, P. Renaud, and P. Vettiger. High-aspect-ratio, ultrathick, negative-tone near-uv photoresist for mems applications. In *Micro Electro Mechanical Systems, 1997. MEMS '97, Proceedings, IEEE., Tenth Annual International Workshop on*, pages 518–522.

[98] ML Ke, Y Wang, S Wei, K Jiang, and MJ Lancaster. Precision microfabrication of millimetre-wave components. In *Proc. 9th Int. Conf. and Exhib. on Laser Metrology, Mach. Tool, CMM and Robot. Perform*, pages 397–403.

[99] Yingtao Tian, Xiaobang Shang, and Michael J. Lancaster. Fabrication of multilayered su8 structure for terahertz waveguide with ultralow transmission loss. *Journal of Micro/Nanolithography, MEMS, and MOEMS*, 13(1):013002–013002, 2014. 10.1117/1.JMM.13.1.013002.

[100] Micro Chem. Nano su-8, negative tone photoresist formulations 50-100, 4 pages, feb. 2002.

[101] Sheng Chang, John Warren, and Fu-Pen Chiang. Mechanical testing of epon su-8 with siem. Report, Brookhaven National Lab., Upton, NY (US), 2000.

[102] Alvaro Mata, Aaron J Fleischman, and Shuvo Roy. Fabrication of multi-layer su-8 microstructures. *Journal of micromechanics and microengineering*, 16(2):276, 2006.

[103] Xiaobang Shang. *SU-8 micromachined terahertz waveguide circuits and coupling matrix design of multiple passband filters*. Phd thesis, 2011.

[104] C. H. Smith and N. S. Barker. Su-8 micromachining process for millimeter and submillimeter-wave waveguide circuit fabrication. In *Infrared, Millimeter and Terahertz Waves, 2008. IRMMW-THz 2008. 33rd International Conference on*, pages 1–2.

[105] J Carlier, S Arscott, V Thomy, JC Fourrier, F Caron, JC Camart, C Druon, and P Tabourier. Integrated microfluidics based on multi-layered su-8 for mass spectrometry analysis. *Journal of micromechanics and Microengineering*, 14(4):619, 2004.

[106] Santeri Tuomikoski, Tiina Sikanen, Raimo A. Ketola, Risto Kostiainen, Tapio Kotiaho, and Sami Franssila. Fabrication of enclosed su-8 tips for electrospray ionization-mass spectrometry. *ELECTROPHORESIS*, 26(24):4691–4702, 2005.

[107] J. L. Hesler, K. Hui, R. K. Dahlstrom, R. M. Weikle, T. W. Crowe, C. M. Mann, and H. B. Wallace. Analysis of an octagonal micromachined horn antenna for submillimeter-wave applications. *Antennas and Propagation, IEEE Transactions on*, 49(6):997–1001, 2001.

[108] III Smith, C. H., Xu Haiyong, and N. S. Barker. Development of a multi-layer su-8 process for terahertz frequency waveguide blocks. In *Microwave Symposium Digest, 2005 IEEE MTT-S International*, page 4 pp.

[109] J. W. Digby, C. E. McIntosh, G. M. Parkhurst, B. M. Towlson, S. Hadjiloucas, J. W. Bowen, J. M. Chamberlain, Roger D. Pollard, Robert E. Miles, D. P. Steenson, L. S. Karatzas, N. J. Cronin, and S. R. Davies. Fabrication and characterization of micromachined rectangular waveguide components for use at millimeter-wave and terahertz frequencies. *Microwave Theory and Techniques, IEEE Transactions on*, 48(8):1293–1302, 2000.

[110] A. Rashidian, D. M. Klymyshyn, M. T. Aligodarz, M. Boerner, and J. Mohr. Su-8 resonator antenna. In *Antennas and Propagation Society International Symposium (APSURSI), 2010 IEEE*, pages 1–4.

[111] A. Mahanfar, Lee Sae-Won, A. M. Parameswaran, and R. G. Vaughan. Self-assembled monopole antennas with arbitrary shapes and tilt angles for system-on-chip and system-in-package applications. *Antennas and Propagation, IEEE Transactions on*, 58(9):3020–3028, 2010.

[112] Y. Wang, M. Ke, M.J. Lancaster, and J. Chen. Micromachined 300 ghz su-8 based slotted waveguide antenna. *Antennas and Wireless Propagation Letters, IEEE*, (99):1–1, 2011.

[113] Michael J. Lancaster. Ep/m016269/1 epsrc research grant application, 2014.

[114] Tianhao He Jeff Powell Yingtao Tian Michael J. Lancaster, David Glynn and Xiaobang Shang. Submillimetre rectangular waveguides based on su-8 photoresist micromachining technology, 17-11-2014 2014.

[115] X. Shang, ML Ke, Y. Wang, and MJ Lancaster. Micromachined wr-3 waveguide filter with embedded bends. *Electronics Letters*, 47(9):545–547, 2011.

[116] Micahel Lancaster Rashad Mahmud, Tianhao He. Micromachined travelling wave slotted waveguide antenna array for beam-scanning applications, 10 - 11 November 2014 2014.

[117] T. Skaik, Y. Wang, M. Ke, S. Qian, and M. Lancaster. A micromachined wr-3 waveguide with embedded bends for direct flange connections. pages 1225–1228. IEEE.

[118] F. Sammoura, Cai Ying, Chi Chen-Yu, T. Hirano, Lin Liwei, and Chiao Jung-Chih. A micromachined w-band iris filter. In *Solid-State Sensors, Actuators and Microsystems, 2005. Digest of Technical Papers. TRANSDUCERS '05. The 13th International Conference on*, volume 1, pages 1067–1070 Vol. 1.

[119] Chen Lihan, A. Arsenovic, J. R. Stanec, T. J. Reck, A. W. Lichtenberger, R. M. Weikle, and N. S. Barker. A micromachined terahertz waveguide 90 twist. *Microwave and Wireless Components Letters, IEEE*, 21(5):234–236, 2011.

[120] J. R. Stanec and N. S. Barker. Fabrication and integration of micromachined submillimeter-wave circuits. *Microwave and Wireless Components Letters, IEEE*, 21(8):409–411, 2011.

[121] M. Vahidpour and K. Sarabandi. Micromachined j-band rectangular waveguide filter. In *General Assembly and Scientific Symposium, 2011 XXXth URSI*, pages 1–4.

[122] G. Petencin D. Koller A. R. Kerr, C. Litton and M. Shannon. Loss of gold plated waveguides at 210-280 ghz, 2009.

[123] Shang Xiaobang, Wang Yi, Xia Wenlin, and M. J. Lancaster. Novel multiplexer topologies based on all-resonator structures. *Microwave Theory and Techniques, IEEE Transactions on*, 61(11):3838–3845, 2013.

[124] CST. Cst microwave studio, 2013.

[125] J.S. Hong and J. Lancaster. *Microstrip Filters for Rf/Microwave Applications*. Wiley, 2001.

[126] R. Levy and Seymour B. Cohn. A history of microwave filter research, design, and development. *Microwave Theory and Techniques, IEEE Transactions on*, 32(9):1055–1067, 1984.

[127] R. Levy, R. V. Snyder, and G. Matthaei. Design of microwave filters. *Microwave Theory and Techniques, IEEE Transactions on*, 50(3):783–793, 2002.

[128] A. E. Atia and A. E. Williams. Narrow-bandpass waveguide filters. *Microwave Theory and Techniques, IEEE Transactions on*, 20(4):258–265, 1972.

[129] A. E. Atia and A. E. Williams. Non-minimum phase, optimum amplitude, bandpass waveguide filters. In *Microwave Symposium, 1973 IEEE G-MTT International*, pages 210–212.

[130] A. E. Atia, A. E. Williams, and R. W. Newcomb. Narrow-band multiple-coupled cavity synthesis. *Circuits and Systems, IEEE Transactions on*, 21(5):649–655, 1974.

[131] R.J. Cameron, C.M. Kudsia, and R.R. Mansour. *Microwave filters for communication systems: fundamentals, design, and applications*. Wiley-Interscience, 2007.

[132] Richard J. Cameron. Advanced filter synthesis. *Microwave Magazine, IEEE*, 12(6):42–61, 2011.

[133] Dan Swanson and G. Macchiarella. Microwave filter design by synthesis and optimization. *Microwave Magazine, IEEE*, 8(2):55–69, 2007.

[134] Alexander Casson and Esther Rodriguez-Villegas. A review and modern approach to lc ladder synthesis. *Journal of Low Power Electronics and Applications*, 1(1):20–44, 2011.

[135] S. Amari and M. Bekheit. Physical interpretation and implications of similarity transformations in coupled resonator filter design. *Microwave Theory and Techniques, IEEE Transactions on*, 55(6):1139–1153, 2007.

[136] V. Miraftab and Yu Ming. Generalized lossy microwave filter coupling matrix synthesis and design using mixed technologies. *Microwave Theory and Techniques, IEEE Transactions on*, 56(12):3016–3027, 2008.

[137] V. Miraftab and Yu Ming. Advanced coupling matrix and admittance function synthesis techniques for dissipative microwave filters. *Microwave Theory and Techniques, IEEE Transactions on*, 57(10):2429–2438, 2009.

[138] A. C. Guyette, I. C. Hunter, and Roger D. Pollard. The design of microwave bandpass filters using resonators with nonuniform q. *Microwave Theory and Techniques, IEEE Transactions on*, 54(11):3914–3922, 2006.

[139] T. F. Skaik, M. J. Lancaster, and F. Huang. Synthesis of multiple output coupled resonator circuits using coupling matrix optimisation. *Microwaves, Antennas and Propagation, IET*, 5(9):1081–1088, 2011.

[140] G. Macchiarella and S. Tamiazzo. Novel approach to the synthesis of microwave diplexers. *Microwave Theory and Techniques, IEEE Transactions on*, 54(12):4281–4290, 2006.

[141] G. Macchiarella and S. Tamiazzo. Synthesis of star-junction multiplexers. *Microwave Theory and Techniques, IEEE Transactions on*, 58(12):3732–3741, 2010.

[142] Chung Shyh-Jong and Wang Hsiao-Ning. Compact multi-function antennas designed using filter synthesis technique. In *Microwave Conference (EuMC), 2012 42nd European*, pages 1331–1334.

[143] O. A. Nova, J. C. Bohorquez, N. M. Pena, G. E. Bridges, L. Shafai, and C. Shafai. Filter-antenna module using substrate integrated waveguide cavities. *Antennas and Wireless Propagation Letters, IEEE*, 10:59–62, 2011.

[144] Zhao Luyu, L. K. Yeung, and Wu Ke-Li. A coupled resonator decoupling network for two-element compact antenna arrays in mobile terminals. *Antennas and Propagation, IEEE Transactions on*, 62(5):2767–2776, 2014.

[145] Li Shuli, Lu Shani, and M. J. Lancaster. Wr-3 band butler matrix design using su-8 photoresist technology. In *Passive RF and Microwave Components, 3rd Annual Seminar on*, pages 19–26.

[146] Seymour B. Cohn. Direct-coupled-resonator filters. *Proceedings of the IRE*, 45(2):187–196, 1957.

[147] George L Matthaei, Leo Young, and E Michael Jones. Design of microwave filters, impedance-matching networks, and coupling structures. volume 2. Report, DTIC Document, 1963.

[148] T.R. Cuthbert. *Broadband Direct-Coupled and Matching RF Network*. TRCPEP, 1999.

[149] S. Tamiazzo and G. Macchiarella. An analytical technique for the synthesis of cascaded n-tuplets cross-coupled resonators microwave filters using matrix rotations. *Microwave Theory and Techniques, IEEE Transactions on*, 53(5):1693–1698, 2005.

[150] W. A. Atia, K. A. Zaki, and A. E. Atia. Synthesis of general topology multiple coupled resonator filters by optimization. In *Microwave Symposium Digest, 1998 IEEE MTT-S International*, volume 2, pages 821–824 vol.2.

[151] A. B. Jayyousi and M. J. Lancaster. A gradient-based optimization technique employing determinants for the synthesis of microwave coupled filters. In *Microwave Symposium Digest, 2004 IEEE MTT-S International*, volume 3, pages 1369–1372 Vol.3.

[152] Chun Young-Hoon, Lee Jae-Ryong, Yun Sang-Won, and Rhee Jin-Koo. Design of an rf low-noise bandpass filter using active capacitance circuit. *Microwave Theory and Techniques, IEEE Transactions on*, 53(2):687–695, 2005.

[153] P.H. Ladbrooke. *MMIC Design: GaAs FETS and HEMTs*. Artech House, 1989.

[154] H. Spreadbury P. J. Ahmed H. Ahmed. *Analogue and digital electronics for engineers : an introduction*. Cambridge University Press, Cambridge [Cambridgeshire]; New York, 1984.

[155] Jia-Liang Chen, Sheng-Fuh Chang, Cherng-Cherng Liu, and Hsi-Wei Kuo. Design of a 20-to-40 ghz bandpass mmic amplifier. In *Microwave Symposium Digest, 2003 IEEE MTT-S International*, volume 2, pages 1275–1278. IEEE.

[156] LungHwa Hsieh and Kai Chang. Narrowband highselectivity active bandpass filters using openloop multiplering resonators. *International Journal of RF and Microwave ComputerAided Engineering*, 15(1):109–115, 2005.

[157] T. Dao, S. Huettner, and A. Platzker. A low phase noise mmic/hybrid 3.0w amplifier at x-band. In *Microwave Symposium Digest, 1986 IEEE MTT-S International*, pages 459–462.

[158] J. B. Vincent and D. G. Van der Merwe. A 16 w solid state mmic x-band amplifier for twt replacement. In *AFRICON, 1996., IEEE AFRICON 4th*, volume 2, pages 749–752 vol.2.

[159] E. M. Suijker, M. Sudow, M. Fagerlind, N. Rorsman, A. P. De Hek, and F. E. van Vliet. Gan mmic power amplifiers for s-band and x-band. In *Microwave Conference, 2008. EuMC 2008. 38th European*, pages 297–300.

[160] Xiao-mei Wang, Zhengwen Sun, Yong Chen, and Sixiu Wang. Design of x-band low-noise amplifier for optimum matching between noise and power. In *Education Technology and Computer (ICETC), 2010 2nd International Conference on*, volume 5, pages V5–184–V5–188.

[161] V. J. Patel, H. S. Axtell, C. L. Cerny, G. L. Creech, R. G. Drangmeister, M. A. Gouker, T. L. James, A. G. Mattamana, I. O. Mbuko, R. A. Neidhard, E. B. Nykiel, P. L. Orlando, D. L. Selke, J. M. Wiedemann, and T. K. Quach. X-band low noise amplifier using sige bicmos technology. In *Compound Semiconductor Integrated Circuit Symposium, 2005. CSIC '05. IEEE*, page 4 pp.

[162] Nakajima Kensuke, Y. Yoshida, Ueda Hiroomi, T. Nishino, H. Fukumoto, and N. Suematsu. X-band sige-mmic low noise amplifier using low parasitic capacitance via holes for emitter grounding. In *Radio and Wireless Symposium, 2007 IEEE*, pages 431–434.

[163] P. B. Basyurt and N. Tarim. An x-band sige low-noise amplifier with high gain and low noise figure. In *Communications, Control and Signal Processing, 2008. ISCCSP 2008. 3rd International Symposium on*, pages 1103–1106.

[164] C. E. Patterson, T. K. Thrivikraman, S. K. Bhattacharya, C. H. J. Poh, J. D. Cressler, and J. Papapolymerou. Organic wafer-scale packaging for x-band sige low noise amplifier. In *Microwave Conference, 2009. EuMC 2009. European*, pages 141–144.

[165] P. Roux, Y. Baeyens, J. Weiner, and Y. K. Chen. Ultra-low-power x-band sige hbt low-noise amplifiers. In *Microwave Symposium, 2007. IEEE/MTT-S International*, pages 1787–1790.

[166] P. Saad, C. Fager, Haiying Cao, H. Zirath, and K. Andersson. Design of a highly efficient 2-4-ghz octave bandwidth gan-hemt power amplifier. *Microwave Theory and Techniques, IEEE Transactions on*, 58(7):1677–1685, July 2010.

[167] Kenle Chen and D. Peroulis. Design of highly efficient broadband class-e power amplifier using synthesized low-pass matching networks. *Microwave Theory and Techniques, IEEE Transactions on*, 59(12):3162–3173, Dec 2011.

[168] Dale E. Dawson. Closed-form solutions for the design of optimum matching networks. *Microwave Theory and Techniques, IEEE Transactions on*, 57(1):121–129, Jan 2009.

[169] C. Sayre. *Complete Wireless Design*. McGraw-Hill Education, 2008.

[170] California Eastern Laboratories (CEL). Nec's super low noise hj fet, 07/01/2004 2004.

[171] ADS. Advanced design system, 2011.

[172] Talal Skaik. *Synthesis of coupled resonator circuits with multiple outputs using coupling matrix optimization*. Phd thesis, 2011.

[173] Mike J Lancaster. *Passive microwave device applications of high-temperature superconductors*. Cambridge University Press, 2006.

[174] Lee Kook Joo, Lee Dong Ho, Rieh Jae-Sung, and Kim Moonil. A v-band waveguide transition design appropriate for monolithic integration. In *Microwave Conference, 2007. APMC 2007. Asia-Pacific*, pages 1–4.

[175] Wenlin Xia, Xiaobang Shang, and M.J. Lancaster. All-resonator-based waveguide diplexer with cross-couplings. *Electronics Letters*, 50(25):1948–1950, 2014.

Publications

1. Michael J. Lancaster, D.G., Tianhao He, Jeffrey Powell, Yingtao Tian and Xiaobang Shang, *Submillimetre Rectangular Waveguides based on SU-8 photoresist micromachining technology*, in *ARMMS RF and Microwave Society*. 2014: Wyboston Lakes, Bedfordshire, UK.

2. Rashad Mahmud, Tianhao He, Michael Lancaster, *Micromachined Travelling Wave Slotted Waveguide Antenna Array for Beam-Scanning Applications*, in *Loughborough Antennas and Propagation Conference (LAPC)*. 2014: Loughborough, UK.

3. Tianhao He, Jeffrey Powell, Richard G. Humphreys, Michael J. Lancaster, *On the Application of Coupling Matrix Filter Synthesis to the Design of Amplifier Input Matching Circuits*, draft to be submitted to IEEE Transactions on MTT.

Presentation

- Tianhao He, David Glynn, Michael J. Lancaster, Yingtao Tian, Jeff Powell,and Xiaobang Shang, *Submillimetre Rectangular Waveguides based on SU-8 photoresist micromachining technology*, in *ARMMS RF and Microwave Society*. 2014: Wyboston Lakes, Bedfordshire, UK. (**Best Paper Award**)

Submillimetre Rectangular Waveguides based on SU-8 photoresist micromachining technology

Michael J. Lancaster, David Glynn, Tianhao He, Jeff Powell, Yingtao Tian and Xiaobang Shang.

School of Electronic, Electrical and System Engineering

The University of Birmingham

Abstract

Rectangular waveguides are fundamental structures for the transmission of signals at millimetre and submillimetre wavelengths. This paper describes the design and measured results for two rectangular waveguides based on layered SU-8 photoresist micromachining technology, with double-layer fabrication techniques to minimise the air gaps between layers. A brief description of the SU-8 photoresist micromachining procedure is given in the paper. One waveguide is demonstrated for the WR3 band from 220 GHz to 325 GHz the other is for the WR6 band 120 GHz to 170 GHz both are made of layered SU-8 with a 3 piece construction. Both waveguides have novel bends in order to connect to the measurement apparatus. The measured performance is presented and compared to conventional machined metal waveguide structures. The measured insertion loss for the SU8 waveguides in both bands is better than 0.03 dB/mm.

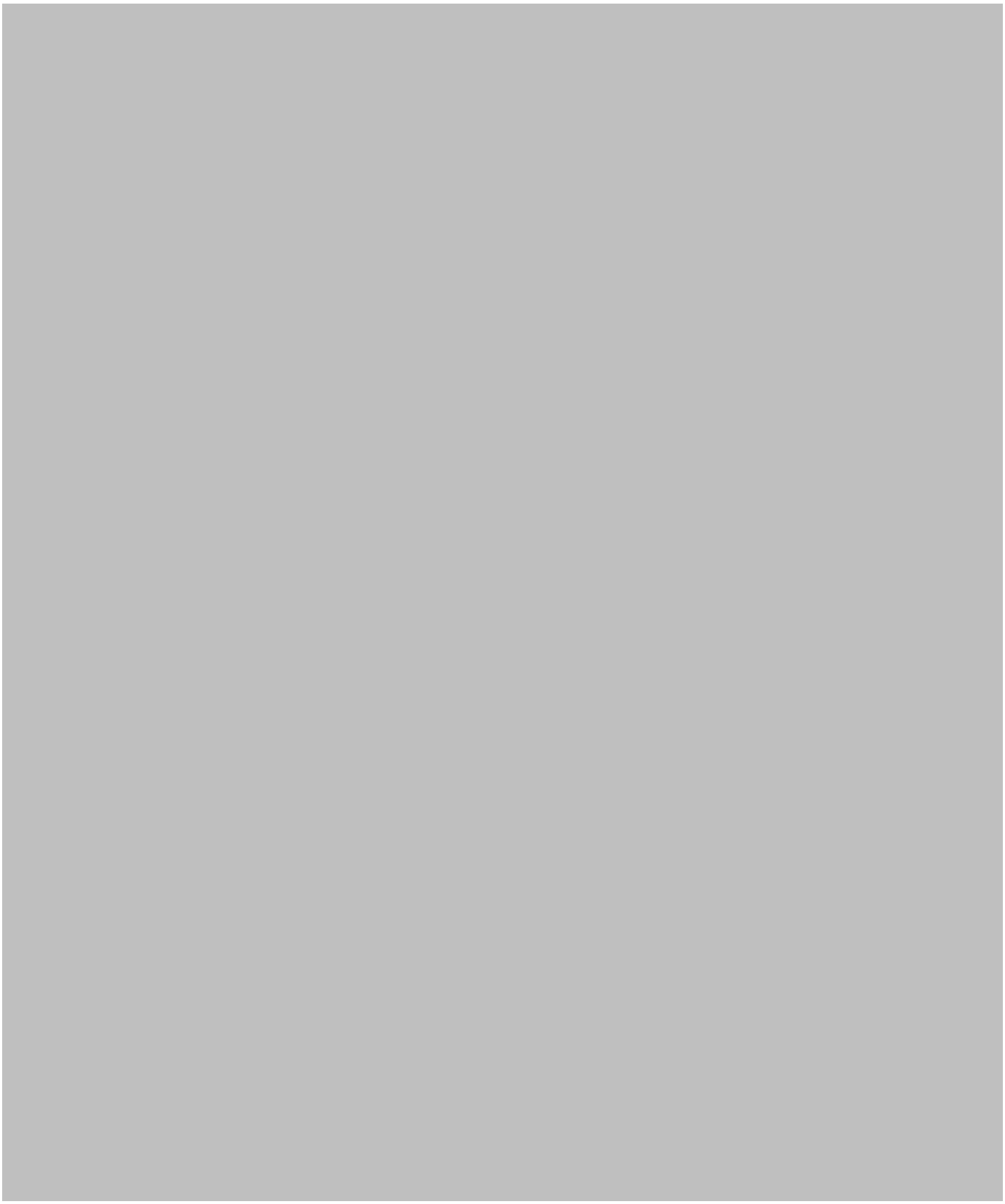

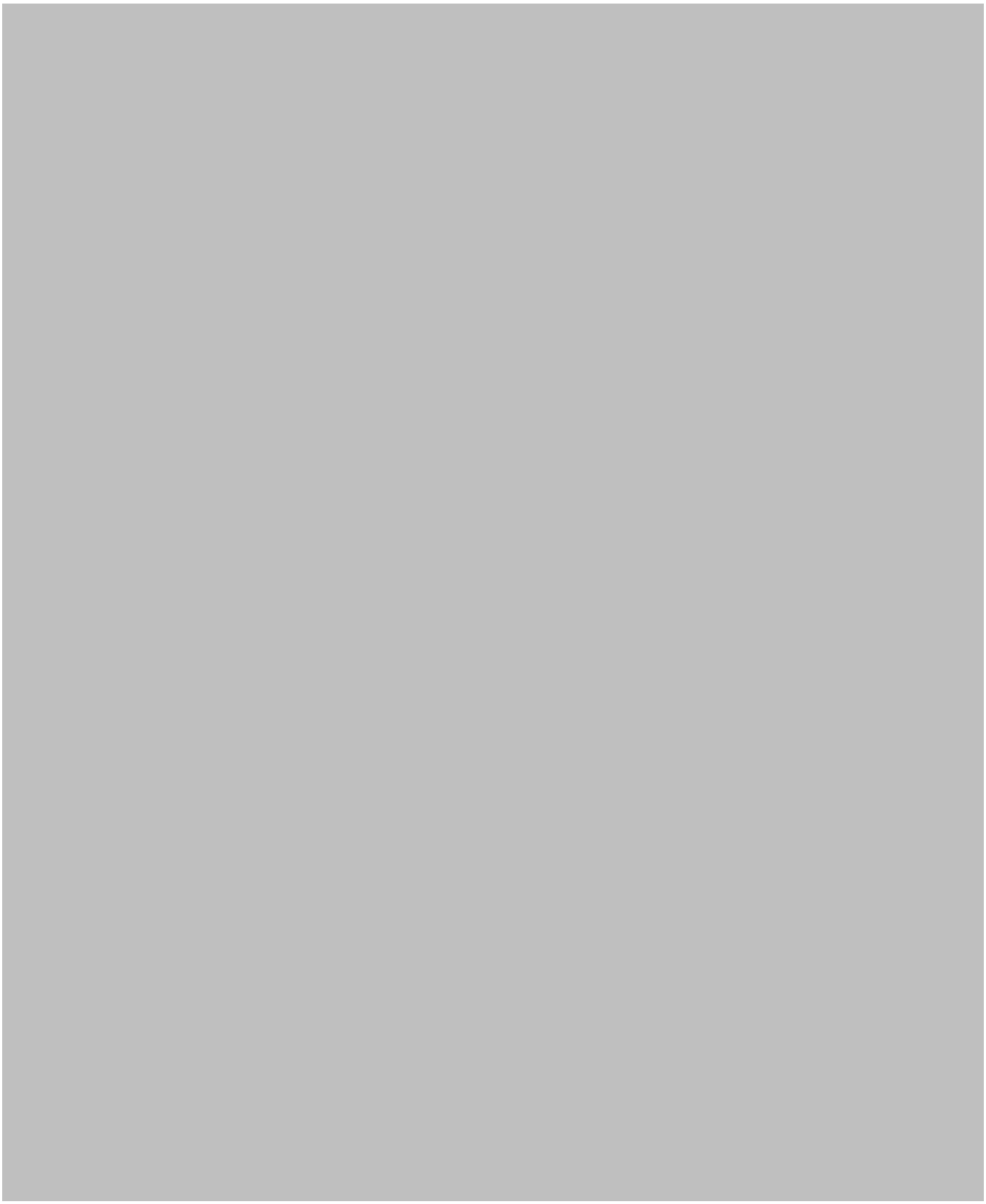

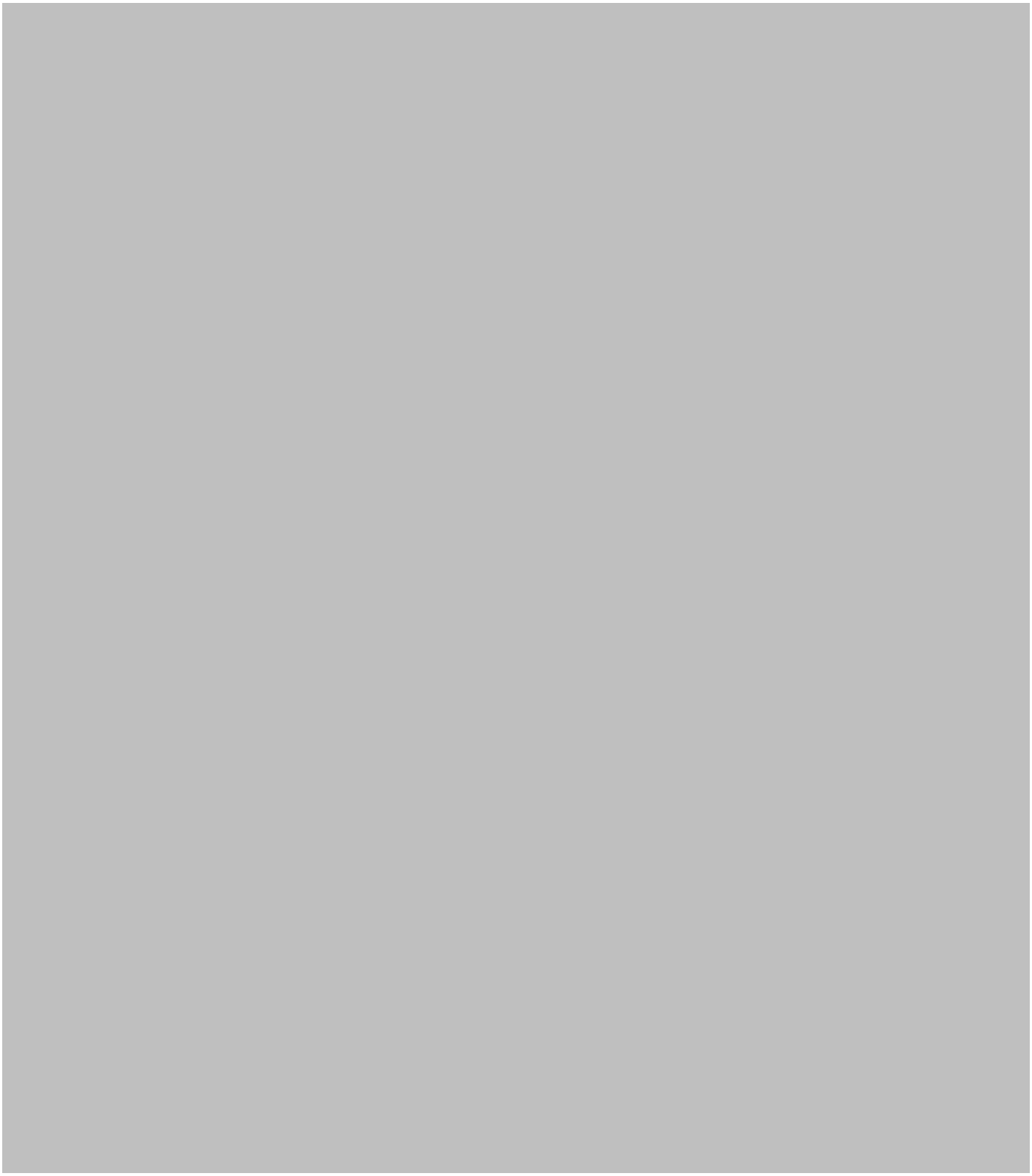

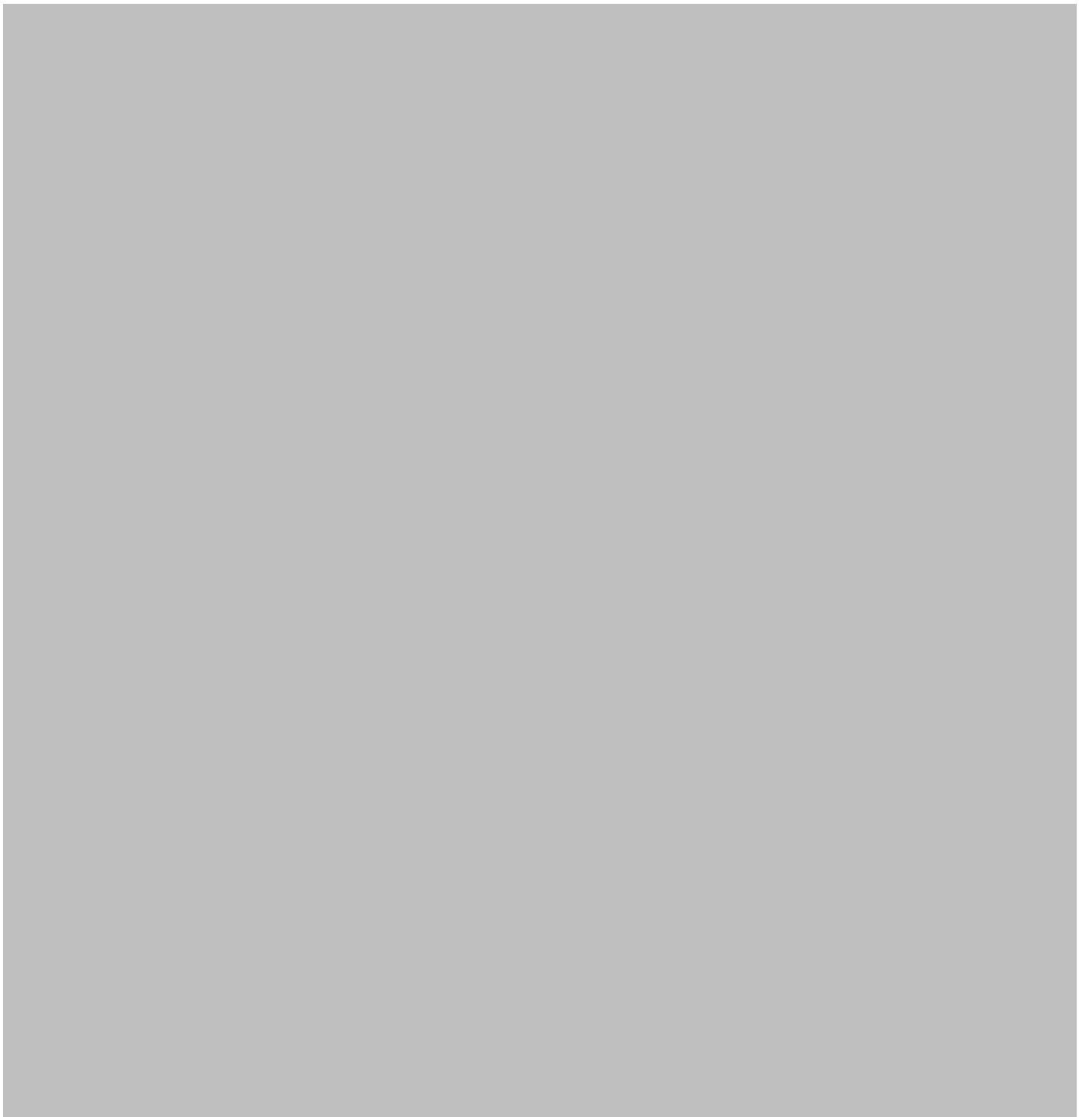

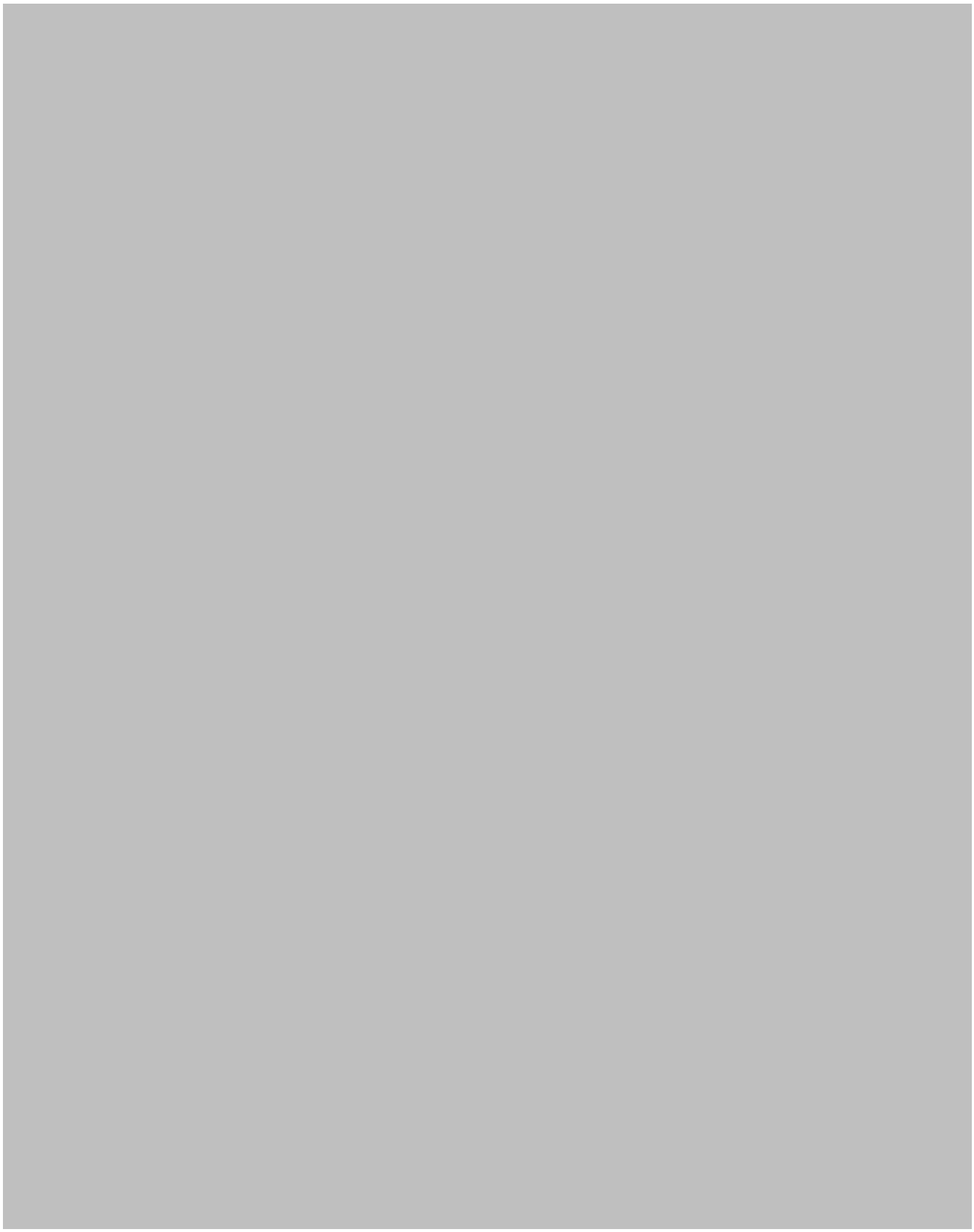

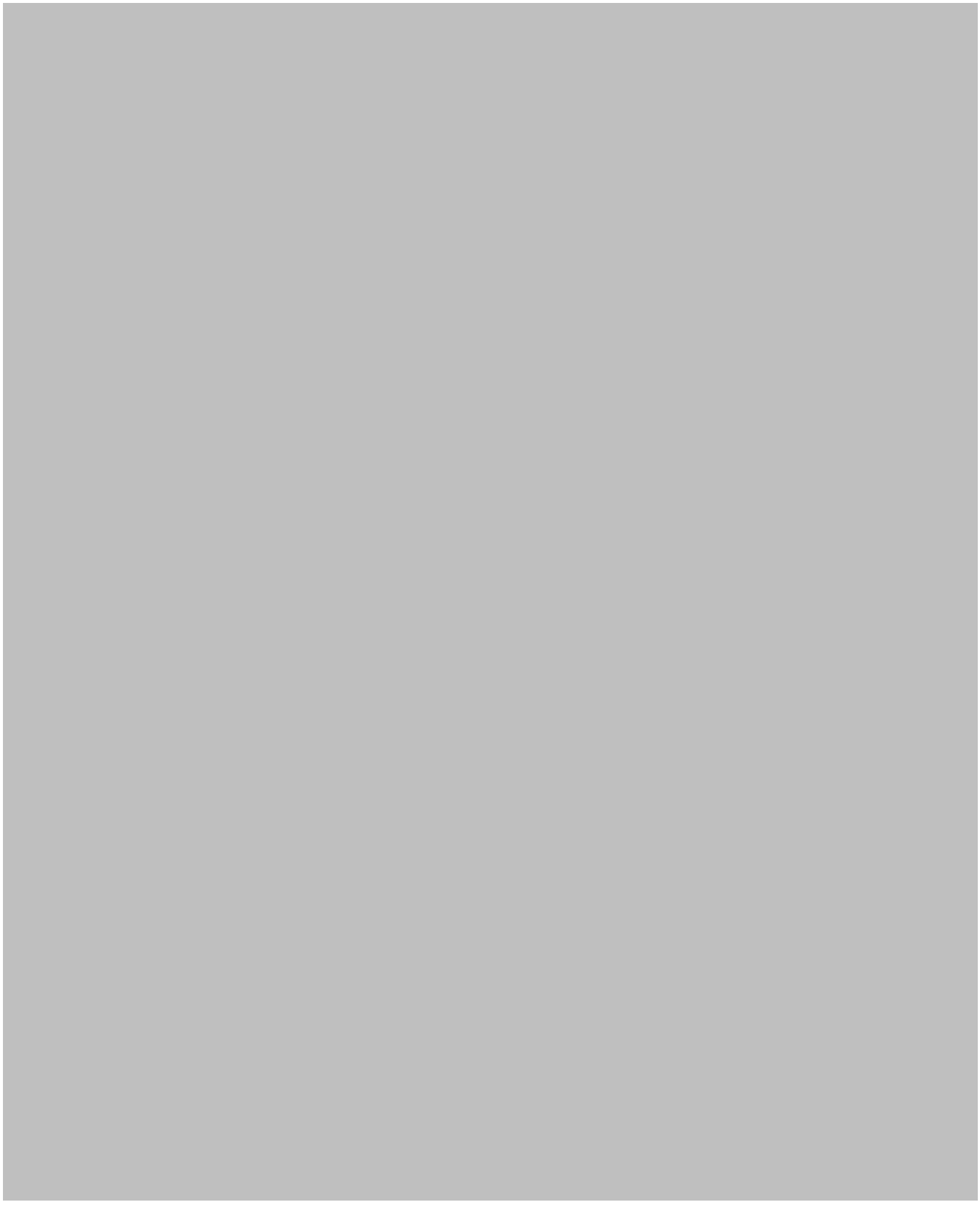

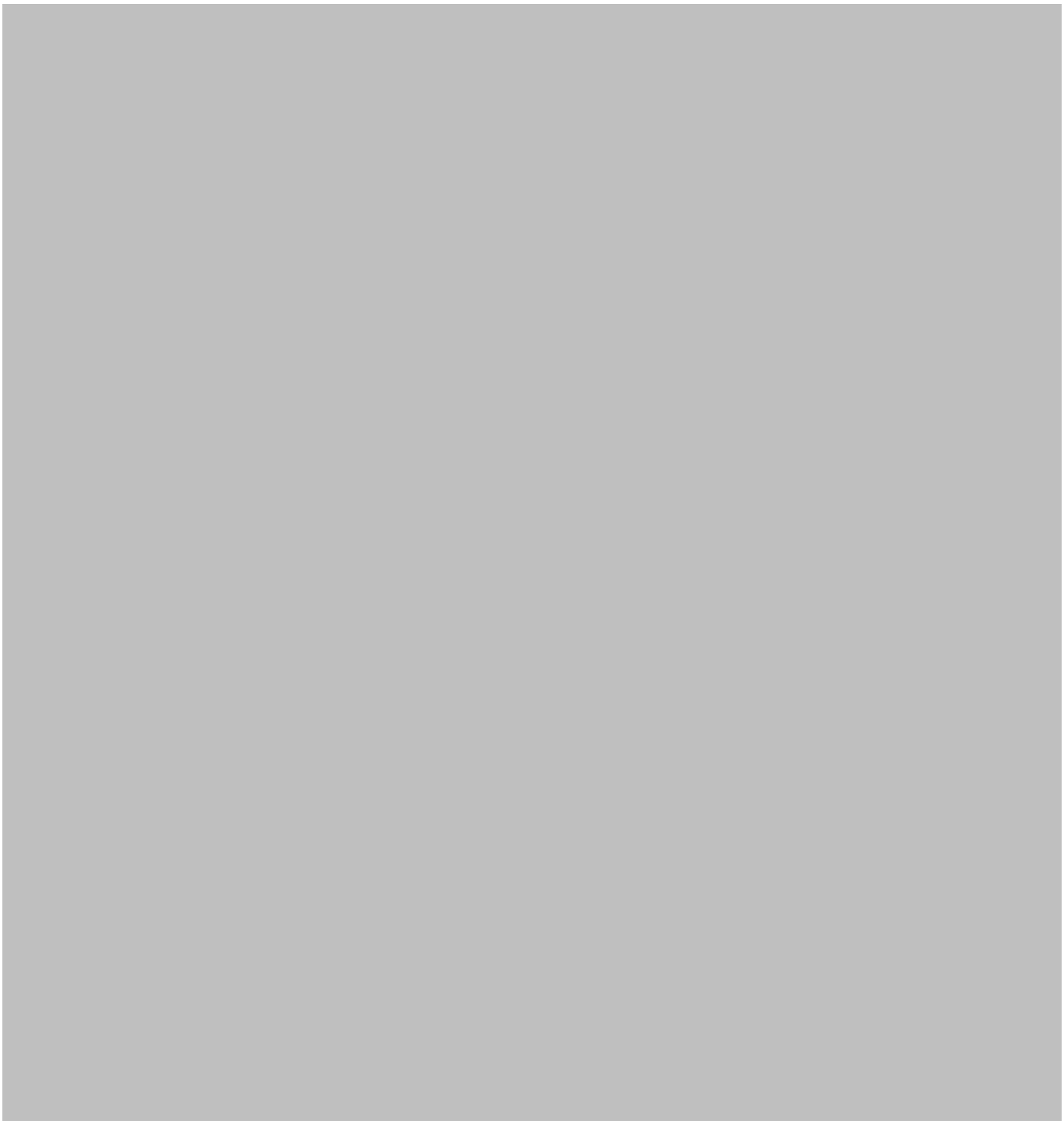

Micromachined Travelling Wave Slotted Waveguide Antenna Array for Beam-Scanning Applications

Rashad Mahmud[1],Tianhao He[1], Micahel Lancaster[1]
[1]*School of Electronic, Electrical and Computer Engineering*
University of Birmingham
Edgbaston, Birmingham, B15 2TT, UK
RHM112@bham.ac.uk,TXH166@bham.ac.uk,
m.j.lancaster@bham.ac.uk,

Yi Wang[2], Xiaobang Shang[1]
[2]*School of Engineering*
University of Greenwich (Medway campus)
Chatham, ME4 4TB, Kent, UK
Yi.Wang@greenwich.ac.uk, X.shang@bham.ac.uk

***Abstract*—A design of travelling wave slotted waveguide antenna array based on micromachined layers operated in the WR-03 frequency band (220-325 GHz) is demonstrated in this paper. The antenna structure remains simple and is designed to be fabricated by using thick SU-8 photoresist technology. Instead of a matched load or a back-short at the termination of the waveguide, a novel H-plane bend followed by a radiating slot is integrated in order to minimise the power reflected to the input port and achieve the travelling wave operation. It also enables broadening of the bandwidth, and keeps the high gain value of the antenna. The 8-slot linear array antenna has shown a simulated gain of 13.5 dBi in the E-plane at 300 GHz, and 30% fractional bandwidth from 240 GHz to 325 GHz. The main beam scans in the H-plane, from -25° to -6°over the bandwidth. The scanning feature is attractive for radar applications.**

Keywords—Beam scanning, travelling array, millimeter-wave waveguides, H-bend radiating slos.

978-1-4799-3662-5/14/$31.00 ©2014 IEEE